SUBMISSION TO THE GIF SCWR COMPUTATIONAL BENCHMARK EXERCISE

A COMPUTATIONAL BENCHMARK STUDY OF FORCED CONVECTIVE HEAT TRANSFER TO WATER AT SUPERCRITICAL PRESSURE FLOWING WITHIN A 7 ROD BUNDLE

By DARRYL J.H. McCLURE, B.Eng.

A Thesis
Submitted to the School of Graduate Studies
in Partial Fulfillment for the Requirements for the Degree
Master of Applied Science

McMaster University

MASTER OF APPLIED SCIENCE (2014) MCMASTER UNIVERSITY

(Engineering Physics) Hamilton, Ontario, Canada

Title: A Computational Benchmark Study of Forced Convective Heat Transfer to Water at Supercritical Pressure Flowing Within a 7 Rod Bundle

Author: Darryl James Hubert McClure, B.Eng. (McMaster University)

Supervisor: Dr. D.R. Novog

Number of Pages: xxiv, 166

Abstract

The research and development effort for the next generation of nuclear power stations is being coordinated by the Generation IV International Forum (GIF). The supercritical water reactor (SCWR) is one of the six reactor technologies currently being pursued by the GIF. The unique nature of supercritical water necessitates further examination of its heat transfer regimes. The GIF SCWR blind computational benchmark exercise is focused on furthering the understanding of the heat transfer to supercritical water as well as its prediction.

A methodology for computational fluid dynamics (CFD) simulations using STAR-CCM+ 9.02.005 has been developed for submission to the GIF SCWR computational benchmark exercise. The experiments of the GIF SCWR computational benchmark exercise were those conducted by the Japan Atomic Energy Agency (JAEA). They are of supercritical water flowing upward in a 7 rod bundle. Of the three experimental cases there are (i) an isothermal case, (ii) a low enthalpy, low heat flux case and (iii) a high enthalpy, high heat flux case. A separate effects study has been undertaken and the SST turbulence model has been chosen to model each of the three experiments. A near wall treatment that

ensures a $y+<0.09$ has been used for both of the heated cases and a near wall treatment that ensures a $y+<0.53$ has been used for the isothermal case. This computational approach was determined to be the optimal choice which balances solution accuracy with computation time.

Final simulation results are presented in advance of the release of the experimental results in June 2014.

Acknowledgements

I would first like to thank my supervisor Dr. David Novog for the opportunity to pursue my academic interests over the past two years. I was given the freedom to study what was truly interesting to me and for this I am grateful.

A great deal of guidance has come from Dr. Alex Rashkovan whose impact on this work cannot be overstated; his expertise and patience throughout this project's entirety has been invaluable. From answering long winded technical emails to our many discussions over Skype, he was always very gracious with his time.

I would like to thank my colleagues of JHE 327, both past and present, for offering both unwelcome and welcome distraction from my computer screen. This has certainly helped maintain my sanity.

Finally and most importantly, this work is a testament to my strong support system of friends and family. There are far too many names to name. However, my mother, in particular, has been a constant source of inspiration and encouragement and for this I am so grateful. Thank you!

Table of Contents

List of Figures

List of Tables

List of Acronyms

AR	Aspect Ratio
CFD	Computational Fluid Dynamics
DHT	Deteriorated Heat Transfer
DNS	Direct Numerical Simulation
EHT	Enhanced Heat Transfer
EVM	Eddy Viscosity Model
GIF	Generation IV International Forum
HTC	Heat Transfer Coefficient
JAEA	Japan Atomic Energy Agency
LES	Large Eddy Simulation
NHT	Normal Heat Transfer
P/D	Pitch to Diameter Ratio
RANS	Reynolds Averaged Navier Stokes
RGR	Radial Growth Rate
RNG	Re-Normalized Group
RSM	Reynolds Stress Model

SCWR	Super-critical Water Reactor
SGS	Sub-Grid Scale
SST	Shear Stress Transport
URANS	Unsteady Reynolds Averaged Navier Stokes

List of Symbols

a_1	SST closure coefficient
A	Area (Chapter 6) [m^2], Wolfstein closure coefficient (Appendix A)
A_ε	Wolfstein closure coefficient
A_μ	Wolfstein closure coefficient
arg_1	SST closure function
arg_2	SST closure function
Bo	Onset of significant buoyancy parameter
c_l	Wolfstein closure coefficient
c_p	Specific heat capacity at constant pressure [$J/kg.K$]
c_s	RSM closure coefficient
c_ε	RSM closure coefficient
$c_{\varepsilon 1}$	RSM closure coefficient
$c_{\varepsilon 2}$	RSM closure coefficient
c_μ	Wolfstein closure coefficient
$CD_{k\omega}$	SST closure function
D_h	Hydraulic diameter [m]

e	Internal energy [J/kg]
f_τ	Blasius' friction factor
F_1	SST closure function
F_2	SST closure function
G	Mass flux [$kg/m^2.s$]
Gr	Grashof number
h	Enthalpy (Chapter 1) [J/kg], Heat transfer coefficient [$W/m^2.K$]
k	Thermal conductivity [$W/m.K$], Turbulent kinetic energy [J/kg]
K_v	Laminarization parameter
l_ε	Wolfstein length scale closure function [m]
Nu	Nusselt number
p	Pressure [Pa]
P	Perimeter [m]
Pr	Prandtl number
q_j	Heat flux in tensor notation [W/m^2]
q''	Heat flux [W/m^2]
Re	Reynolds number
Re_y	Wall distance Reynolds number
T	Temperature [K]
u_i	Instantaneous velocity vector in tensor notation [m/s]
U_i	Mean velocity vector in tensor notation [m/s]
u_i'	Turbulent velocity vector in tensor notation [m/s]

u, v, w	Turbulent velocities in the *x, y, z* directions, respectively [*m/s*]
U, V, W	Mean velocities in the x, y, z directions, respectively [*m/s*]
*u**	Friction velocity [*m/s*]
x_i	Position in tensor notation [*m*]
x, y, z	Rectangular coordinates [*m*]
y	Wall distance [*m*]
y+	Normalized wall distance
y'	Rod wall to bisector of sub-channel distance (Chapter 5)
β	Volumetric coefficient of expansion [*1/K*]
β^*	SST closure coefficient
γ	SST closure coefficient
Γ	Circulation [m^2/s]
δ_{ij}	Kronecker delta function
ε	Turbulent dissipation rate [*J/kg.s*]
ε_{ijk}	Levi-Civita symbol
κ	von Karman's coefficient
λ	Wolfstein blending function
μ	Dynamic viscosity [*Pa.s*]
μ_t	Turbulent or eddy viscosity [*Pa.s*]
ν	Kinematic viscosity [m^2/s]
ρ	Density [kg/m^3]
τ_{ij}	Viscous stress tensor [*Pa*]

τ_w	Wall shear stress [Pa]
σ_k	SST closure coefficient
σ_ω	SST closure coefficient
$\sigma_{\omega 2}$	SST closure coefficient
φ	SST closure coefficients
φ_1	$k - \omega$ closure coefficients
φ_2	$k - \varepsilon$ closure coefficients
φ_{ij}	Total pressure strain [m^2/s^3]
φ_{ij1}	Slow pressure strain [m^2/s^3]
φ_{ij2}	Rapid pressure strain [m^2/s^3]
ω	Specific turbulent dissipation rate [$1/s$]
ω_i	Vorticity vector in tensor notation [$1/s$]
Ω	Mean strain rate [$1/s$]

Chapter 1

Introduction

1.1 Supercritical Water Reactor

The need for plentiful and affordable clean energy has never been more in demand. Nuclear energy has been harnessed for the past 60 years as a means to produce electricity. These first reactors were rightly termed Generation I reactors. Two decades later brought the improved technology of Generation II designs. The majority of the reactors in operation today are of this generation. Currently, Generation III and III+ are being sold and implemented in growing electricity markets such as Southeast Asia. Each subsequent generation has offered improved safety as well as economics.

It is the plan of the Generation IV International Forum (GIF) to coordinate research and development for the next generation of innovative nuclear power systems [**1**]. Under the umbrella of GIF's research and development there exist multiple innovative reactor concepts. Canada, among multiple other countries, has chosen to contribute effort to the design of a Supercritical Water Reactor

(SCWR). The design of the SCWR will feature coolant that is held at a pressure greater than the critical pressure of *22.1 MPa*. The high enthalpy content of the supercritical water coolant will allow for a lower flow rate through the core for a given power. The steam cycle will be direct and the high temperature outlet condition allows the use of gas turbine technology. The absence of phase change at supercritical pressure negates the need for steam dryers and separators. Each of these features will allow for the containment to be much smaller than Generation III designs and will reduce the capital cost while increasing thermal efficiency.

A consequence of using supercritical water as the reactor coolant is the avoidance of a critical heat flux scenario. The thermal-hydraulic safety design of reactors operating with subcritical coolant is centred on quantifying the conditions at which critical heat flux occurs in order to ensure the structural and thermal integrity of the cladding as well as the fuel. Operating conditions of currently produced commercial reactors are maintained at margins of about 30% away from the conditions that give critical heat flux. The thermal-hydraulic design of the SCWR will centre on the conditions that lead to a less drastic phenomenon known as deteriorated heat transfer (DHT). DHT as well as the other heat transfer regimes of supercritical fluids are not well understood. The complexity of the heat transfer to supercritical fluids is due in part to the unique thermophysical properties of the supercritical fluid.

1.2 Heat Transfer to Supercritical Fluids

A supercritical fluid is one that is held at a pressure greater than the critical pressure. In the case of water this pressure is *22.1 MPa*. At these high pressures there exists no phase change regardless of the temperature. However, large and abrupt changes to the physical properties of the fluid take place near a certain temperature known as the *pseudocritical temperature*, T_{pc}. The pseudocritical temperature is defined as being the temperature at which the specific heat capacity of the fluid reaches its maximum. As the temperature of the fluid is increased from below T_{pc} to above it; density, thermal conductivity and dynamic viscosity decrease drastically. The physical properties of water at *25 MPa* are shown in Figure 1-1.

Due to the distinct property changes the regimes of heat transfer to supercritical fluids are very different than that of subcritical pressure fluids. Pioro and Duffey's [**2**] comprehensive review of heat transfer to supercritical water flowing inside channels categorized hundreds of experimental conditions into one of three heat transfer regimes: (i) normal heat transfer (NHT), (ii) enhanced heat transfer (EHT) and (iii) DHT. The NHT regime can be readily predicted by using Dittus-Boelter type correlations. However, the regimes of EHT and DHT are complicated by the drastic physical property changes that occur in close vicinity to T_{pc}. Detailed discussion of the mechanisms for each of the three heat transfer regimes will be given in Chapter 2.1.

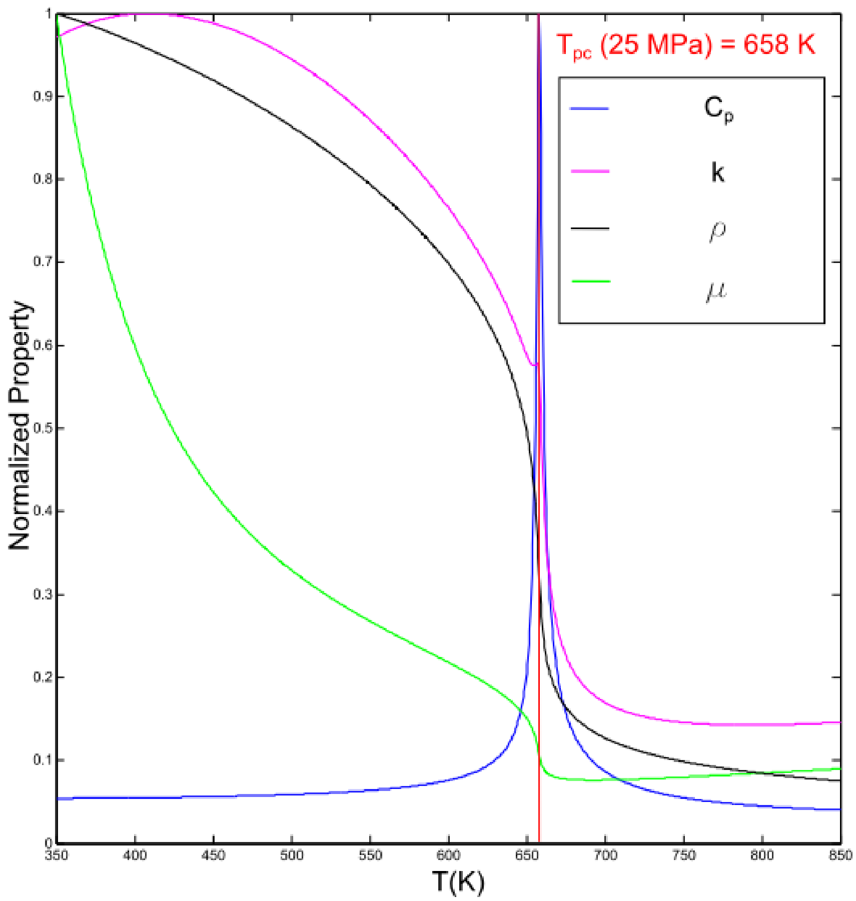

Figure 1-1: Physical property variation of water at *25 MPa*

1.3 GIF SCWR Computational Benchmark Exercise

The purpose of a benchmark exercise is to validate a computational model's performance based on some accepted standard. A computational benchmark exercise in the context of this thesis is one whose purpose is to validate the results given by computational models against a set of experimental data. A benchmark study will strive to identify the best computational models and develop reasoning as to why certain models or modelling approaches outperform others. This will expand the knowledge base of both the physical phenomena being modelled as well as the models themselves.

The experimental data collected by the JAEA has not been shown to the participants and in this sense this is a "blind" benchmark study. This prevents the "tuning" of a computational model in order to match the results of a particular experiment. This is often done without relying upon physical understanding and reasoning. In this way, blind benchmark studies represent the true performance of the models.

The experiments of the JAEA are those of upward flow of supercritical water within a 7 rod bundle that is electrically heated. Rod wall temperature and pressure drop measurements have been made.

The GIF SCWR computational benchmark exercise is driven by the research and development of the SCWR. The safety of the SCWR depends upon, among many other factors, a fundamental understanding of how heat is transferred from the fuel to the coolant. The proposed mechanisms governing the heat transfer to supercritical fluids are not fully understood and the understanding of the problem is limited by the amount and quality of the available experimental data. What is more is that the vast majority of experimental data available is that of flow in tubes and very few studies of flow in rod bundle geometries are reported [**2**]. In order to bridge this knowledge gap that exists for heat transfer to supercritical fluids computational models can be used as a complement to experimental studies. These models are particularly immature and it is thus the goal of the GIF SCWR computational benchmark exercise to expand the knowledge base of the heat transfer to supercritical fluids as well as improve the computational models used to predict these phenomena.

Multiple research groups around the world have agreed to participate in the GIF SCWR computational benchmark exercise. Following the submission of the computational results, the experimental data will be presented and comparisons made in June 2014 in Delft, The Netherlands. The benchmark organizing committee will then compile the results and comparisons to experiment into a mutual scientific paper.

1.4 Computational Fluid Dynamics

The tools to be used for the GIF SCWR computational benchmark exercise belong to a modelling approach known as computational fluid dynamics (CFD). CFD models act to solve the conservation equations of mass, momentum and energy on a discretized domain. The conservation equations can be derived from Newton's second law and the first law of thermodynamics and are known as the Navier-Stokes equations. The system of conservation equations for an incompressible flow is shown in Equations 1.1 – 1.3. The use of the incompressible equation set is justified by the very low Mach number (*0.01*) of the flow studied.

Mass Conservation:

$$\frac{\partial u_i}{\partial x_i} = 0 \tag{1.1}$$

Where u_i represents the local and instantaneous velocity in the i^{th} direction.

Momentum Conservation:

$$\rho \frac{\partial u_i}{\partial t} + \rho u_j \frac{\partial u_i}{\partial x_j} = -\frac{\partial p}{\partial x_i} + \frac{\partial \tau_{ij}}{\partial x_j} \tag{1.2}$$

Where p is the local pressure and $\tau_{ij} \equiv \mu \left(\frac{\partial U_i}{\partial x_j} + \frac{\partial U_j}{\partial x_i} \right)$ is the viscous stress tensor.

The momentum equation is the balance of the unsteady and convective terms on the left hand side of Equation 1.2 with the pressure gradient and the molecular diffusion term on the right hand side.

Energy Conservation:

$$\rho \frac{\partial \left(e + \frac{1}{2} u_i u_i \right)}{\partial t} + \rho u_j \frac{\partial \left(h + \frac{1}{2} u_i u_i \right)}{\partial x_j} = \frac{\partial u_i \tau_{ij}}{\partial x_j} - \frac{\partial q_j}{\partial x_j} \tag{1.3}$$

Where e is the local internal energy, h is the local enthalpy and q_j is the heat flux in the j^{th} direction.

The total energy equation is the balance of the unsteady and convective terms on the left hand side of Equation 1.3 with the work done by surface stresses and the heat conduction term on the right hand side.

The system of equations to be solved are highly nonlinear, second order partial differential equations which are, save for a few very simple cases, not solvable analytically. This reality necessitates a numerical solution. The solution of the system of Equations 1.1 – 1.3 is known as direct numerical simulation (DNS). In practice, applying this method to the solution of a high Reynolds number flow results in a prohibitively large computational grid which precludes its use as a tool for an engineering study. This is due to the very small spatial and temporal scales at which the velocity and temperature field fluctuate. These scales are given by Kolmogorov [**3**] and are not discussed explicitly here in the interest of brevity.

A step down in computational requirements is the large eddy simulation (LES). LES acts to resolve the large spatial and temporal scales of the turbulent flow and accounts for the small scales using what is called a sub-grid scale (SGS) turbulence model. In effect, LES utilizes a low pass filter to eliminate the SGS motions from the conservation equations and then models the effect of the SGS motions.

Another step down in computational requirements is the Reynolds Averaged Navier Stokes (RANS) approach; of which there is an “unsteady” and “steady option, referred to as Unsteady Reynolds Averaged Navier Stokes (URANS) and

RANS, respectively. In this approach the mean flow is the primary focus and the turbulent fluctuations are modelled.

Reynolds had the idea to decompose the instantaneous velocity field into a mean and fluctuating component as in Equation 1.4.

$$u = U + u' \tag{1.4}$$

When this decomposed velocity field is substituted into the Navier Stokes equations and a time average is performed, the RANS equations result as shown in Equation 1.5 – 1.7 [**4**].

$$\frac{\partial U_i}{\partial x_i} = 0 \tag{1.5}$$

$$\rho \frac{\partial U_i}{\partial t} + \rho U_j \frac{\partial U_i}{\partial x_j} = -\frac{\partial \bar{p}}{\partial x_i} + \frac{\partial}{\partial x_j}\left(\tau_{ij} - \rho \overline{u_i' u_j'}\right) \tag{1.6}$$

$$\begin{aligned} \rho \frac{\partial\left(\bar{e} + \frac{1}{2}U_i U_i + \frac{1}{2}\overline{u_i' u_i'}\right)}{\partial t} &+ \rho U_j \frac{\partial\left(\bar{h} + \frac{1}{2}U_i U_i + \frac{1}{2}\overline{u_i' u_i'}\right)}{\partial x_j} \\ &= \frac{\partial U_i}{\partial x_j}\left(\tau_{ij} - \rho\overline{u_i' u_j'}\right) - \frac{\partial \overline{q_j}}{\partial x_j} \\ &- \rho \frac{\partial}{\partial x_j}\left(\overline{u_j' h'} + \frac{1}{2}\overline{u_j' u_i' u_i'} - \overline{u_i' \tau_{ij}}\right) \end{aligned} \tag{1.7}$$

Equation 1.7 can be interpreted as the conservation equation of the total energy as a sum of the internal energy, kinetic energy of the mean flow and the turbulent kinetic energy.

The time average mentioned above is defined differently for URANS and RANS. The most commonly used form of the RANS equation set is a time average over an *infinite* time domain as seen in Equation 1.8.

$$F_T(x) = \lim_{T\to\infty} \frac{1}{T} \int_{t-\frac{1}{2}T}^{t+\frac{1}{2}T} f(x,t)dt \tag{1.8}$$

Where $F_T(x)$ is the time average of the flow variable $f(x,t)$.

From this definition the time derivatives in Equations 1.6, 1.7 will be exactly zero and thus the RANS solution will be independent of time.

The URANS time averaging procedure has a subtle difference in that integration is performed over a *finite* time domain as in Equation 1.9.

$$\widetilde{F_T}(x,t_i) = \frac{1}{T} \int_{t_i-\frac{1}{2}T}^{t_i+\frac{1}{2}T} f(x,t)dt \tag{1.9}$$

Where $\widetilde{F_T}(x,t_i)$ is the modified time average of the flow variable $f(x,t)$, T is a constant time step and t_i is the discretized time such that the modified time average is defined at intervals of T.

It can be seen that Equations 1.5 – 1.7 maintain the exact form as Equations 1.1 – 1.3 along with additional terms that are shown in Table 1.1:

Table 1-1: Additional terms present in the RANS equations

Term	Description
$\rho\overline{u_i'u_j'}$	Reynolds stress tensor
$\overline{u_j'h'}$	Turbulent transport of heat
$\frac{1}{2}\overline{u_j'u_i'u_i'}$	Turbulent transport of turbulent kinetic energy
$\overline{u_i'\tau_{ij}}$	Molecular diffusion of turbulent kinetic energy

The terms included in Table 1.1 represent additional unknowns and approximations must be made for each term in order to close the system of equations. These closure approximations depend on experimental results in order to determine the proportionality constants. This is what is meant by “turbulence modelling”.

1.4.1 Turbulence Modelling

In the context of RANS modelling, there are two fundamental approaches to solving this closure problem and they differ in their treatment of the Reynolds stress term.

1.4.1.1 Reynolds Stress Modelling

In the Reynolds stress modelling (RSM) approach, transport equations are derived for each of the six Reynolds stresses. If Equation 1.6 is subtracted from Equation 1.2, an equation for u_i' is obtained. When this equation is multiplied by u_j' and a time average is taken, the exact transport equation for the Reynolds stress tensor is obtained as seen in Equation 1.10 [**5**].

$$
\begin{aligned}
&\frac{\partial \overline{u_i' u_j'}}{\partial t} + U_j \frac{\partial \overline{u_i' u_j'}}{\partial x_j} \\
&\qquad = -\left(\overline{u_j' u_k'} \frac{\partial U_i}{\partial x_k} + \overline{u_i' u_k'} \frac{\partial U_j}{\partial x_k} \right) - 2\nu \overline{\frac{\partial u_i'}{\partial x_k} \frac{\partial u_j'}{\partial x_k}} \\
&\qquad + \overline{\frac{p}{\rho} \left(\frac{\partial u_i'}{\partial x_j} + \frac{\partial u_j'}{\partial x_i} \right)} \\
&\qquad - \frac{\partial}{\partial x_k} \left(\overline{u_i' u_j' u_k'} - \nu \frac{\partial \overline{u_i' u_j'}}{\partial x_k} + \overline{\frac{p}{\rho} \left[\delta_{jk} u_i' + \delta_{ik} u_j' \right]} \right)
\end{aligned}
\tag{1.10}
$$

The left hand side of Equation 1.10 are the usual unsteady and convection terms. These are balanced, from left to right, by the generation, dissipation, pressure strain and diffusion terms. The diffusion term is made up of the turbulent transport of Reynolds stress, molecular diffusion of Reynolds stress and the pressure diffusion of Reynolds stress. Equation 1.10 introduces an extensive list of additional unknowns, indeed more than the original system of equations. These terms must be modelled in order for a computational solution to be obtained. The modelled form of the RSM will be further described in Chapter 3.2, where it will be seen that the RSM approach will include the solution of seven additional transport equations; one for each Reynolds stress and one for the dissipation rate.

1.4.1.2 Eddy Viscosity Modelling

Eddy viscosity models (EVMs) are based on the assumption that the Reynolds stresses can be related to the mean velocity field; specifically that the Reynolds stresses are aligned with their corresponding velocity gradients. This assumption is known as the Boussinesq approximation and is given in Equation 1.11:

$$-\rho\overline{u_i'u_j'} = \mu_t\left(\frac{\partial U_i}{\partial x_j} + \frac{\partial U_j}{\partial x_i}\right) - \frac{2}{3}\rho k\delta_{ij} \tag{1.11}$$

Where μ_t is the eddy viscosity which is a scalar property of the flow and is free to change across the flow domain. The eddy viscosity is defined using two independent parameters of turbulence and these parameters are solved by two additional transport equations. One of which is for the turbulent kinetic energy, k, shown in Equation 1.12 which is one half the trace of Equation 1.10. The second transport equation to be solved is associated with the dissipation of turbulence and the vast majority of the models solve an equation for ε or ω. The details of the modelled equations will be presented in Chapter 3.1.

$$k = \frac{1}{2}\overline{u_i'u_i'} \tag{1.12}$$

$$\frac{\partial k}{\partial t} + U_j \frac{\partial k}{\partial x_j} = -\overline{u_i' u_j'} \frac{\partial U_i}{\partial x_j} - \nu \overline{\frac{\partial u_i'}{\partial x_j} \frac{\partial u_i'}{\partial x_j}} - \frac{1}{2} \frac{\partial}{\partial x_j} \overline{u_i' u_i' u_j'} - \frac{1}{\rho} \frac{\partial \overline{u_i p}}{\partial x_i} - \nu \frac{\partial^2 k}{\partial x_j \partial x_j} \tag{1.13}$$

The turbulent kinetic energy equation includes the usual unsteady and convective terms on the left hand side and is balanced by turbulence production, dissipation, turbulent transport, pressure diffusion and molecular diffusion.

The Boussinesq approximation assumes the Reynolds stress tensor is a linear function of the strain rate tensor multiplied by a scalar eddy viscosity much in the same way that the viscous stress is related to the strain rate tensor by the molecular viscosity. This simplifying assumption is, in general, not true due to the anisotropic nature of turbulence.

A common closure approximation for the turbulent transport of heat also relies on the Boussinesq approximation and is given in Equation 1.14.

$$\overline{u_j' h'} = -\frac{1}{\rho} \frac{\mu_t}{Pr_T} \frac{\partial \bar{h}}{\partial x_j} \tag{1.14}$$

Where Pr_T is the turbulent Prandtl number and is given a typical value of 0.89 or 0.9 [**4**].

1.4.1.3 Turbulence Modelling Considerations

The EVM approach is by far the most popular turbulence modelling approach because of its computational efficiency and satisfactory prediction of the mean velocity field. However, in certain situations the EVM approach breaks down because an accurate description of the turbulent field is needed to predict certain flow and heat transfer behaviour. In some situations, the RSM approach can be used and can provide improved results in certain situations with an increase in computational cost. The computational cost increase is not only due to the increase in the number of transport equations to be solved but also due to the highly coupled nature of the Reynolds stress equations which can result in poor numerical convergence, thus requiring more iterations [**4**].

1.4.1.4 Modelling of the Near Wall Region

In general there are two ways of incorporating a wall into the computational flow domain; through the use of (i) wall functions or (ii) integration of the solution to the wall.

Due to the lack of computational resources the wall function method was initially preferred and remains in use throughout industry. In this method the conservation equations as well as the transport equations are solved away from the wall and near wall flow variables are defined using semi-empirical wall functions that prescribe the temperature and velocity profiles in terms of laminar and turbulent Prandtl numbers, the friction velocity and the turbulent kinetic energy [**6**].

When using this method it is important to discretize the near wall region such that the first computational cell centre is placed within the log layer. The log layer velocity and temperature profiles are well understood to be described by the logarithmic law of the wall whereas the regions nearer to the wall do not follow this logarithmic behaviour.

The desire to resolve complex near wall behaviour such as separation, reattachment and three dimensional boundary layers is the motivation to integrate the conservation and transport equations to the wall. In order to accomplish this near wall cell sizes must be quite small in order to resolve the appropriate temperature and velocity gradients. In addition, the ease with which the transport equations of turbulence are integrated towards the wall is not universal. For example, the original form of the popular turbulence model $k-\varepsilon$ [**7**] suffers from numerical stability issues due to the awkward boundary conditions placed on the ε equation, whereas the $k-\omega$ [**8**] model suffers no such issue. The adequate resolution of the boundary layer depends on the placement of the first computational cell centre within the laminar sublayer.

There are many methods that have been proposed in order to integrate the ε equation through to the wall that attempt to address the undesirable behaviour in the near wall region. Namely, they are (i) the wall function approach, (ii) the damping function approach and (iii) the two layer approach.

The initial method was to employ wall functions. The high Reynolds number prescription of the ε equation (See Equation 3.16) is used in this formulation. This, however, proved to be unsatisfactory for calculations that included separated flows as well as three-dimensional boundary layer behaviour.

The use of damping functions has been employed by numerous authors. Models that apply this method are termed "low Reynolds number". The idea is to modify the constants attached to the eddy viscosity, production and destruction of dissipation such that they become functions of a wall distance or turbulent Reynolds number. This was first suggested by van Driest [**9**] when prescribing a mixing length in the near wall region.

The two layer formulation acts to prescribe ε algebraically as a function of wall distance in the near wall layer and this value is blended with that of the solution of the ε transport equation up to some critical wall distance or turbulent Reynolds number. The formulation of Wolfstein [**10**] is given in Appendix A.

In order to establish the regions within the turbulent boundary layer a non-dimensional wall distance is used, as below.

$$y+ = \frac{u^* y}{\nu} \tag{1.15}$$

The laminar sublayer is defined to lie at $y+ < 5 - 7$ whereas the log layer is defined to be $30 < y+ < \sim 200$. The layer between the two is referred to as the buffer layer and this layer is influenced by viscous (laminar) and turbulent effects. It is also the region where the production of turbulent kinetic energy is the largest due to the appreciably high velocity gradient and Reynolds stress (see Equation 1.13).

1.4.2 CFD Methodology

The empirical nature of turbulence modelling necessitates rigorous verification and validation studies prior to the application of a turbulence model and computational grid to a particular flow. Turbulence models are usually developed with a particular flow in mind and therefore there exists no one model which is capable of giving acceptable results for all flows.

Verification, in this context, refers to the process of limiting errors due to discretization for a particular turbulence model [**11**], this is a form of dynamic verification as it is known in the software development field [**12**]. These studies are done by successively reducing the time and spatial discretization size until subsequent reduction in discretization size does not yield a change in the results of a particular physical parameter deemed important by the CFD analyst, for example, this could be the drag coefficient for flow over a bluff body such as a car or the lift coefficient of a wing. Once a verified solution has been found comparisons with peer reviewed experimental results can be done.

Validation studies are usually done by comparing multiple verified solutions of various models with an accepted experimental dataset. This comparison acts to quantify the error associated with a particular turbulence model in predicting the physical phenomena deemed important by the CFD analyst [**11**].

The decision to employ a particular turbulence model depends upon many factors. For example, a turbulence model may predict negligible error within a particular validation study but its general strengths and weaknesses are not fully understood due to its lack of use in the scientific literature. In this case, perhaps a turbulence model that did not perform so well in the same validation study would be chosen instead based on its well understood behaviour for a wide variety of physical phenomena. This is the familiar story of the $k - \varepsilon$ model.

When modelling flows and heat transfer in complex geometries of which there is little to no experimental data a *separate effects study* is performed. A separate effects study acts to isolate pertinent physical phenomena to be found in the complex flow of interest and separately verify and validate a modelling approach for each physical phenomenon. Following the separate effects study a decision is made by the CFD analyst as to which approach will be used for the complex flow or if a compromise must be made. For example, modelling flow within a rod bundle the CFD analyst must consider the mean velocity profile and its interaction with the bulk flow turbulence and any circulation induced by features such as grid spacers and the naturally occurring secondary flow. An adequate treatment of the near wall region that may include wall functions or integration of the solution to the wall must be considered in order to capture the heat transfer from the rod wall accurately. Each of the separate effects are, of course, dependent upon one another but coherent modelling decisions are difficult to make with so many complex phenomena present.

In the subsequent chapters the verification process will be referred to as mesh sensitivity studies and multiple validation studies will be used in the separate effects study.

1.5 Objective and Scope

The present study is the author's contribution to the GIF SCWR computational benchmark exercise. This contribution endeavoured to maintain solution accuracy while minimizing computational resources and thus describes an engineering approach to the modelling of heat transfer to supercritical water. The motivation of the benchmark exercise is to further understand the heat transfer mechanisms to supercritical water and also to improve the application of computational models used to predict these mechanisms. This expansion of knowledge is of immediate interest to the research and development effort for the SCWR which is orchestrated by GIF.

A detailed literature review of the experimental and computational investigations of both the heat transfer mechanisms to supercritical fluids as well as rod bundle flow will be the subject of Chapter 2.This is followed by a detailed presentation of the computational models to be used in Chapter 3. Chapter 4 will present the experimental and modelled conditions of the experiments conducted by the JAEA. Chapter 5 will present the results of the separate effects study performed and put forth an argument for a particular turbulence model. Chapter 6 will present the mesh sensitivity studies. The results to be submitted to the GIF SCWR computational benchmark exercise will be presented and discussed in Chapter 7. Chapter 8 will outline the conclusions of this study and discuss suggestions for future work.

Chapter 2

Literature Review

This chapter will review experimental and computational investigations of heat transfer to supercritical fluids and investigations of secondary flow and turbulence structure within rod bundles.

2.1 Investigations of Heat Transfer to Supercritical Fluids

2.1.1 Experimental Studies

As mentioned previously, Pioro and Duffey's [**2**] extensive review identified three distinct heat transfer regimes present for heat transfer to supercritical fluids. Those being (i) normal heat transfer (ii) enhanced heat transfer and (iii) deteriorated heat transfer. These regimes are defined with comparison to the predictions given by the Dittus-Boelter correlation (Equation 2.2). The EHT regime is defined by its heat transfer coefficient (HTC) being larger than that predicted by the Dittus-Boelter correlation and the DHT regime is defined by its HTC being smaller than that predicted by the Dittus-Boelter correlation. The correlations developed to predict these phenomena are presented followed by physical descriptions of the enhanced and deteriorated heat transfer regimes.

2.1.1.1 Correlations for Heat Transfer to Supercritical Fluids

The NHT regime has been noted to be similar to that of heat transfer to subcritical fluids far away from critical pressure regions and therefore Dittus-Boelter type correlations are seen to adequately predict the heat transfer coefficient [**2**]. For such flows in a CFD analysis, wall functions may be used.

$$q'' = h(T_w - T_b) \tag{2.1}$$

The definition of the heat transfer coefficient is shown in Equation 2.1 and the original Dittus-Boelter correlation is shown in Equation 2.2, where the Nusselt number, Nu, represents the ratio of the heat transfer due to convection to that of conduction, the Reynolds number, Re_b, is the ratio of inertial forces to viscous and the Prandtl number, Pr, is the ratio of the momentum diffusivity to the thermal diffusivity.

$$Nu = \frac{hD_h}{\lambda} = 0.023 Re_b^{0.8} Pr_b^{0.4} \tag{2.2}$$

This particular correlation has applicability for internal turbulent flow downstream of inlet effects. However, the use of Pr_b led to unrealistic results for predictions near the critical and pseudocritical points because of its sensitivity to property variation [**13**].

The work of Krasnoshchekov and Protopopov [**14**] [**15**], Krasnoshchekov et al [**16**] and Petukhov et al [**17**] gave the correlation seen in Equation 2.3:

$$Nu = \frac{(\xi/8) Re_b \overline{Pr}}{12.7\sqrt{\xi/8}(\overline{Pr}^{2/3} - 1) + 1.07} \left(\frac{\rho_w}{\rho_b}\right)^{0.3} \left(\frac{\bar{c_p}}{c_{pb}}\right)^{n} \tag{2.3}$$

where $\xi = \frac{1}{(1.82 log_{10} Re_b - 1.64)^2}$ and the exponent n is

$n = 0.4$	for $T_w \leq T_{pc}$ or $1.2T_{pc} \leq T_b$
$n = n_1 = 0.22 + 0.18\left({T_w}/{T_{pc}}\right)$	for $1 \leq T_w/T_{pc} \leq 2.5$
$n = n_1 + (5n_1 - 2)\left[1 - \left({T_b}/{T_{pc}}\right)\right]$	for $1 \leq T_b/T_{pc} \leq 1.2$

$\overline{Pr}$ is an average over the range of temperature defined by the bulk and wall conditions and eliminates the large peak in Pr as c_p becomes very large, this is one improvement introduced by Equation 2.3 as compared to Equation 2.2.

Jackson and Fewster [**18**] modified Equation 2.2 to allow the inclusion of property variations in an effort to extend the functionality of the Dittus-Boelter correlation outside of the NHT regime. The correlation of [**18**] is given in Equation 2.4.

$$Nu = 0.0183 Re_b^{0.82} \overline{Pr}^{0.5} \left(\frac{\rho_w}{\rho_b}\right)^{0.3} \tag{2.4}$$

The choice of employing the ratios of density and specific heat in the correlations was supported by Jackson [**19**] as he stated that the effectiveness of turbulent forced convective heat transfer is dependent upon the turbulent heat flux in the near wall region which is dependent upon the product of the local values of specific heat and density. Taking into account the variation of density and specific heat across the cross section of the flow section has allowed these correlations to expand their application outside of the NHT regime. The correlation shown in Equation 2.3 [**16**] was determined by Jackson [**20**] to predict 97% of the experimental data within 25%. Kim et al [**21**] performed experiments of upward flow in tubes of supercritical carbon dioxide and compared results with multiple correlations and found the correlation of Equation 2.4 [**18**] performed best.

2.1.1.2 Enhanced Heat Transfer

Jackson [**22**] explains the mechanism of EHT by considering three effects. As the wall temperature reaches T_{pc} the thermal conductivity decreases, the specific heat increases and the dynamic viscosity decreases. Although the decrease in thermal conductivity will impair heat transfer, this is more than compensated by the large specific heat and the low viscosity which acts to thin the viscous sublayer.

Yamagata et al [**23**] performed experiments of forced convective heat transfer to supercritical water in tube geometries and mainly reported results that fell into the

EHT regime. When considering upward flow they found that for high mass flux cases with low to moderate heat flux there existed a peak in heat transfer coefficient at a bulk temperature slightly less than T_{pc} and this peak would decrease with an increase of heat flux. Jackson [**24**] explains this phenomena by noting that when the heat flux is low, the temperature gradient is not very steep in the near wall region and as the bulk temperature approaches T_{pc} the near wall temperature approaches T_{pc} slightly upstream and therefore there exists a large region where the value of the specific heat is very high leading to EHT.

2.1.1.3 Deteriorated Heat Transfer

The DHT regime is caused by two mechanisms; (i) thermally induced bulk flow acceleration and (ii) buoyancy influence. The conditions at which these mechanisms are seen can be quite different yet their result on the turbulent boundary layer is quite similar.

2.1.1.3.1 Thermally Induced Bulk Flow Acceleration

The threshold for the onset of thermally induced bulk flow acceleration causing heat transfer deterioration has been explored by Moretti et al [**25**]. The derivation of this threshold resulted from heat transfer measurements for a nearly constant property gas flow in a converging duct. However, it has been used throughout the supercritical water literature to determine the presence of this particular flow phenomenon. Thermally induced bulk flow acceleration is deemed appreciable if the criterion in Equation 2.5 is met.

$$K_v = \frac{4\left(\frac{P_h}{P_w}\right)q^+}{Re_{D_h}} > 3.5 \times 10^{-6} \tag{2.5}$$

Where P_h and P_w are the heated and wetted perimeter, respectively, $q^+ = \frac{\beta q''}{Gc_p}$, and β is the volumetric coefficient of expansion.

The onset of this effect is shown to occur for high values of q'' and is explained by Jackson [**24**] as follows. For a heated tube, the bulk enthalpy increases and the density decreases axially along the flow section. Due to mass continuity the flow accelerates and an additional pressure gradient must be present in order to cause this acceleration. This acceleration is greater within the boundary layer as the velocity in this region is lower. The non-uniform pressure gradient will then act to change the distribution of the shear stress such that it falls more quickly with distance from the wall then it would without flow acceleration. In other words, the region of appreciable shear stress will be confined to a thin layer very near to the wall away from the buffer layer. This results in a drastic decrease of turbulent kinetic energy production, a thickening of the viscous sublayer and a deterioration of heat transfer.

2.1.1.3.2 Buoyancy Influence

The threshold for the consideration of buoyancy effects is given by Mikielewicz et al [**26**]:

$$Bo = \frac{Gr^{*}\delta_{M+}\left(\frac{\nu_w}{\nu_b}\right)\left(\frac{\rho_w}{\rho_b}\right)^{0.5}}{2Nu_{D_h}Re_{D_h}^{3}(f_\tau/2)^{1.5}Pr^{0.4}} > 0.1 \tag{2.6}$$

Palko et al [**27**] applied the Dittus Boelter correlation and the Blasius form of the friction factor and obtained:

$$Bo^{*} = \frac{Gr^{*}}{Re_{D_h}^{3.425}Pr^{0.8}} > 6.0 \times 10^{-7} \tag{2.7}$$

The onset of this effect is shown to occur at low values of mass flux and is explained by Jackson [**24**] as follows. For upward flow, the motion of the higher temperature, lower density near wall layer is aided by the buoyancy force. This causes a change in the velocity as well as the shear stress distribution. The buoyancy in the near wall layer helps overcome the downward shear force exerted on this layer by the wall. In the case without buoyancy, the fluid further from the wall provides a large portion of the upward force on the near wall layer. Therefore, the shear force on the near wall layer in the upward direction provided by the fluid further from the wall is reduced. Because the buoyant layer is very usually located in the buffer layer, a decrease of shear stress in this region results in a drastic decrease of turbulent kinetic energy production, a thickening of the viscous sublayer and a deterioration of heat transfer.

Following the deterioration of heat transfer, recovery is possible due to the strengthening of the buoyancy force exerted on the near wall layer. In this case, the buoyant force is so strong such that it exerts an upward shear force on the bulk fluid region and thus there occurs an inversion of the shear stress direction. Once shear stress is established in this region, turbulence generation and heat transfer recover [**24**].

The absolute nature of these threshold values for the onset of thermally induced bulk flow acceleration and buoyancy influence was called into question by He et al [**28**]. They studied convective heat transfer to CO_2 in upward and downward flow in tubes. It was shown for a sufficiently low Bo^* that the wall temperature distributions for upward and downward flow are equivalent, as expected for flows without buoyancy influence. However, increasing $Bo^* = 4.28E\text{-}7$ resulted in a large difference between the upward and downward flow wall temperature distributions. The effect of buoyancy was obvious in this case despite the fact that Bo^* remained below the criterion of $Bo^* = 6.0E\text{-}7$ suggested by Mikielewicz [**26**].

2.1.2 Computational Studies

Computational studies of heat transfer to supercritical fluids have been used as a complement to experiment. Although there is no replacement for experiment, the high resolution data obtained from CFD can offer deep insight into the various heat transfer mechanisms discussed previously. Prior to using CFD as a predictive tool, the error of a particular model and mesh must be quantified with validation against experimental data. Only then should the data be used as a means to further one's understanding of flow phenomena.

Koshizuka et al [**29**] used the low Reynolds form of the k-ε turbulence model [**30**] to successfully model the EHT regime of the Yamagata et al [**23**] dataset. The DHT regime was then studied without reference to any particular validation data.

Roelofs [**31**] used the low Reynolds form of both the RNG k-ε [**32**] and RSM [**5**] [**33**] turbulence models to simulate the experiments of Yamagata et al [**23**] and achieved equally successful results. Sensitivity to $y+$ was performed using RNG and compared to the $698\ kW/m^2$ case of Yamagata. It was determined that $y+ < 1$ gave acceptable results and were nearly exactly the same as results with $y+ < 0.1$. The verified solutions of RSM and RNG were shown to successfully predict Yamagata et al's results for $q'' = 698\ kW/m^2$.

Palko et al [**27**] used the SST turbulence model [**34**] to investigate the DHT regime using the experiments of Ornatskij et al (high heat flux, high mass flux) [**35**] and Shitsman (moderate heat flux, moderate mass flux) [**36**]. A near wall mesh resolution of $y+ < 1$ was shown to be able to capture the DHT. It was shown that the low coolant flow rate experiments of Shitsman [**36**] resulted in DHT caused by buoyancy influence; this was demonstrated by a simple comparison of simulations done with and without buoyancy terms included in the RANS equations. However, the simulated results for the high coolant flow rate experiments of Ornatskij [**35**] were shown to be insensitive to buoyancy by performing the same simple comparison. This was expected by applying the threshold of Mikielewicz et al [**26**]. It was concluded that for high coolant flow rates some mechanism other than buoyancy caused DHT.

Kim et al [**37**] performed a thorough study using multiple turbulence models to simulate the experiments of Yamagata et al. The standard *k-ε,* standard *k-ω* [**8**], SST, RNG and several low Reynolds number type *k-ε* turbulence models were studied. It was concluded that the best prediction was obtained using the RNG turbulence model with a near wall mesh satisfying *y+ < 1*.

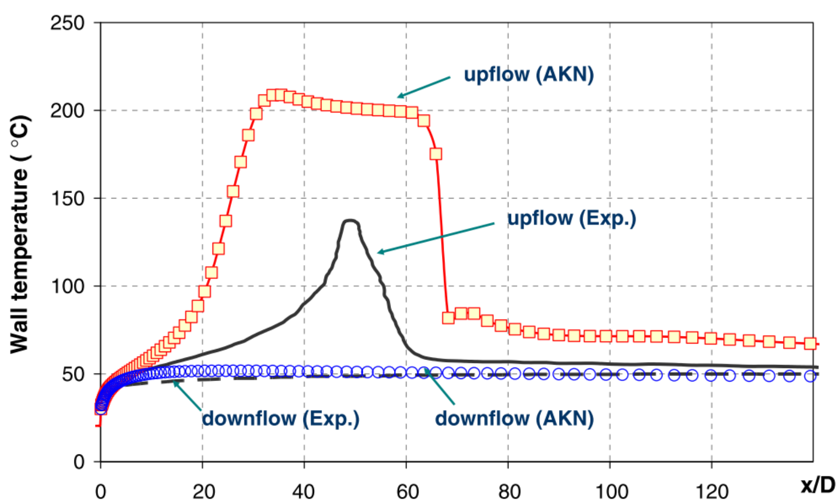

Figure 2-1: T_w vs. axial position comparison of AKN to experiment in buoyancy influenced DHT - Figure reproduced from He et al [28**]**

Table 2-1: Experimental conditions of He et al [28]

Re	*44 046*
q_w (W/m^2)	*68 000*
T_{in} (^{o}C)	*20.5*

He et al [**28**] studied the flow of supercritical CO_2 in tubes described previously. Simulations were performed using the V2F *k-ε* [**38**] and AKN *k-ε* [**39**] turbulence models and their prediction capability was analysed in regions of buoyancy influenced DHT. The near wall cell was always placed such that $y+ < 0.5$. The AKN model predicted the peak in wall temperature seen in upward flow more accurately while both V2F and AKN were able to reproduce the results of the downward flow case. Although the AKN model outperformed the V2F, it was seen that the prediction of the wall temperature peak was not localized as in experiment but spanned the region both upstream and downstream of the experimental peak. This is shown in Figure 2-1. The results of AKN were then used to study the buoyancy influence mechanism of DHT which has been previously described in *2.1.1.3.2.*

Zhu [**40**] offered a thorough comparison of the predictive capabilities of SST versus that of RNG k-ϵ. Prior to the comparison, a mesh sensitivity study was performed to show that a $y+ < 0.1$ gave mesh independent results. Zhu chose to validate a computational approach based on the experiments of Glushchenko et al [**41**], Ornatskii et al [**35**], Yamagata et al [**23**] and Shitsman [**36**], which explore each of the three heat transfer regimes for upward and downward flow of supercritical fluid in tubes. Zhu found that in cases of EHT, RNG over predicted the HTC leading to non-conservative estimates of wall temperatures. In cases of DHT, RNG was shown to predict the deterioration far downstream of where it was seen in experiment, also leading to non-conservative estimates of wall temperature. Conversely, SST showed success in predicting the onset of DHT. The SST model was also shown to give conservative predictions of wall temperature when it was in error with experiment. The SST model was therefore chosen as superior to the RNG model.

Cheng et al [**42**] modelled the heat transfer to supercritical water flowing upward in a triangular lattice and square lattice sub channels. Prior to carrying out the final simulations they performed a validation study using turbulence models of various types, including EVMs and RSMs of both ε and ω type. The validation study used the experimental data of Yamagata et al [**23**] for a low and moderate heat flux. It was shown that the ε type turbulence models performed better than the ω type. In choosing the turbulence model for sub channel flows, Cheng et al [**42**] cited the presence of secondary flow – flow that exists in the plane perpendicular to the flow direction – in rod bundle flow and its importance to predicting the HTC. Therefore, the RSM of Speziale et al [**43**] was chosen for the final simulations on the basis of its capability to resolve the secondary flow and its strength in predicting the experimental results of Yamagata et al [**23**]. The results of the sub channel simulations showed a distinct non-uniformity in HTC along the azimuthal direction, with the square lattice sub channel having a stronger non-uniformity. The results were deemed trustworthy by the appearance of secondary flow cells that were qualitatively similar to that of isothermal, sub channel flow at subcritical conditions.

Yang et al [**44**] also modelled the heat transfer to supercritical water flowing upward in triangle and square lattice sub channels. Following a thorough validation study which compared multiple turbulence models to the experiments of Yamagata et al [**23**] and the correlations of Watts et al [**45**] and Bishop et al [**46**], the two layer model of Hassid et al [**47**] with $y+ < 0.5$ and the standard k-ε model with $y+ > 15$ were chosen as the best options. The simulations of the sub channels were performed with the standard k-ε turbulence model and strong non-uniformity in wall temperature along the circumferential direction was seen in the case of the square lattice sub channel but not for the triangular lattice sub channel. These results agreed with those reported by Cheng et al [**42**] discussed above. The authors concluded that increasing the *P/D* ratio would lessen the non-uniformity seen in wall temperature.

In both the previous studies [**42**] [**44**] of heat transfer to supercritical water within subchannel geometry no mention of modelling the conduction through the rod cladding was described. It is important to note that neglecting the conduction will bias the rod wall temperature results towards stronger non-uniformity.

2.2 Investigations of Rod Bundle Flow

The interesting features of rod bundle flow are the presence of secondary flows and the anisotropic nature of the turbulent field. The study of secondary flows has been done for rod bundle flow but many of the fundamental studies have been done in ducts of square cross section, as this is a simple flow geometry that has been shown to produce secondary flows. The structure of the turbulent field and the secondary flows have been examined by multiple authors both experimentally and computationally.

2.2.1 Experimental Studies

The presence of secondary flows in ducts of non-circular cross section was first noted by Nikuradse [**48**] in studying the shape of the isovels for square duct flow. The displacement of the isovels was postulated by Prandtl [**49**] to be due to superimposed secondary flows that acted to convect high momentum fluid from the bulk flow to the corners and, in order to satisfy continuity, convect low momentum fluid from the mid-point of the walls to the bulk flow. The isovels in a square duct are shown in Figure 2-2. The secondary flow cells found in one quadrant of a square duct are shown in Figure 2-3.

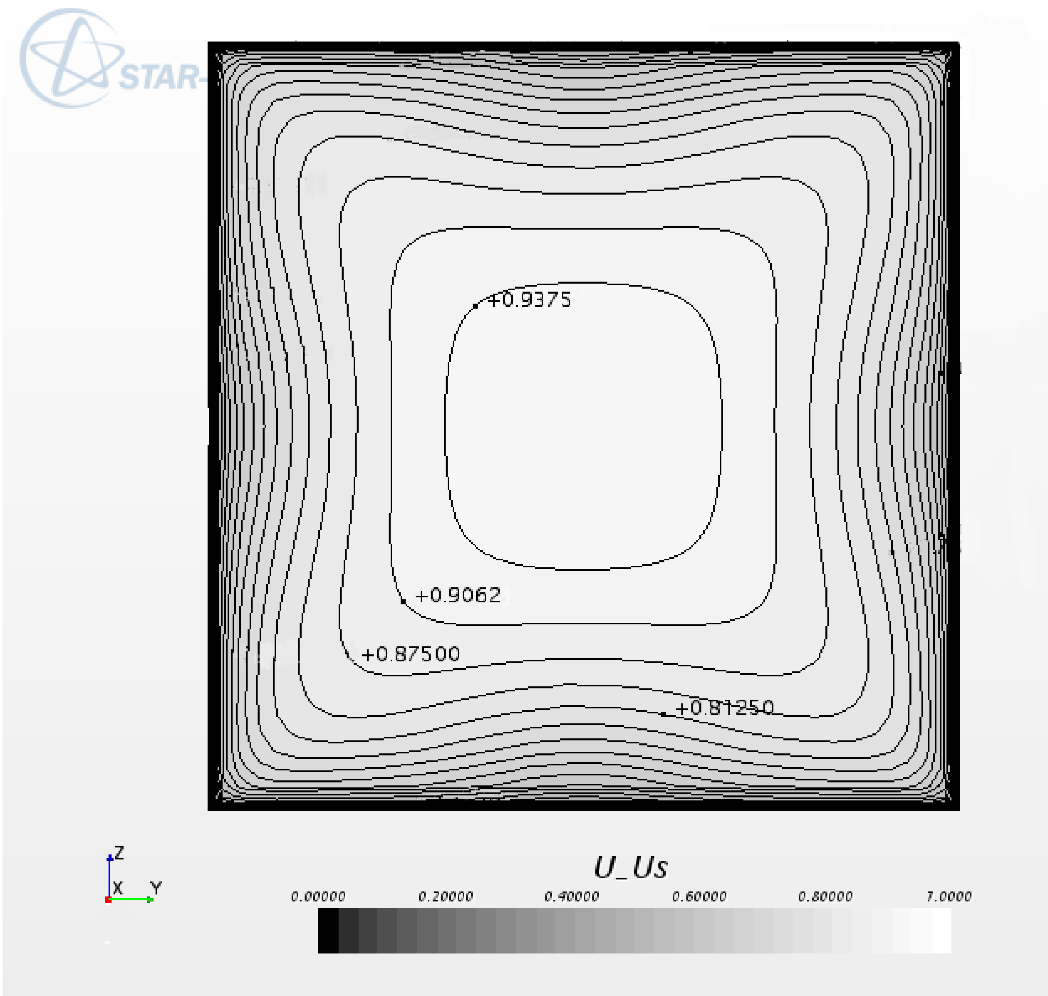

Figure 2-2: Isovels in square duct flow

Brundrett et al [**50**] performed experiments in square duct flow and measured the three velocity components and all six Reynolds stresses. Following this they studied the Reynolds averaged streamwise vorticity equation and noted that the production of secondary flows is due to the second derivative of the Reynolds stress components and therefore cannot be present in laminar flow. They found that the typical pattern of isovels described by Nikuradse [**48**] and seen in Figure 2-2 agreed with their data well.

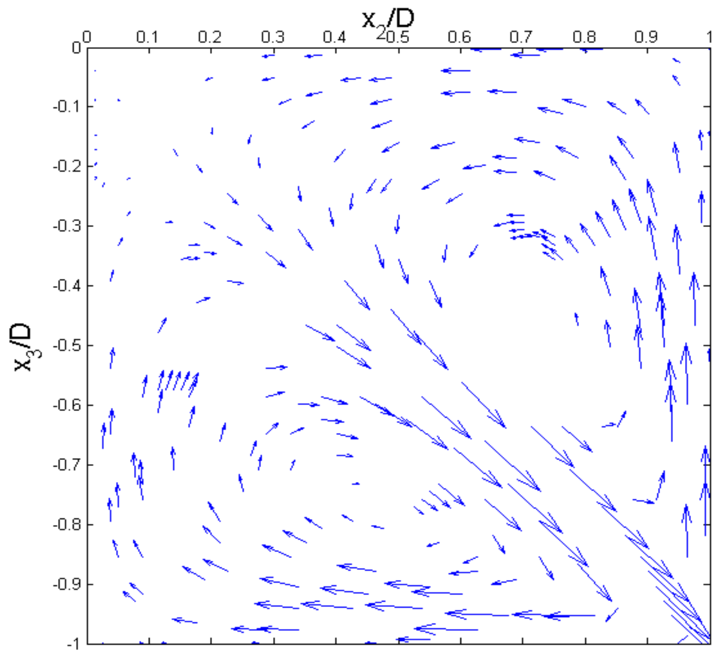

Figure 2-3: Opposing secondary flow cells in one quadrant of a square duct

The Reynolds averaged streamwise vorticity equation has been analyzed by multiple authors and is therefore worth briefly introducing here. This equation is shown below and is derived by taking the curl of Equation 1.6.

$$\rho U_j \frac{\partial \omega_k}{\partial x_j} - \rho \omega_j \frac{\partial U_k}{\partial x_j} + \rho \varepsilon_{ijk} \frac{\partial^2}{\partial \mathrm{x}_i\, \partial \mathrm{x}_l} \left(\overline{u_l' u_j'}\right) = \mu \frac{\partial^2 \omega_k}{\partial \mathrm{x}_j\, \partial \mathrm{x}_j} \tag{2.8}$$

Each of the four terms represents a kinematic process. The first represents an increase in vorticity due to convection along a streamline. The second term is the source of the so called Prandtl's secondary flow of the first kind, in which the angular velocity of a stream tube increases while passing through a constriction [**50**]. The third and fourth term represent the production of vorticity due to the turbulent and viscous stresses, respectively.

When considering only the streamwise direction (which will be assumed as x) for flow in a straight, constant cross section duct for fully developed flow the Reynolds averaged vorticity equation is given as below.

$$U_y \frac{\partial \omega_x}{\partial \mathrm{y}} + U_z \frac{\partial \omega_x}{\partial \mathrm{z}} = \frac{\partial^2}{\partial \mathrm{y}\,\partial \mathrm{z}}\left(\overline{v'^2} - \overline{w'^2}\right) - \left(\frac{\partial^2}{\partial y^2} - \frac{\partial^2}{\partial z^2}\right)\overline{v'w'} + \nu\left(\frac{\partial^2 \omega_x}{\partial \mathrm{y}^2} + \frac{\partial^2 \omega_x}{\partial \mathrm{z}^2}\right) \quad (2.9)$$

It is noted that a few terms have been omitted in Equation 2.9. The term responsible for Prandtl's secondary flows of the first kind was omitted due to the absence of flow constrictions in straight square duct and rod bundle geometries. Terms involving $\frac{\partial}{\partial x}$ have also been omitted due to the fully developed nature of the flow considered.

The terms on the left are the convection of streamwise vorticity due to the secondary flow. The first two terms on the right hand side are responsible for the production of streamwise vorticity and will be referred to as P_1 and P_2, respectively. The last term is the diffusion of streamwise vorticity.

Brundrett et al [**50**] determined that P_1 was the main source of production and this was balanced by convection and diffusion in the near wall region. Gessner et al [**51**], however, found that both P_1 and P_2 were of the same magnitude and two orders of magnitude larger than both the convection and diffusion terms. The difference between P_1 and P_2 was found to drive the secondary flow and this difference was of the same order of magnitude as the convection and diffusion terms. Perkins' [**52**] confirmed the findings of Gessner et al.

Trupp et al [**53**] conducted experiments in isothermal flow in a simulated "infinite" rod bundle with various Reynolds numbers and varying *P/D* ratio. Measurements of the mean primary velocity, five of the six Reynolds stresses and local wall shear stress were made. From these measurements the magnitude of the secondary flows were deduced and shown to be on the order of 1% of the mean primary flow. The orientation of the secondary flow cells are shown for two sub channels in Figure 2-4, where the blue cells represent rotation in the clockwise direction and red cells in the counter-clockwise direction.

Trupp et al's measurement of local wall shear stress showed uniformity within ± 5% in the circumferential direction for all Reynolds numbers and *P/D* ratios. The measurements of the Reynolds stresses were shown to agree fairly well when compared to that of Laufer's [**54**] for pipe flow at a Reynolds number of *41 000.*

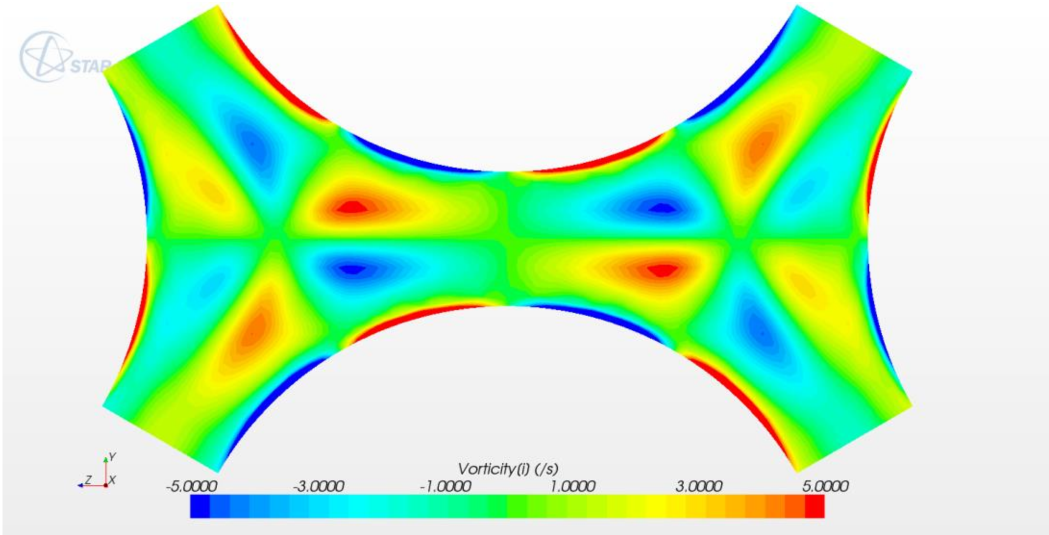

Figure 2-4: Counter-rotating secondary flow cells in two sub channels of a rod bundle

2.2.2 Computational Studies

The previous discussion regarding the experimental work done on secondary flows has highlighted the importance of the two production terms that involve the stresses $\overline{v'^2}$, $\overline{w'^2}$ and $\overline{v'w'}$. Therefore, it is obvious that these terms be accurately modelled.

Launder and Ying [**55**] realized that the prescription of the Reynolds stress tensor given by isotropic EVMs was insufficient in capturing secondary flows. They then derived a model which solves the transport of $\overline{v'^2} - \overline{w'^2}$ and $\overline{v'w'}$. This model was able to predict the magnitude of the secondary flows.

Reece [**56**] employed the famous RSM of Launder et al [**5**]- which acts to solve for each of the six Reynolds stresses by transport equation – to successfully predict the secondary flows seen in the experiments of Melling et al [**57**].

As stated previously, Cheng et al [**42**] used the RSM of Speziale et al [**43**] to model the secondary flows within a rod bundle.

Many authors have employed a non-linear or anisotropic EVM to resolve the secondary flow [**58**] [**59**] . This approach is not further discussed in the interest of brevity.

2.3 Summary

- There exist three regimes for heat transfer to supercritical fluids: (i) NHT (ii) EHT and (iii) DHT.
- The DHT regime is subdivided into two mechanisms: (i) thermally induced bulk flow acceleration and (ii) buoyancy influence.
- The adequate resolution of the boundary layer is of utmost importance for flows involving heat transfer to supercritical fluids. This is due to the drastic change in physical properties at temperatures near T_{pc} and their effect on the heat transfer regime observed. It should be emphasized that turbulence models applied using wall functions have been shown to fail and the models must be integrated to the wall.

- The SST, RNG and RSM turbulence models with a $y+ < 1$ have been identified as capable of predicting the HTC in multiple supercritical heat transfer regimes
- Secondary flows exist in ducts of non-circular cross section. The more complex RSM is needed in order to resolve these secondary motions
- If secondary flows are not resolved (by using a EVM, for example) less lateral mixing may be predicted resulting in larger azimuthal temperature gradients on a rod

Chapter 3

Computational Models

The general form of the EVM and the RSM were introduced in Chapter 1.4.1. The specific form of the SST turbulence model [**34**] as well as the RSM proposed by Launder et al [**5**] will be described in further detail.

In both cases the steady version of these turbulence models was employed because, in the limit of the models studied, there appeared to be no unsteady behaviour.

3.1 The Shear Stress Transport (SST) Turbulence Model [34]

The SST turbulence model was developed by Menter as a means of utilizing the advantages offered by both the standard k-ε and the standard k-ω models. The dissipation of turbulent kinetic energy, ε, is solved in one case and the specific dissipation of turbulent kinetic energy, ω, is solved in the other. Where ω is defined as below:

$$\omega = \frac{\varepsilon}{k} \tag{3.1}$$

And ε is defined as:

$$\varepsilon = \nu \overline{\frac{\partial u_i'}{\partial x_j}\frac{\partial u_i'}{\partial x_j}} \tag{3.2}$$

The standard *k-ε* model is known to be inferior to the standard *k-ω* model in terms of boundary layer predictions whereas the standard *k-ω* is sensitive to freestream values of ω [**4**]. Menter used this knowledge to combine the two models such that the ω transport equation is solved in the near wall region and the ε equation is solved in the freestream with a blending function that acts to transition between the constants used to define each model.

The two transport equations are given below.

$$\frac{\partial k}{\partial t} + U_j \frac{\partial k}{\partial x_j} = -\overline{u_i' u_j'}\frac{\partial U_i}{\partial x_j} - \beta^* k\omega + \frac{\partial}{\partial x_j}\left[(\nu + \sigma_k \nu_t)\frac{\partial k}{\partial x_j}\right] \tag{3.3}$$

$$\frac{\partial \omega}{\partial t} + U_j \frac{\partial \omega}{\partial x_j} = -\frac{\gamma}{\nu_t}\overline{u_i' u_j'}\frac{\partial U_i}{\partial x_j} - \beta\omega^2 + \frac{\partial}{\partial x_j}\left[(\nu + \sigma_\omega \nu_t)\frac{\partial \omega}{\partial x_j}\right] + 2(1 - F_1)\sigma_{\omega 2}\frac{1}{\omega}\frac{\partial k}{\partial x_j}\frac{\partial \omega}{\partial x_j} \tag{3.4}$$

Where the turbulent velocity correlation $\overline{u_i' u_j'}$ is given by the Boussinesq approximation seen in Equation 1.11 and the eddy viscosity is given as:

$$\nu_t = \frac{a_1 k}{\max(a_1\omega; \Omega F_2)} \tag{3.5}$$

Where $\Omega = \frac{\partial U_i}{\partial x_j}$ is the mean strain rate.

The following definitions are used:

$$F_1 = \tanh(arg_1^4) \tag{3.6}$$

$$F_2 = \tanh(arg_2^2) \tag{3.7}$$

$$arg_1 = min\left[max\left(\frac{\sqrt{k}}{0.09\omega y}; \frac{500\nu}{y^2\omega}\right); \frac{4\rho\sigma_{\omega 2}k}{CD_{k\omega}y^2}\right] \tag{3.8}$$

$$arg_2 = max\left(2\frac{\sqrt{k}}{0.09\omega y}; \frac{500\nu}{y^2\omega}\right) \tag{3.9}$$

$$CD_{k\omega} = max\left(2\rho\sigma_{\omega 2}\frac{1}{\omega}\frac{\partial k}{\partial x_j}\frac{\partial \omega}{\partial x_j}, 10^{-20}\right) \tag{3.10}$$

Where y is the wall distance.

The constants of the model can be calculated based on a blend of the *k*-*ω* model and the transformed standard *k*-*ε* model. If SST`s set of constants are given as φ and the set of constants of *k*-*ω* and *k*-*ε* are φ_1 and φ_2, respectively. Then:

$$\varphi = F_1\varphi_1 + (1 - F_1)\varphi_2 \tag{3.11}$$

Where the constants of each model are shown in Table 3-1.

Table 3-1: SST turbulence model constants

$\sigma_{k1} = 0.85$	$\sigma_{\omega 1} = 0.5$	$\beta_1 = 0.075$	$a_1 = 0.31$	$\beta^* = 0.09$	$\gamma_1 = 0.553$
$\sigma_{k2} = 1.0$	$\sigma_{\omega 2} = 0.856$	$\beta_2 = 0.0828$		$\beta^* = 0.09$	$\gamma_2 = 0.440$

It is evident that arg_1 will fall to zero far from any wall as each of the terms go as $1/y$ or $1/y^2$. This is to say that F_1 will go to zero at distances away from walls and therefore the constants of *k-ε* will be used in the freestream and at distances close to walls arg_1 will become very large resulting in $F_1=1$ which will switch the constants to the *k-ω* formulation. This is exactly the desired behaviour to take advantage of each of the model's strengths while minimizing the impact of their weaknesses.

3.2 The Reynolds Stress Model of Launder et al [5]

As mentioned previously in Chapter 1 the RSM has a much more complicated formulation than the EVMs. In addition to the conservation equations, six Reynolds stress transport equations are solved plus an equation for the dissipation of turbulence.

The exact form of the Reynolds stress transport equations has been given in Equation 1.10.

$$\frac{\partial \overline{u_i'u_j'}}{\partial t} + U_j \frac{\partial \overline{u_i'u_j'}}{\partial x_j}$$
$$= -\left(\overline{u_j'u_k'}\frac{\partial U_i}{\partial x_k} + \overline{u_i'u_k'}\frac{\partial U_j}{\partial x_k}\right) - 2\nu \overline{\frac{\partial u_i'}{\partial x_k}\frac{\partial u_j'}{\partial x_k}}$$
$$+ \overline{\frac{p}{\rho}\left(\frac{\partial u_i'}{\partial x_j} + \frac{\partial u_j'}{\partial x_i}\right)} \tag{1.10}$$
$$- \frac{\partial}{\partial x_k}\left(\overline{u_i'u_j'u_k'} - \nu \frac{\partial \overline{u_i'u_j'}}{\partial x_k} + \overline{\frac{p}{\rho}\left[\delta_{jk}u_i' + \delta_{ik}u_j'\right]}\right)$$

The unsteady and convection terms are on the left hand side while the production, dissipation, pressure strain and diffusion terms are on the right hand side. The diffusion term is split into turbulent diffusion, viscous diffusion and pressure diffusion terms.

In order to close the set of equations correlations must be made for the dissipation term, the pressure strain correlation, and the turbulent diffusion term. The viscous diffusion is ignored by assuming a large Reynolds number flow and pressure diffusion is ignored based on the treatment of this term by previous authors.

The turbulent diffusion correlation was approximated by severe simplification of the exact transport equation for $\overline{u_i'u_j'u_k'}$.

$$-\overline{u_i'u_j'u_k'} = c_s \frac{k}{\varepsilon}\left[\overline{u_i'u_l'}\frac{\partial \overline{u_j'u_k'}}{\partial x_l} + \overline{u_j'u_l'}\frac{\partial \overline{u_k'u_i'}}{\partial x_l} + \overline{u_k'u_l'}\frac{\partial \overline{u_i'u_j'}}{\partial x_l}\right] \tag{3.12}$$

The pressure-strain correlation, $\overline{\frac{p}{\rho}\left(\frac{\partial u_i'}{\partial x_j}+\frac{\partial u_j'}{\partial x_i}\right)}$, has been studied by multiple authors and the linear model of Gibson et al [**60**] has been chosen in this work. Many authors noted that by inspection of Poisson's equation governing the pressure fluctuations it is seen that pressure fluctuations are affected by turbulence interactions and mean-strain effects. These are often termed the slow and rapid part of the pressure-strain correlation, respectively. In addition to this, wall reflection terms of the slow and rapid type are included in the correlation. For the sake of brevity the reader is directed to the work of Gibson et al [**60**] as well as the STAR-CCM+ USER GUIDE pg. 3556 [**6**].

$$\overline{\frac{p}{\rho}\left(\frac{\partial u_i'}{\partial x_j}+\frac{\partial u_j'}{\partial x_i}\right)} = \phi_{ij} = \phi_{ij_1} + \phi_{ij_2} + \phi_{ij_{w1}} + \phi_{ij_{w2}} \tag{3.13}$$

The dissipation term is modelled by assuming a state of isotropy for the dissipative scale of turbulence.

$$2\nu\overline{\frac{\partial u_i'}{\partial x_k}\frac{\partial u_j'}{\partial x_k}} = \frac{2}{3}\delta_{ij}\varepsilon \tag{3.14}$$

Therefore the modelled form of the Reynolds stress transport equations can be written as:

$$\frac{\partial\overline{u_i'u_j'}}{\partial t}+U_j\frac{\partial\overline{u_i'u_j'}}{\partial x_j}$$
$$=-\left(\overline{u_j'u_k'}\frac{\partial U_i}{\partial x_k}+\overline{u_i'u_k'}\frac{\partial U_j}{\partial x_k}\right)-\frac{2}{3}\delta_{ij}\varepsilon+\phi_{ij} \tag{3.15}$$
$$+c_s\frac{\partial}{\partial x_k}\frac{k}{\varepsilon}\left[\overline{u_i'u_l'}\frac{\partial\overline{u_j'u_k'}}{\partial x_l}+\overline{u_j'u_l'}\frac{\partial\overline{u_k'u_i'}}{\partial x_l}+\overline{u_k'u_l'}\frac{\partial\overline{u_i'u_j'}}{\partial x_l}\right]$$

The dissipation rate remains as an unknown and its modelled transport equation is given as:

$$\frac{\partial\varepsilon}{\partial t}+U_j\frac{\partial\varepsilon}{\partial x_j}=c_\varepsilon\frac{\partial}{\partial x_k}\left(\frac{k}{\varepsilon}\overline{u_k'u_l'}\frac{\partial\varepsilon}{\partial x_l}\right)-c_{\varepsilon1}\frac{\varepsilon}{k}\overline{u_k'u_i'}\frac{\partial U_i}{\partial x_k}-c_{\varepsilon2}\frac{\varepsilon^2}{k} \tag{3.16}$$

The constants of this model are given in Table 3-2. Note that this form of the ε equation is only solved in regions remote from walls; the so called high Reynolds number formulation.

Table 3-2: RSM turbulence model constants

$c_s=0.11$	$c_\varepsilon=0.15$	$c_{\varepsilon1}=1.44$	$c_{\varepsilon2}=1.9$

The two layer formulation of Wolfstein [**10**] is used in the following study and is given in Appendix A.

Chapter 4

JAEA Experimental Conditions

4.1 Experimental Description

The experiments conducted by the JAEA were done in upward flow of supercritical water in a 7 rod bundle which was electrically heated. The electric heating element was encased with a Boron Nitride insulator and this was contained within a cladding of Inconel 600. Thermocouples were situated into the cladding surface facing the coolant at various azimuthal positions for each rod at various axial positions. Two pressure taps were installed along the test section.

Three experimental cases of the JAEA were chosen as part of the computational benchmark exercise; (i) an isothermal case A1, (ii) a low enthalpy, low heat flux case B1 and (iii) a high enthalpy, high heat flux case B2.

The submission requirements for the computational benchmark exercise will include a pressure drop prediction for the isothermal case A1 and wall temperature predictions for the heated cases B1 and B2.

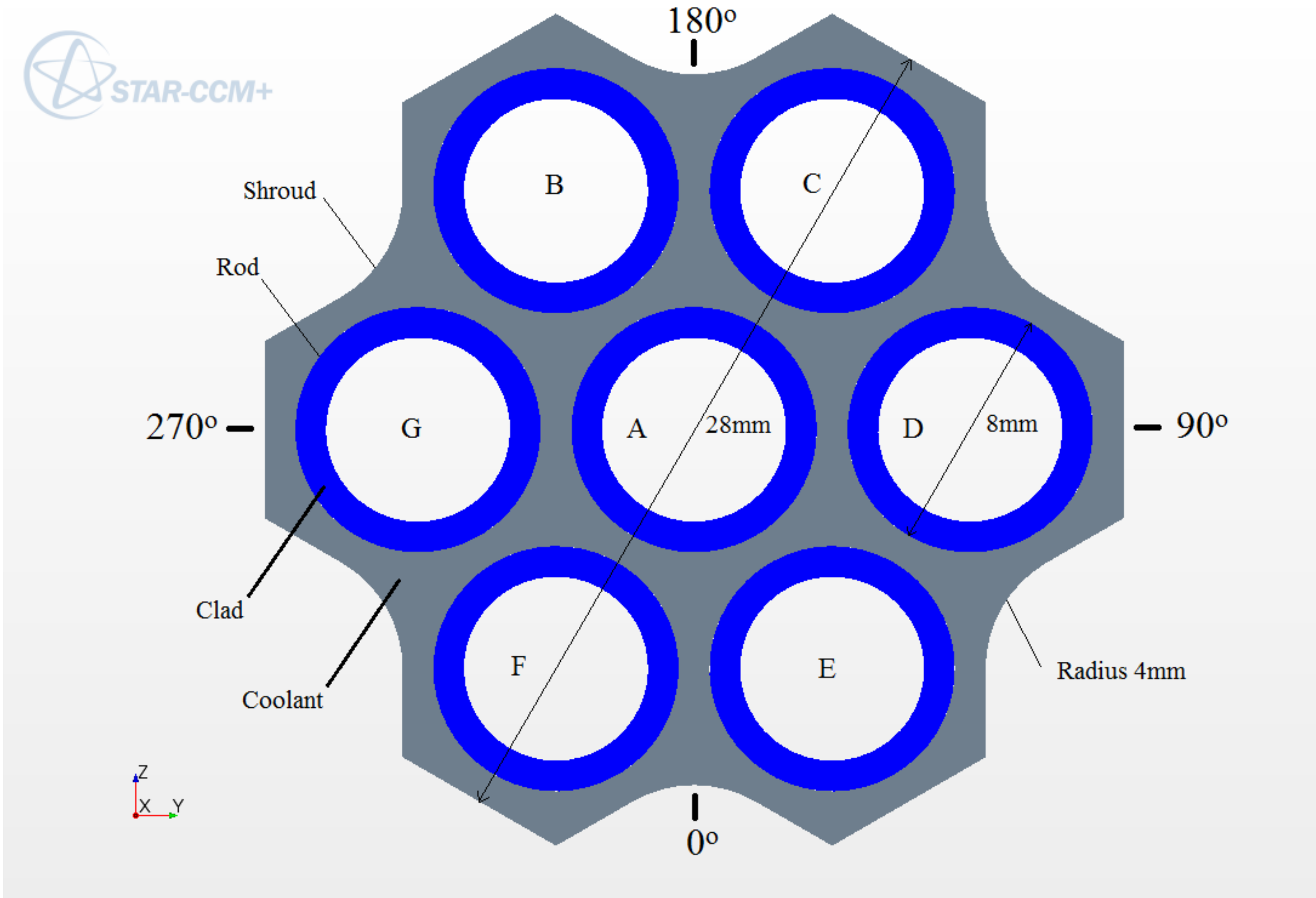

Figure 4-1: 7 rod bundle

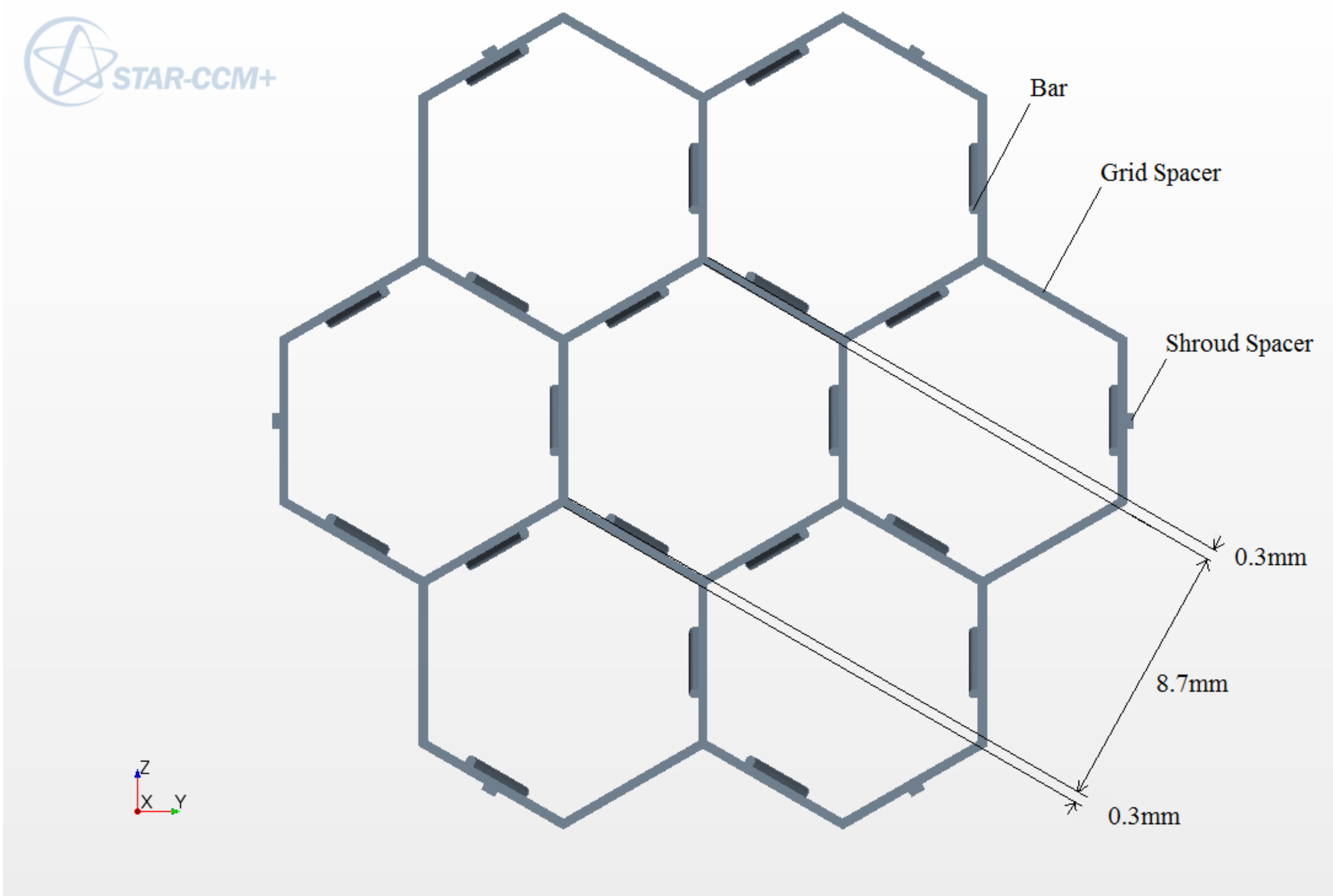

Figure 4-2: Grid spacer

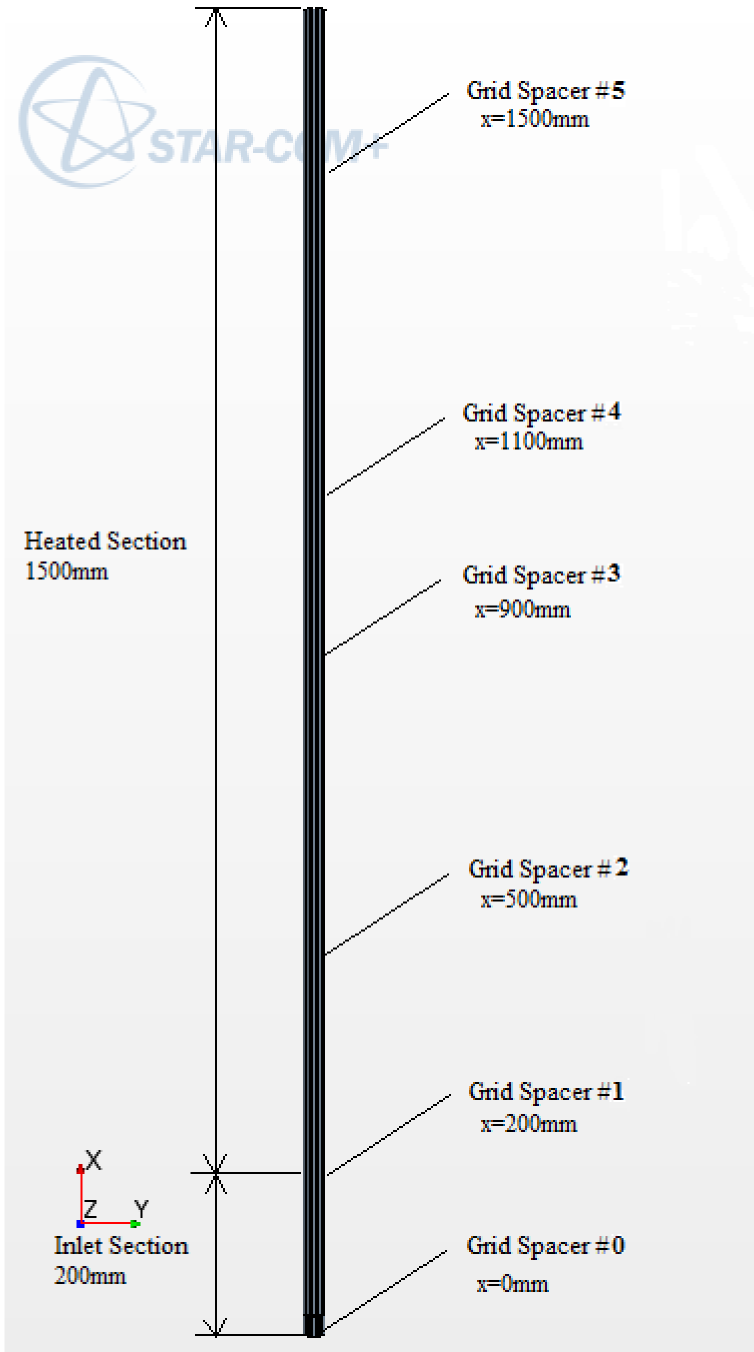

Figure 4-3: Axial snapshot of the JAEA test section

Figure 4-1 shows the cross section of the 7 rod bundle including the clad regions in blue and the coolant region in grey. The rods are arranged in a triangular lattice and are encased by a hexagonal-like shroud.

Figure 4-2 shows the grid spacer geometry which includes stabilizing bars that face the rod surfaces and shroud spacers that face the shroud surface. There are a total of six grid spacers that are situated along the test section as shown in Figure 4-3.

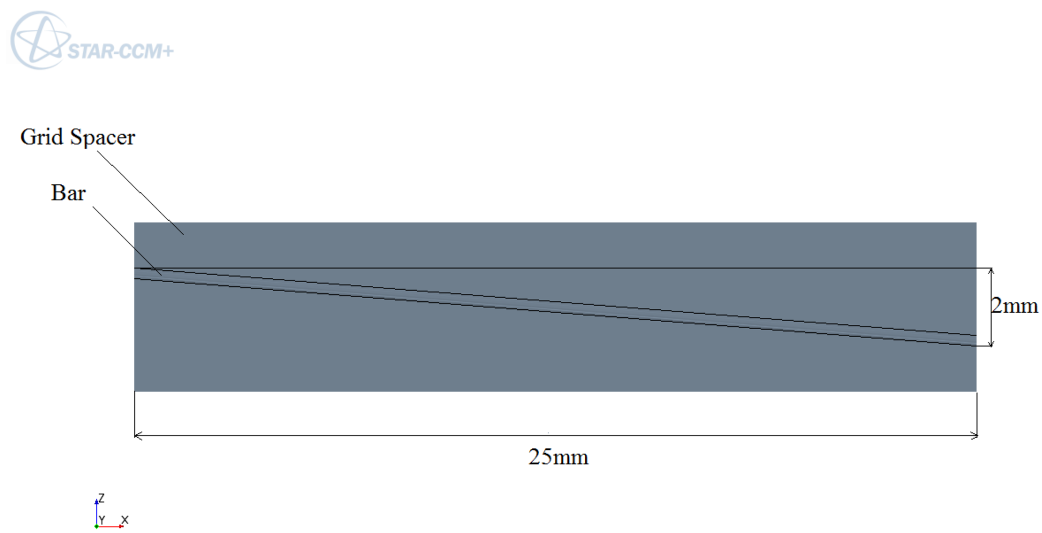

Figure 4-4: Side view of the grid spacer wall

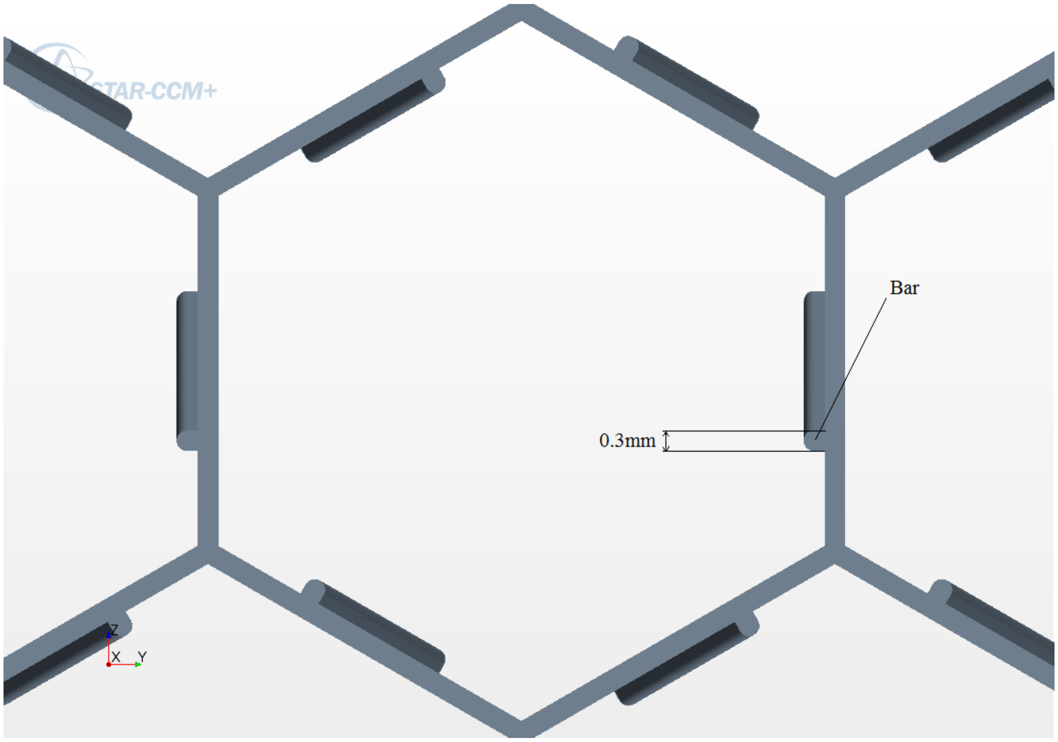

Figure 4-5: Detailed view of the grid spacer

Figure 4-4 shows the orientation of the stabilizing bar at an angle to the axial direction. This can also be seen in Figure 4-5 with a detailed view of the grid spacer.

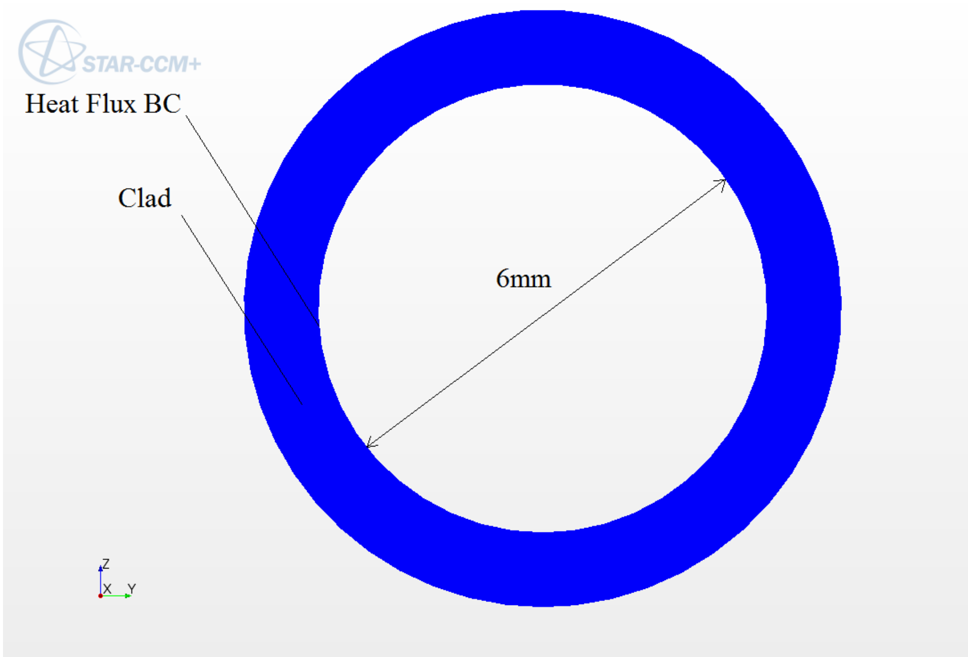

Figure 4-6: Detailed view of rod including clad

Figure 4-6 shows a detailed view of the rod structure including the clad.

The experimental results of the JAEA are split into two parts. First, a pressure drop measurement was made for the isothermal case A1. And secondly, temperature measurements were made at the various thermocouple positions along the test section for the heated cases B1 and B2. The measurement locations can best be summarized with reference to Figure 4-7 included in the benchmark exercise conditions and also available in [**61**].

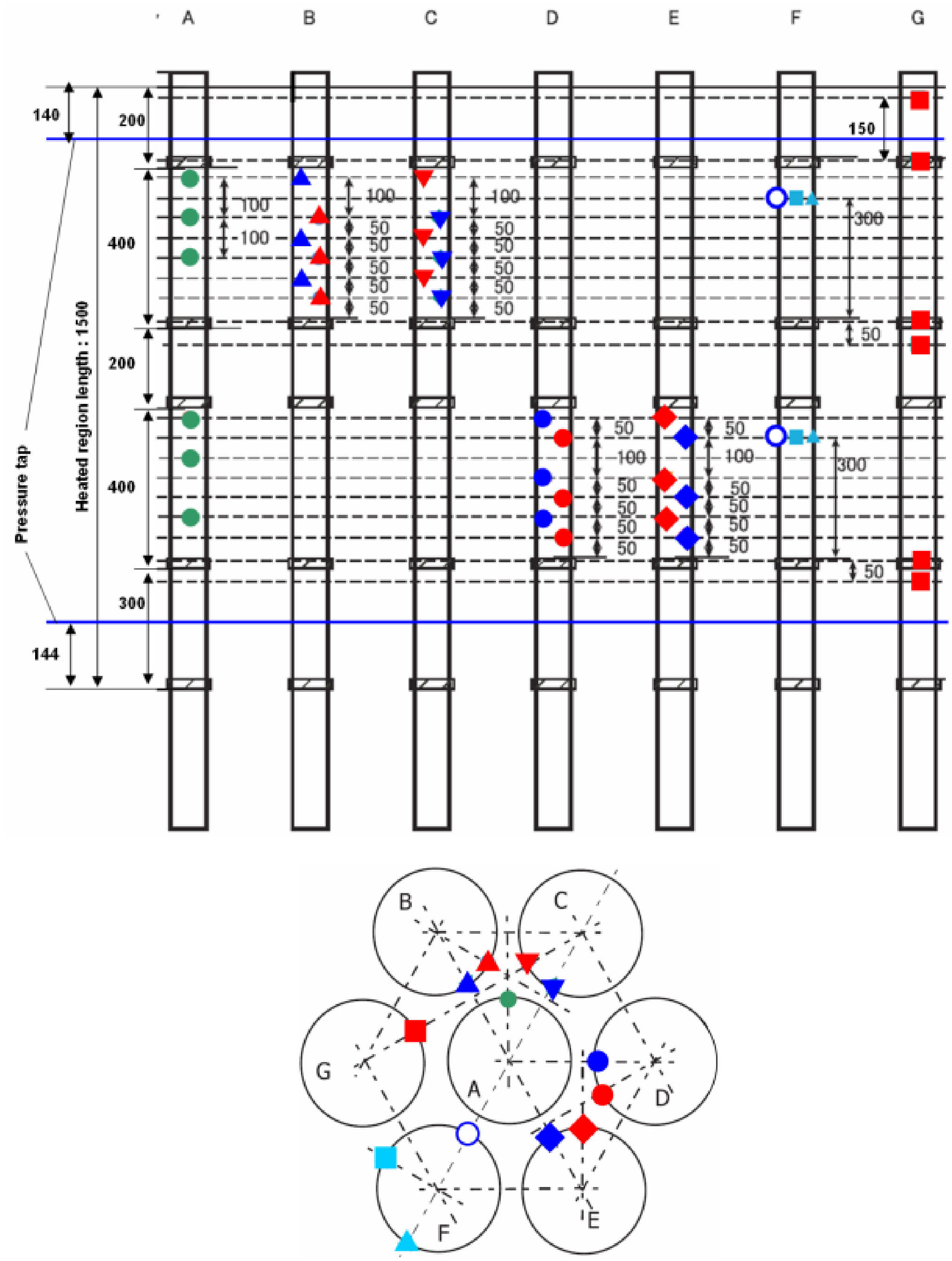

Figure 4-7: Pressure tap and thermocouple positions for final submission [61]

The boundary conditions of the experimental cases are shown in Table 4-1 and Table 4-2

Table 4-1: Isothermal experimental conditions

Case	Inlet Temperature (K)	Inlet Pressure (MPa)	Mass Flux (kg/m^{2}s)
A1	297.35	25.0	2283.44

Table 4-2: Heated experimental conditions

Case	Inlet Temperature (K)	Inlet Pressure (MPa)	Mass Flux (kg/m^{2}s)	Heater A (kW)	Heater B, D, F (kW)	Heater C, E, G (kW)
B1	353.58	24.98	1447.56	19.67	22.51	22.52
B2	519.58	25.03	1432.97	34.14	34.08	34.13

4.2 Computational Model Description

The modelled geometry includes minor modifications that were made in the interest of ensuring a high quality computational grid as well as reducing computational resources.

4.2.1 Stabilizing Bar Geometry

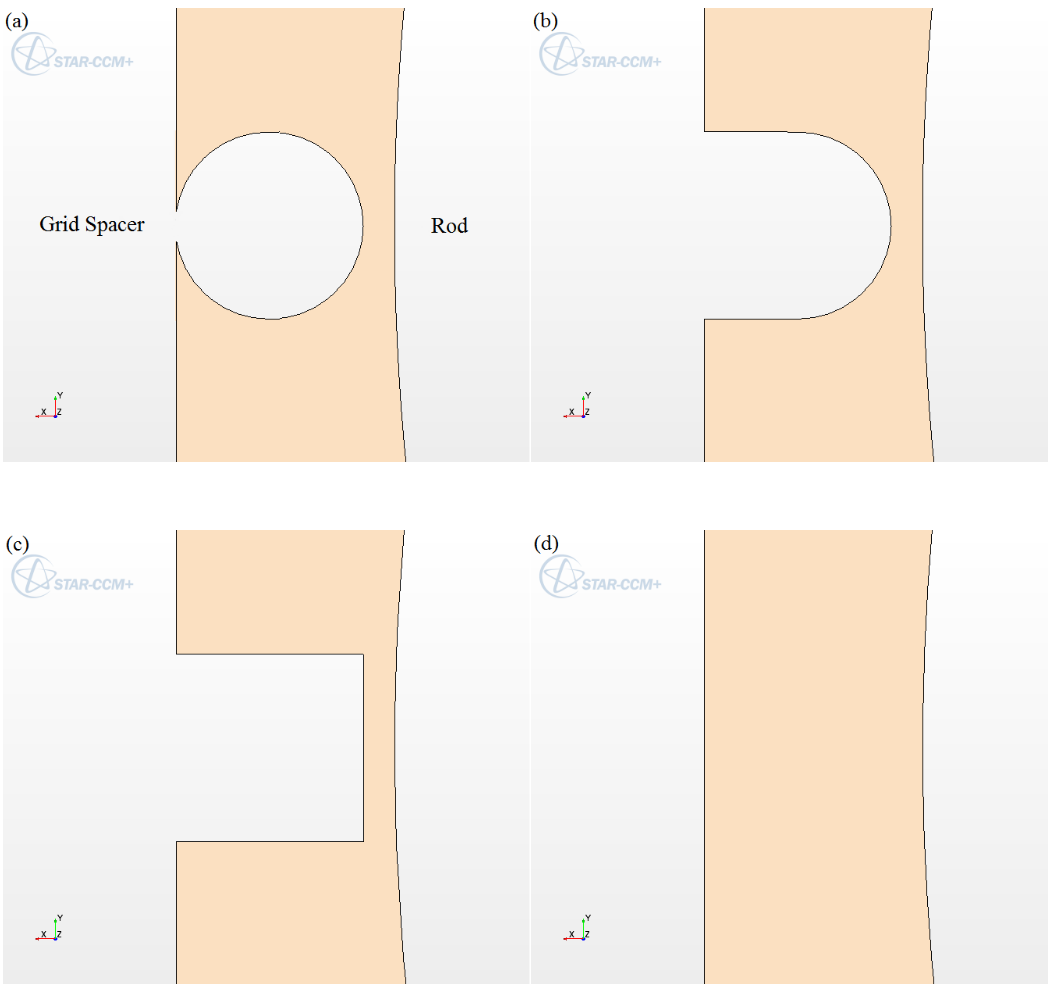

Figure 4-8: Various bar geometries: (a) Actual Bar, (b) Round Bar, (c) Square Bar and (d) No Bar

The effect of the bar geometry was studied in both isothermal and heated conditions. The geometries studied are shown in Figure 4-8 . The actual geometry of the bar was found to be infeasible to model owing to the very low quality mesh cells that were created in the region where the bar meets the grid spacer wall.

Part of the study was done using a one-third grid spacer cell in an effort to reduce computation time. This geometry utilized rotational periodicity as well as a fully developed boundary condition connecting the inlet and outlet; this is shown in Figure 4-9.

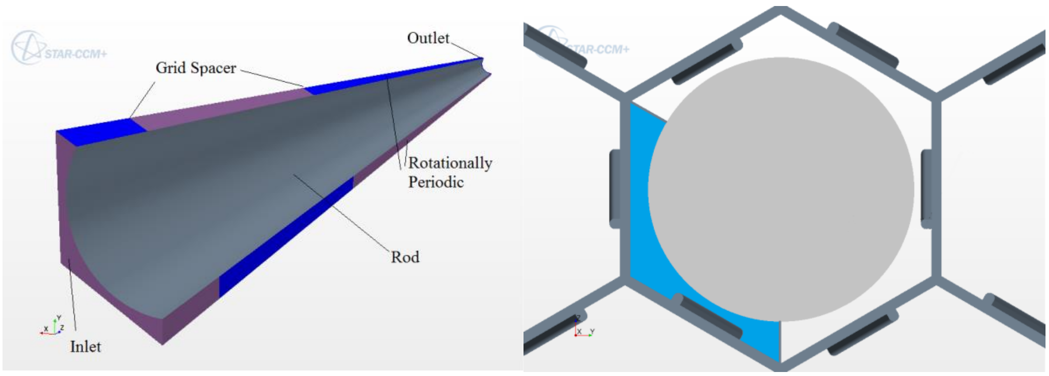

Figure 4-9: One-third grid spacer cell

To examine the consequence of the change in geometry at isothermal conditions rod wall shear stress contour plots are shown in Figure 4-10.

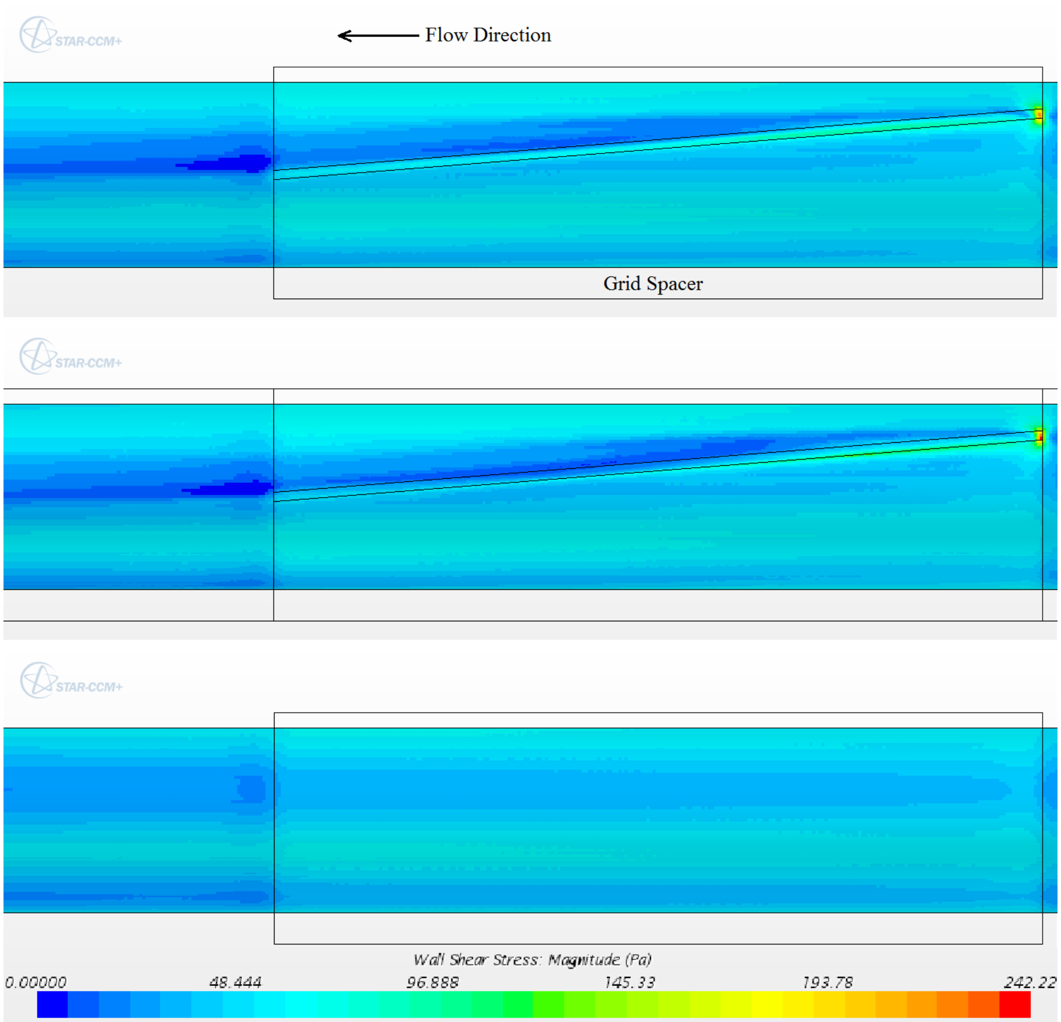

Figure 4-10: Rod wall shear stress contour plots of various bar geometries; from top to bottom, Round Bar, Square Bar, No Bar

The wall shear stress of the "Round Bar" and "Square Bar" are nearly identical. Both of the geometries show a peak at the upstream edge of the grid spacer at the location of the bar. This is due to the abrupt change in flow cross section causing a spike in velocity in that region. There also exists a low wall shear stress region or "wake" on the diverging side of the bar pictured in dark blue in Figure 4-10.

This "wake" continues downstream of the grid spacer and is not present in the results of the "No Bar" geometry.

It has been shown that the "Round Bar" and "Square Bar" geometries give nearly identical results for local rod wall shear stress. In keeping as close to the actual geometry of the experiments, the "Round Bar" geometry is chosen for further comparison with the "No Bar" geometry.

The effect of the bar geometry on pressure drop at isothermal conditions is studied using the one-third rod bundle; the geometry and the boundary conditions are shown in Figure 4-11. The pressure drop across the grid spacer with and without the round bar was calculated and the results appear in Table 4-3. The pressure drop predictions were measured between two planes that were placed 5 mm and 125 mm, upstream and downstream of the grid spacer, respectively.

Table 4-3: Pressure drop across the grid spacer with/without a round bar

Geometry	**Pressure Drop (kPa)**
Round Bar	*12.063*
No Bar	*11.609*

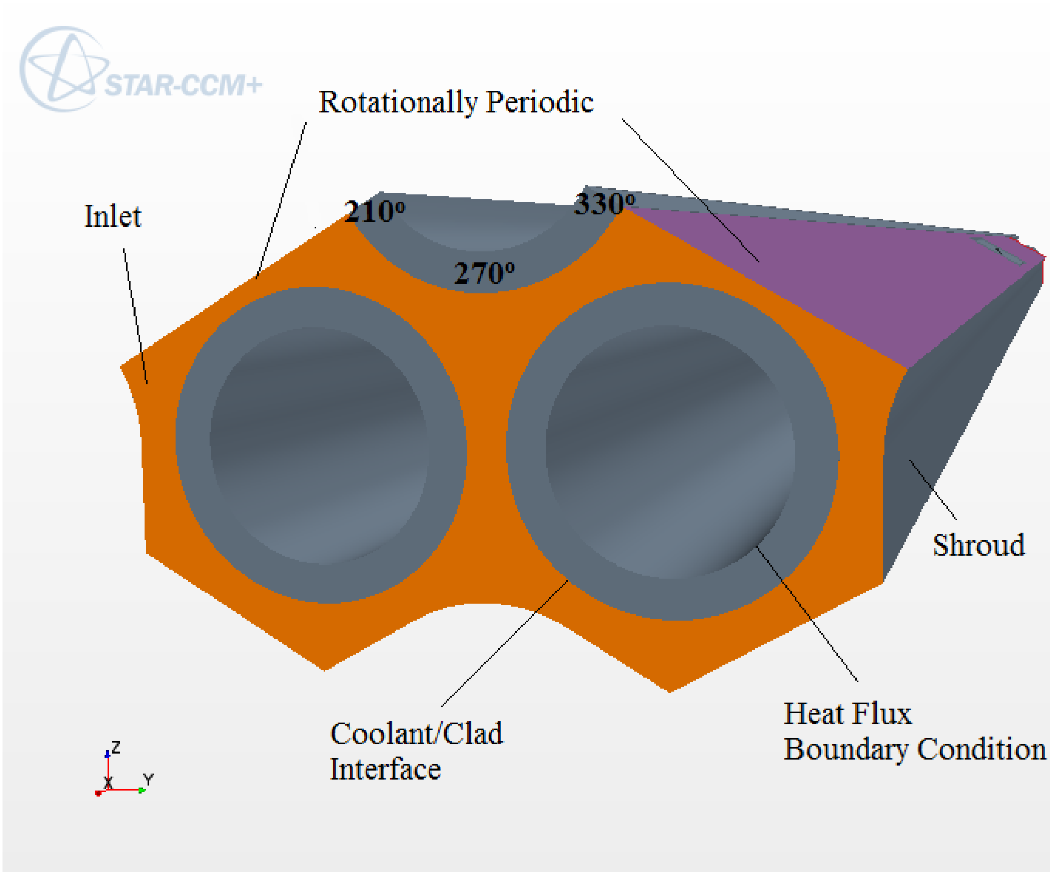

Figure 4-11: One-third rod bundle geometry and boundary conditions

The pressure drop results of the two grid spacer geometries disagree by ~4%. This is not a sizable disagreement.

The effect of the grid spacer geometry on wall temperature is studied using the boundary conditions of the heated case B2. Figure 4-12 shows the wall temperature along the surface of the centre rod at the azimuthal position of *300°* (see Figure 4-11). The simulations that produced these calculated wall temperatures considered only one axial section of the test section. It was estimated that T_w would pass through T_{pc} (*658* K) in very close proximity to the 4th spacer seen in Figure 4-3 and Figure 4-7. Therefore, owing to the large property gradients that are expected in this region, this section's wall temperature was assumed to be most sensitive to changes in geometry. Using only the most sensitive section instead of simulating the entire test section contributed to very large savings in computational resources.

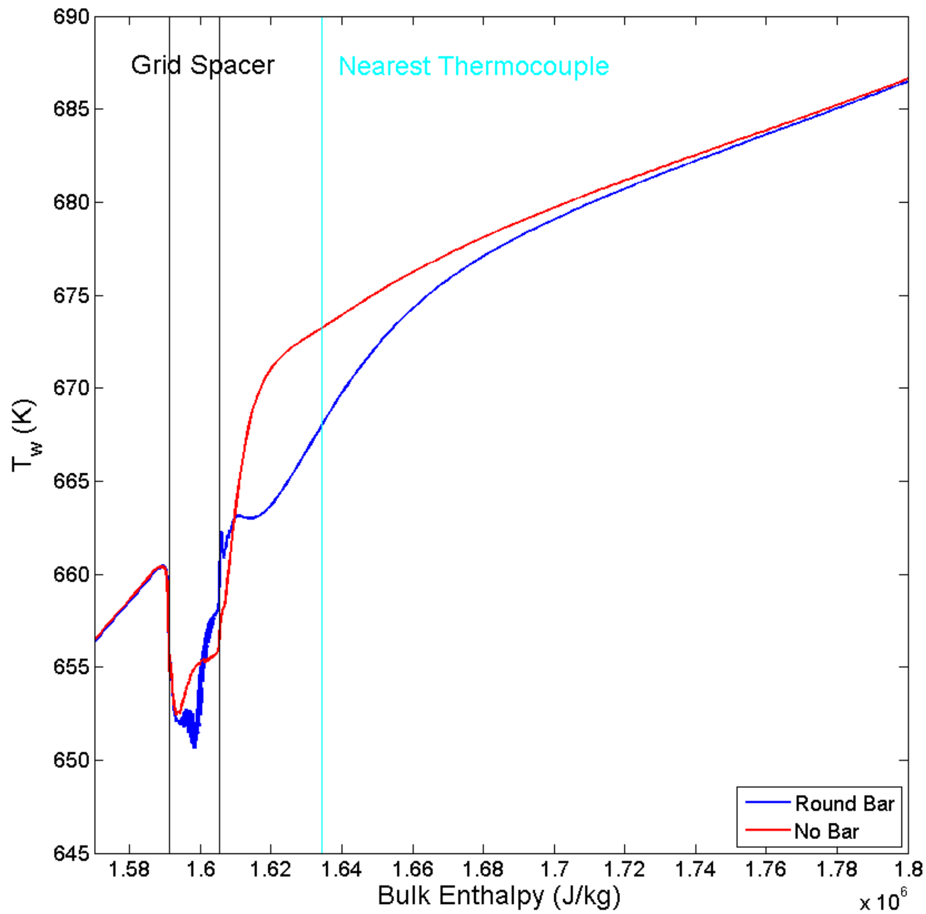

Figure 4-12: T_w vs. Bulk Enthalpy of the 4th grid spacer section along the *300°* azimuthal position of the centre rod

To simulate only this section a plug flow was attached *300 mm* upstream of the spacer and allowed to develop hydro-dynamically. The heat flux was applied *100 mm* upstream of the grid spacer.

The results given in Figure 4-12 show that heat transfer is improved within the grid spacer, regardless of the geometry. However, the “No Bar” grid spacer does not act to improve the heat transfer in the downstream region, as does the “Round Bar” grid spacer. In fact, downstream of the “No Bar” grid spacer there appears to be an impairment of heat transfer. This behaviour was also seen in computations done by Zhu et al [**62**]. A reference to the nearest thermocouple is included to show that the temperature predictions in the near downstream region disagree by up to *5* K yet the far downstream temperature predictions would be unaffected.

Due to the effect of the bar in both pressure drop, rod wall shear stress and wall temperature predictions, the “Round Bar” geometry is chosen in keeping with a close approximation to the true experimental geometry. In addition, this decision is made with the knowledge that the use of the “No Bar” geometry offers no significant improvement in mesh size, convergence and therefore computation time, thus the inclusion of this detailed structure comes without detriment.

4.2.2 Inlet Boundary Condition

The effect of inlet condition was studied in both isothermal and heated conditions. The focus was placed on determining the necessity of the inclusion of the zeroth grid spacer (Grid Spacer #0 in Figure 4-3), which lies upstream of the heated section.

This study was done using the one-third rod bundle geometry of Figure 4-11. The inlet conditions considered are shown schematically in Figure 4-13. Case (a) represents the assumption that the flow returns to a fully developed state after a certain downstream distance from the grid spacer. Case (b) represents the nearest approximation to the experimental geometry. If the assumption of case (a) is correct then the zeroth grid spacer may be neglected.

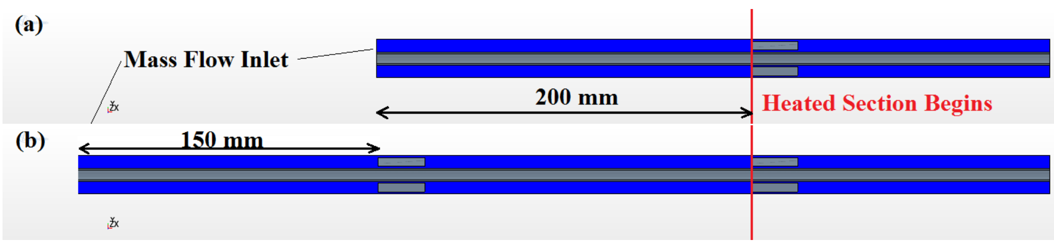

Figure 4-13: Inlet condition sensitivity boundary conditions (a) Without 0th grid spacer (b) With 0th grid spacer

The first study was completed at isothermal conditions using the boundary conditions of Case A1 shown in Table 4-1. The calculated pressure drops across the 1st grid spacer given by the two cases agree within *0.1%*, as shown in Table 4-4.

Table 4-4: Pressure drop across the 1st grid spacer with/without the 0th grid spacer

Geometry	**Pressure Drop (kPa)**
Without 0^{th} grid spacer	*12.063*
With 0^{th} grid spacer	*12.049*

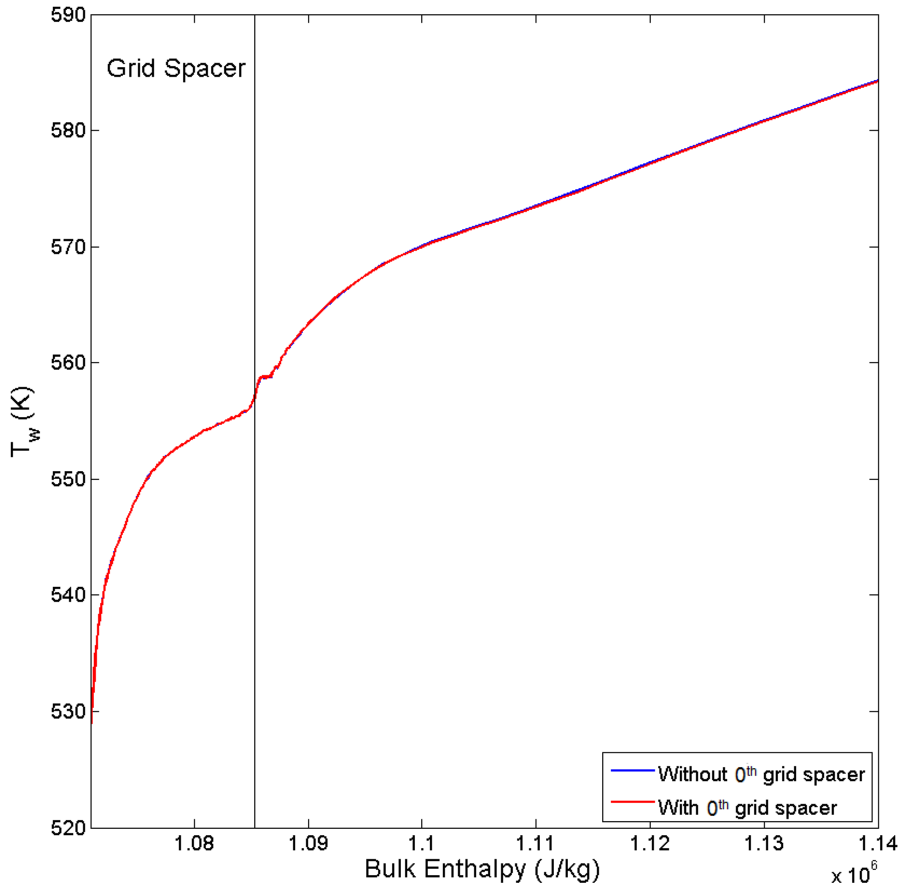

Figure 4-14: T_w vs. Bulk Enthalpy along the *240°* azimuthal position of the centre rod

The effect of the inlet condition is further explored using the boundary conditions of case B2. Figure 4-14 shows that the wall temperature distribution through and downstream of the first grid spacer within the heated section is insensitive to the inclusion of the zeroth grid spacer which lies upstream of the heated section. Due to the insensitivity, the zeroth grid spacer will be neglected and all experimental cases will be modelled as shown in Figure 4-13 (a).

It is noted that there is peculiar behaviour immediately downstream of the grid spacer where the wall temperature is seen to have an abrupt increase. This behaviour is thought to be due to the complex flow that exists at the rod wall when the stabilizing bars of the grid spacer are encountered. Similar behaviour was also observed in [**62**]. However, a precise explanation is beyond the scope of this study.

4.2.3 Heat Flux Boundary Condition

A heat flux boundary conditions was applied to the inner surface of the Inconel 600 cladding as shown in Figure 4-6 and Figure 4-11. The physical properties of the Boron Nitride insulator were not available to the benchmark participants and therefore the insulator was not included in the modelled geometry.

Chapter 5

Separate Effects Study

A separate effects study, as mentioned previously in Chapter 1.4.2, is performed when analyzing a complex flow in which there is little to no experimental data available. A separate effects study acts to isolate the physical phenomena deemed important by the CFD analyst. In this chapter the physical phenomena of an upward flow of supercritical water in a 7 rod bundle which was electrically heated are identified and subsequently studied through multiple validation cases.

The strengths of two candidate turbulence models will be explored in the following validation cases. The SST turbulence model [**34**] and the linear pressure strain, two layer RSM [**5**] [**60**] [**10**] represent the two fundamental types of RANS based models; the EVM and RSM, respectively. These turbulence models were chosen based on their representation in the literature reviewed in Chapter 2.

5.1 Heat Transfer to the Supercritical Turbulent Boundary Layer

The study of the heat transfer to the supercritical turbulent boundary layer was deemed extremely important to the prediction of the wall temperature. It has been noted that the prediction of the HTC for flows of supercritical water are highly dependent upon the distribution of specific heat, density, thermal conductivity and viscosity which are a strong function of temperature especially in the proximity of T_{pc}. Therefore it is of primary concern to properly resolve the boundary layer and the temperature gradient in the very near wall region in order to accurately represent the physical property distributions and therefore accurately predict the HTC.

Table 5-1: Boundary conditions of the Yamagata et al [23] validation case

Pressure (MPa)	*24.5*
Mass Flux (kg/m^{2}s)	*1260*
Heat Flux (kW/m^2)	*465*
Tube Diameter (mm)	*7.5*
Enthalpy Range (kJ/kg)	*1478.7 – 2650.0*

In the interest of isolating the heat transfer to the supercritical turbulent boundary layer from any other effects that could influence the HTC the experiments of Yamagata et al [**23**] were chosen as an appropriate validation case. The experiments of Yamagata et al were done for upward, downward and horizontal flow of supercritical water flowing in a tube. Measurements of wall temperature were made for a variety of heat and mass fluxes. The boundary conditions for the case studied are shown in Table 5-1.

This case in particular was chosen because it is shown to lie far from regions of thermally induced bulk flow acceleration and buoyancy influence as determined by the threshold parameters of Moretti et al [**25**] and Mikielewicz et al [**26**], respectively . These parameters are similar to the cases of the JAEA as shown in Table 5-2.

Table 5-2: Threshold parameters of Yamagata et al [23**] compared to the cases of the JAEA**

Parameter	**Yamagata et al**	**JAEA B1**	**JAEA B2**	**Threshold**
Bo*	*1E-9 – 4E-8*	*1.4E-8 – 2.3E-8*	*6E-10 – 2.6E-8*	*> 6E-7*
K_v	*0.4E-9 – 1.2E-8*	*1E-8 – 1.6E-8*	*1.2E-8 – 3.2E-8*	*> 3.5E-6*

It is noted that these threshold parameters, Bo^* and K_v, were developed based on experiments done in tubes and converging ducts, respectively and caution should be used when applying these parameters to rod bundle flows.

5.1.1 Computational Parameters

The axisymmetry of the tube geometry was exploited and this allowed the computations to be solved on a two dimensional axisymmetric domain. A hydrodynamically fully developed inlet profile was calculated and velocity and turbulence parameters were passed from the fully developed profile to the inlet of the heated section. The inlet temperature was held at 600K, corresponding to an inlet enthalpy of 1478.7 kJ/kg. The outlet of the test section was defined as a pressure outlet and an adiabatic section of 16 D_h was attached downstream of the heated section in order to avoid the outlet boundary condition having an impact on the flow. The physical properties were linearly interpolated between the data from the National Institute of Standards and Technology (NIST).

In order to establish a verified solution the discretization error is examined by analysing the results given by subsequently finer meshes. Multiple meshes are created by varying three mesh parameters, (i) the distance from the wall that the first node is to be placed ($y+$), (ii) the ratio at which that distance increases as nodes are placed towards the bulk of the flow (RGR) and (iii) the degree of axial refinement. For a given $y+$ and RGR, the axial aspect ratio (axial refinement) will determine the final mesh size. The mesh parameters studied are shown below in Table 5-3.

Table 5-3: Mesh parameters used to determine a verified solution

y+	*< 0.05, <0.15, <0.3*
RGR	*1.1, 1.19, 1.28*
Aspect Ratio	Up to *10 000*

5.1.2 Mesh Sensitivity Studies

The axial refinement sensitivity was examined using aspect ratios of up to *10000*. It was found that results were independent of axial refinement up to an AR = *10000*. The simulations used constant axial refinement, while an additional simulation was done that was meshed very finely in the axial region where T_w was expected to pass through T_{pc}. Therefore, very high aspect ratios can be chosen as optimal in order to reduce computational effort. Although this is generally not good practice, the simulations showed that residual convergence criteria were met.

The results of the sensitivity studies are that of the SST turbulence model. The results obtained using the RSM were similar and are therefore omitted.

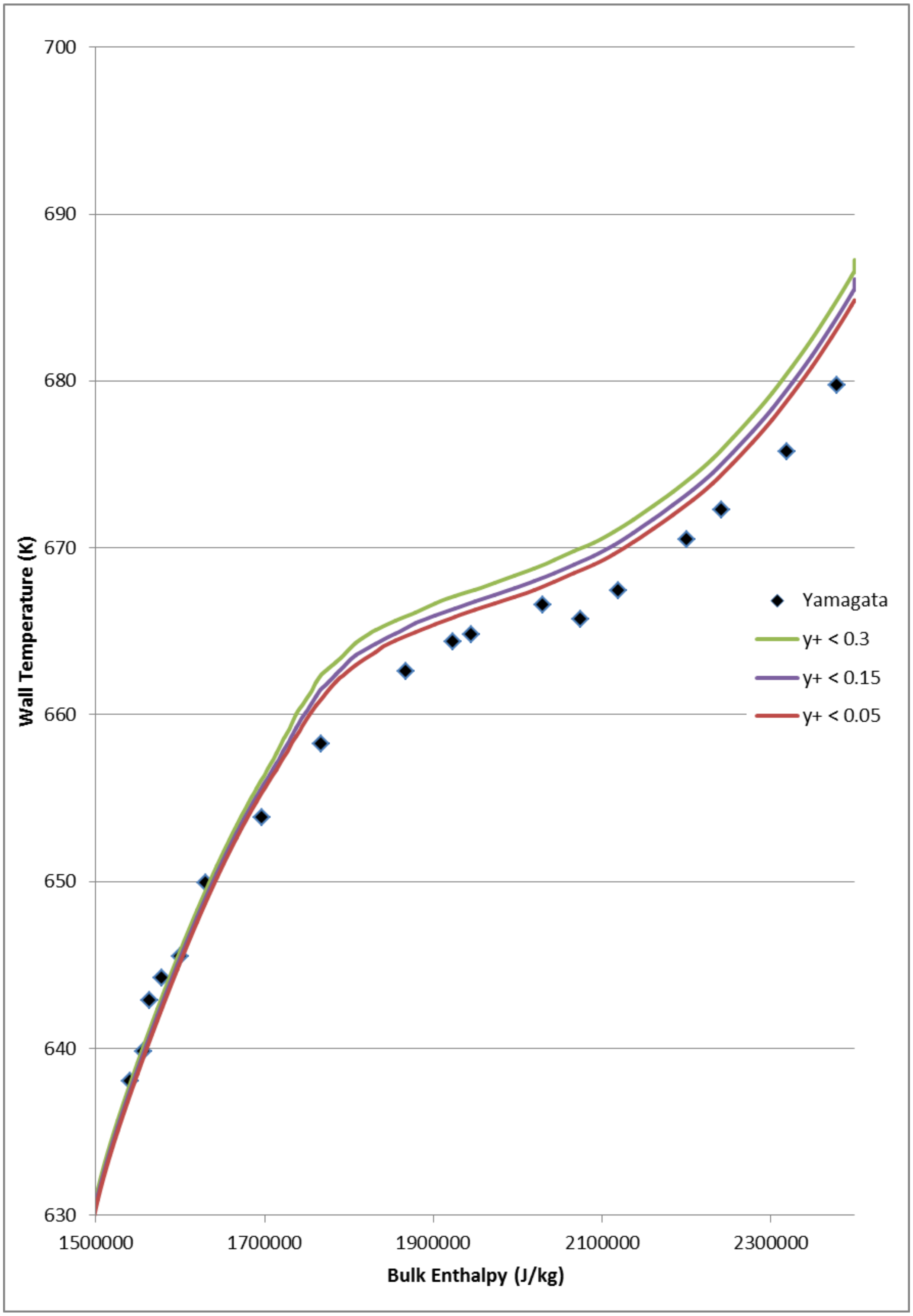

Figure 5-1: T_w vs. Bulk Enthalpy for various *y*+ values at RGR = *1.28*

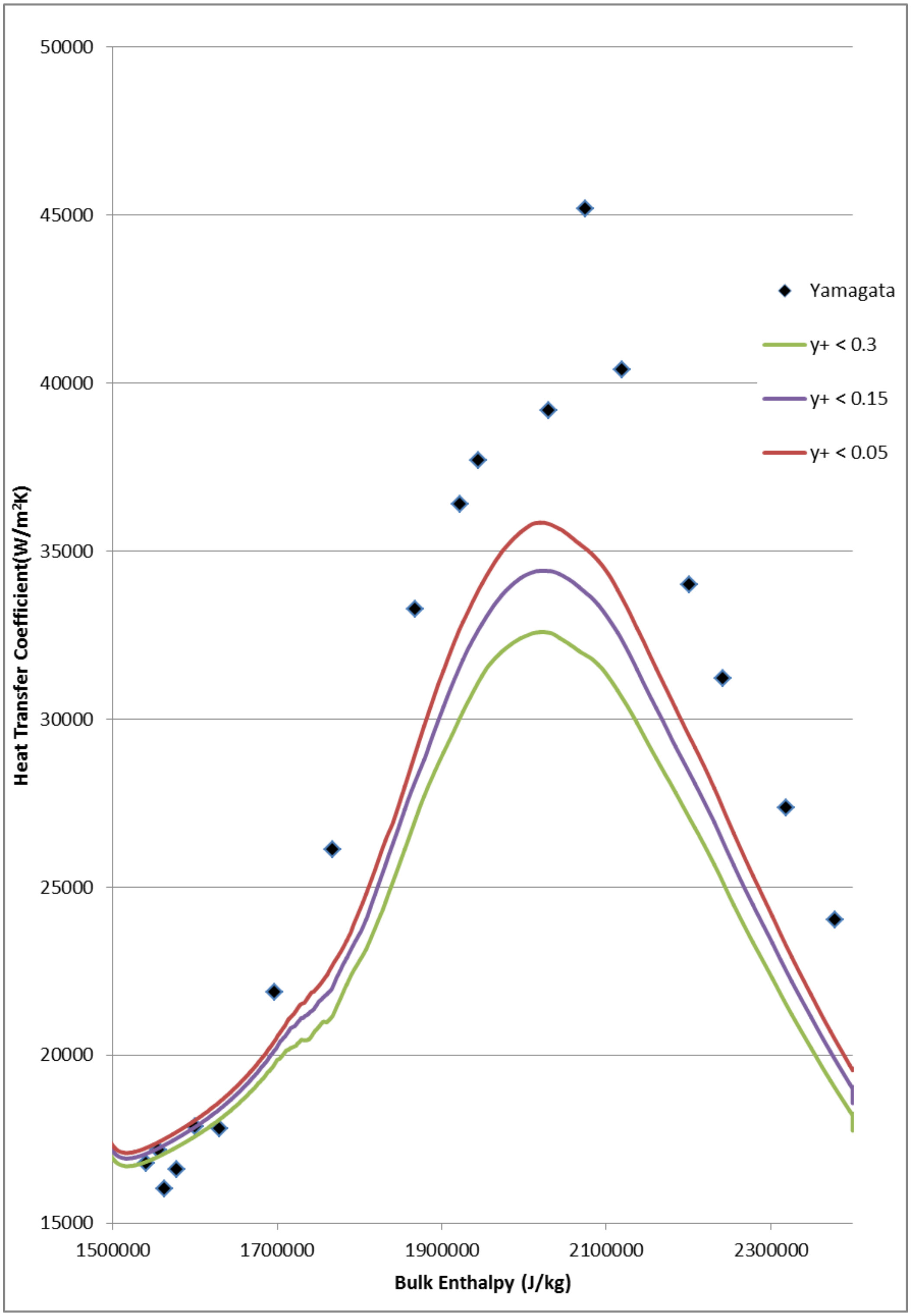

Figure 5-2: HTC vs. Bulk Enthalpy for various *y+* values at RGR = *1.28*

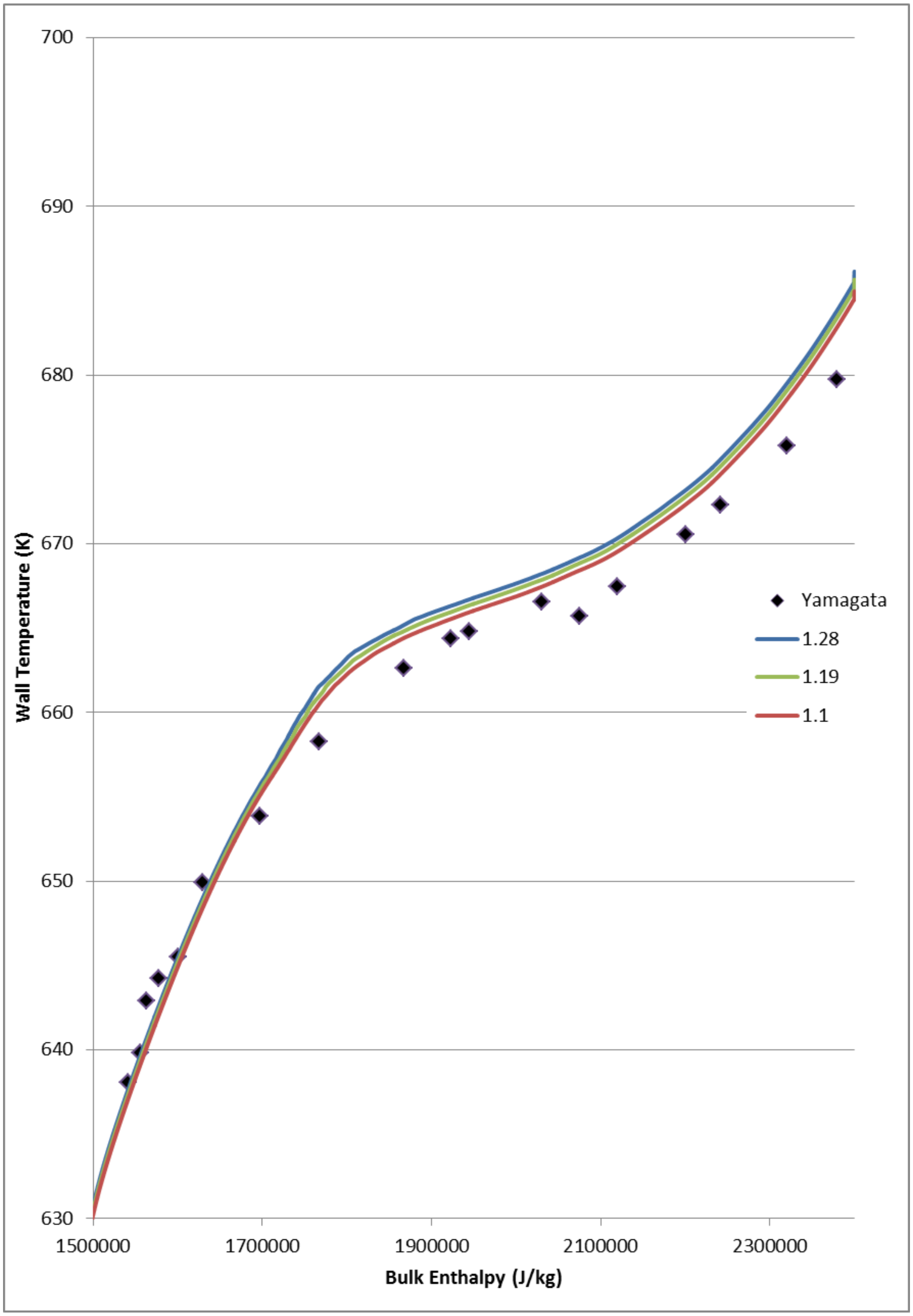

Figure 5-3: T_w vs. Bulk Enthalpy for various RGR values at *y+ < 0.15*

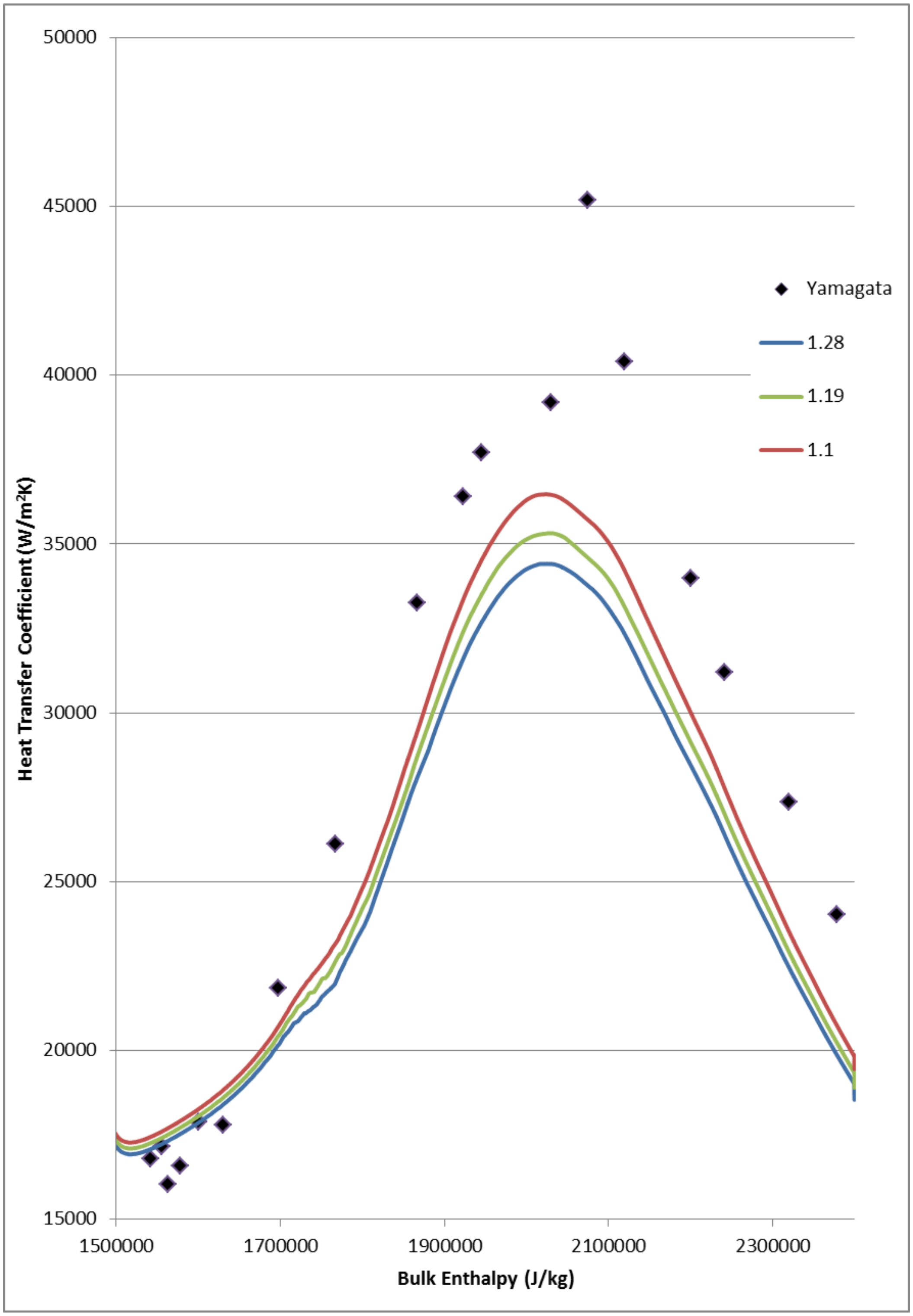

Figure 5-4: HTC vs. Bulk Enthalpy for various RGR values at *y+ < 0.15*

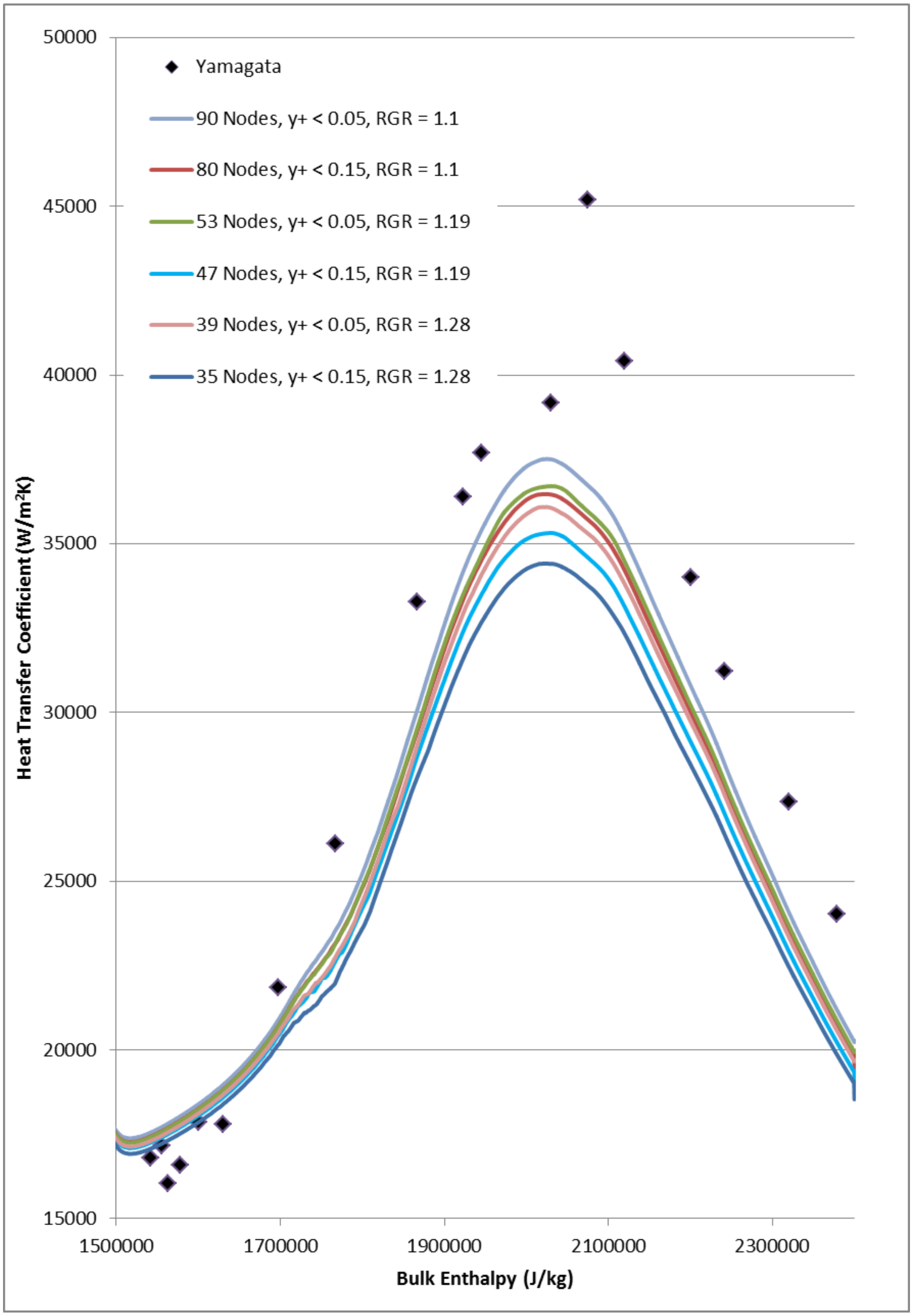

Figure 5-5: HTC vs. Bulk Enthalpy for various combinations of *y*+ and RGR

y+ sensitivity was studied using a RGR = *1.28*. The results of this study are shown in Figure 5-1 and Figure 5-2 with predictions of wall temperature distribution and heat transfer coefficient distribution, respectively. Based on these results it was determined that a *y+ < 0.15* was effective in resolving the heat transfer to the boundary layer but there remained some sensitivity as the *y+* was reduced.

In Figure 5-2 the predictions show an unexpected decrease in HTC at the lowest enthalpy studied as well as peculiar behaviour seen at an enthalpy of *1700000 J/kg*. In the first case normally entrance effects would cause increases in the HTC. In the second case the change in slope observed was not expected. The origins of these behaviours are not known and should be considered in future studies.

RGR sensitivity was then analysed using a *y+ < 0.15.* The wall temperature distribution and heat transfer coefficient distribution are shown in Figure 5-3 and Figure 5-4, respectively.

It is noted that the results are slightly less sensitive to RGR as compared to *y+*. With the simulations of *y+ < 0.3* excluded it is warranted to compare the results on the basis of the computational resources required. This is seen in Figure 5-5 where the number of nodes that span the radius of the tube are noted as well.

It can be seen that the results are not quite mesh independent. As expected, the mesh with the smallest *y+* and lowest RGR gives the highest peak of HTC.

However, further refining the mesh was deemed not suitable as increasing the number of nodes resulted in diminished returns. For example, an improvement in prediction accuracy of ~4% is seen from increasing the number of radial nodes from 39 to 90, yet this resulted in a computational increase of 400%.

In general the meshes with a lower $y+$, regardless of RGR, perform better than their counterparts and, therefore, the conclusion of this mesh sensitivity study was to adopt $y+ < 0.05$ and a RGR = 1.28 as this option offered comparatively moderate computational resources while maintaining predictive accuracy.

5.1.3 Validation Study

It is evident that the experimental case of Yamagata et al studies the EHT regime. Therefore, a turbulence model's ability to predict the physical property distribution in the near wall is directly proportional to its prediction accuracy in this regime. This is due to the variable property mechanism for EHT described by Jackson [**22**] previously in Chapter 2.1.1.2.

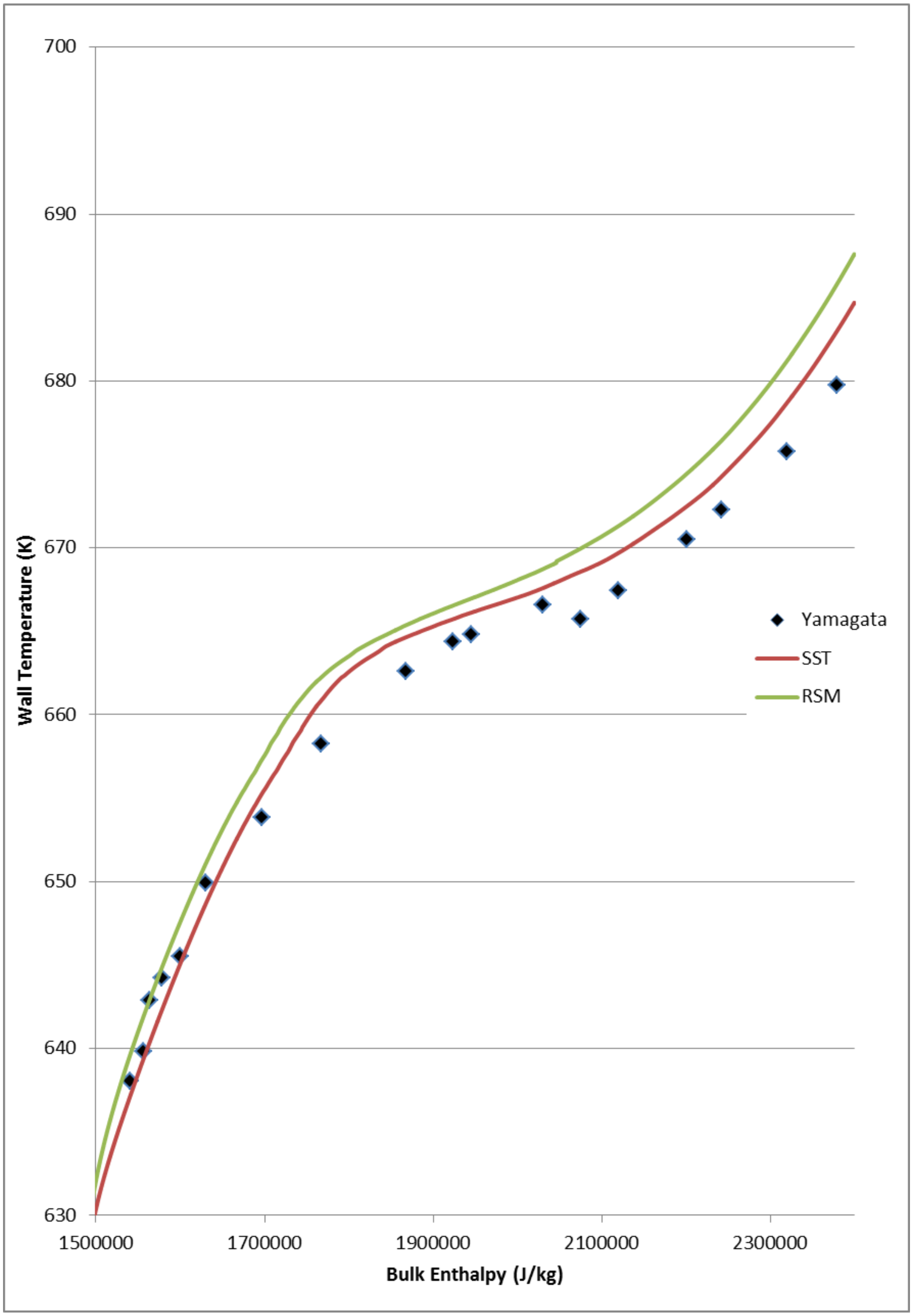

Figure 5-6: T_w vs. Bulk Enthalpy comparison of SST, RSM and Yamagata

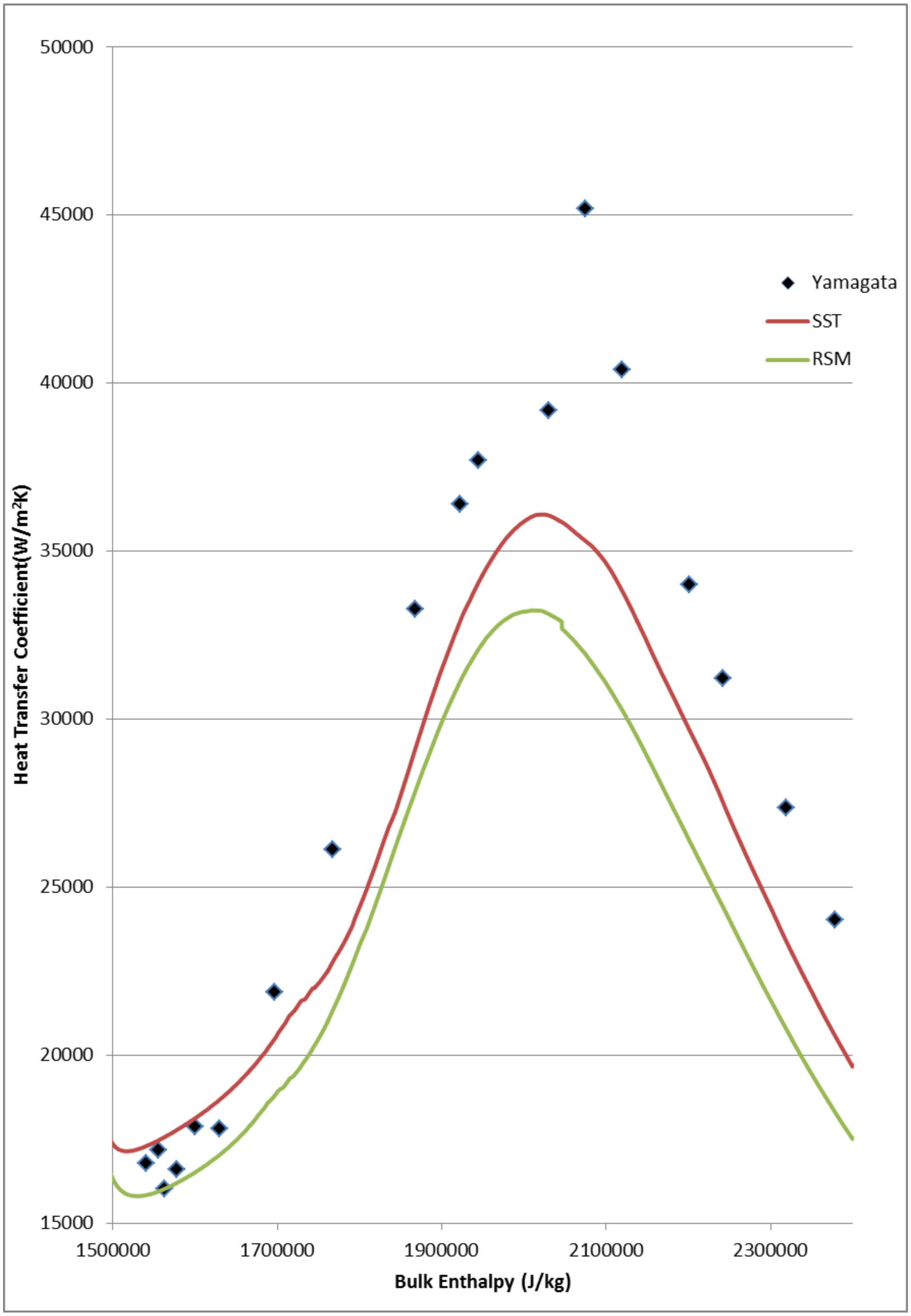

Figure 5-7: HTC vs. Bulk Enthalpy comparison of SST, RSM and Yamagata

The verified solutions of SST and RSM are given in Figure 5-6 and Figure 5-7. The two models accurately predict the location of the HTC peak slightly upstream of where the bulk temperature passes through T_{pc}. However, both models under-predict this peak with SST performing slightly better. This discrepancy is only that of a few degrees K. It is hypothesized that the improved prediction of SST is due to the solution of the ω equation near wall instead of the ε equation. In this situation, the SST turbulence model is chosen as superior as it offers a slightly better prediction of HTC while requiring half the computation time.

5.2 Flows in Channels of Non-Circular Cross Section

The flow through channels of non-circular cross section has long been known to have a complex flow structure. The presence of secondary flows and the anisotropic turbulent field that produces them has been introduced in Chapter 2.2. Secondary flows act to increase convection of momentum and heat throughout the flow channel and this increases the shear stress seen at the rod wall. The shear stress at the wall is known to largely correlate with the HTC.

Due to the dependence of HTC upon wall shear stress and therefore its dependence on the prediction of secondary flows and the anisotropic turbulent field two experimental datasets were chosen as appropriate validation cases.

*5.2.1 Rectangular Duct Flow of Melling et al [**57**]*

The experiments of Melling et al [**57**] studied near fully developed, isothermal flow in one quadrant of a duct of rectangular cross section. Initial measurements of the entire duct confirmed the symmetry that allowed this simplification. The three mean velocity components and five of the six Reynolds stresses were measured and the mean velocity and turbulent field were examined through contour plots.

5.2.1.1 Boundary Conditions

The boundary conditions of the experimental case are shown in Table 5-4 and the geometry of the test section in Figure 5-8.

Table 5-4: Boundary conditions of the Melling et al [57] validation case

Pressure (MPa)	*0.1013*
Mass Flow Rate (kg/s)	*1.5*
Bulk Velocity (m/s)	*0.915*
Hydraulic Diameter (mm)	*40.49*
***Re* (based on D_h and U_b)**	*42000*

Measurements were taken at two planes; *5.6*D_h and *36.8*D_h. Melling et al showed that the flow at the measuring plane of *36.8*D_h could be considered fully developed. The contour plots produced at this measuring plane will be compared to computations.

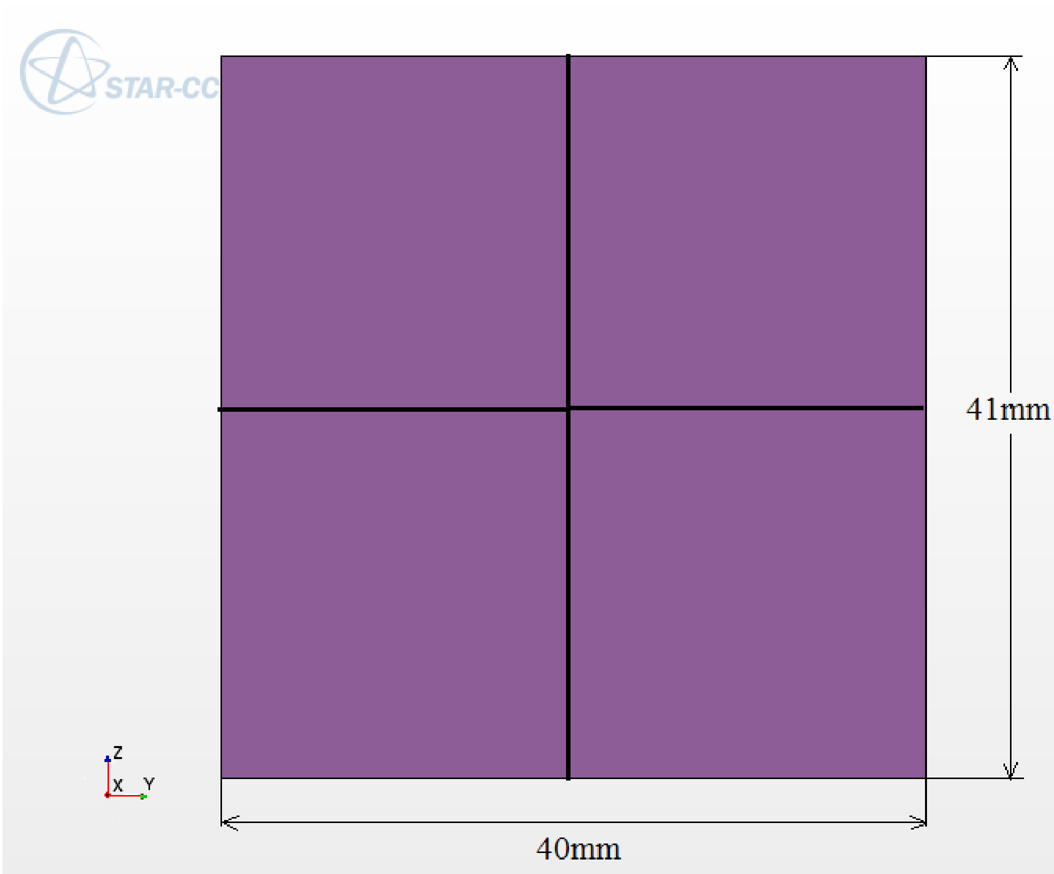

Figure 5-8: Cross section of the rectangular duct of Melling et al [57**]**

5.2.1.2 Computational Parameters

As done in the experiment, only one quadrant of the rectangular duct was modelled by applying symmetry boundary conditions, this is shown in Figure 5-9.

Modelling only one quadrant of the duct limits the size of the flow structures. This partial geometry was able to be exploited due to the knowledge that the secondary flow structures appear as opposing pairs in each corner of the duct and each quadrant of the duct was shown to be identical. The fully developed nature of the flow allowed the application of a fully developed boundary condition connecting the inlet and outlet of the section. The sensitivity to this boundary condition was examined to verify this approach.

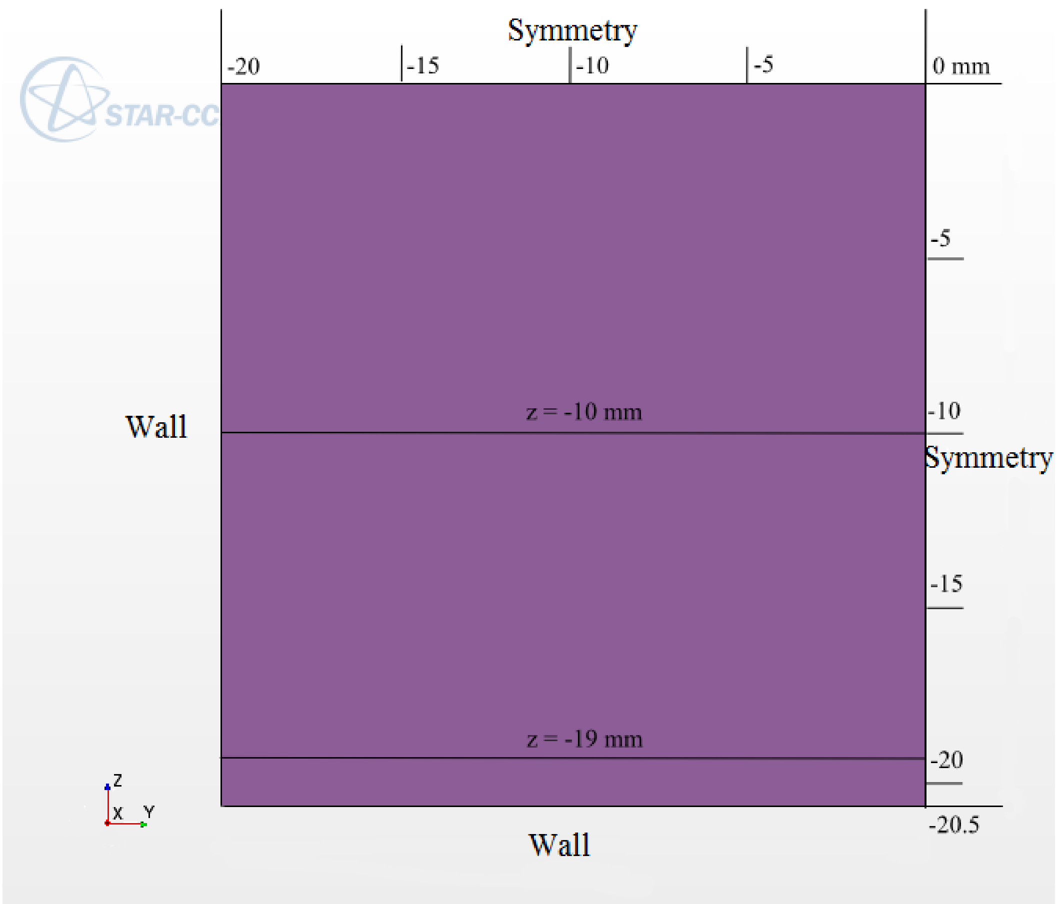

Figure 5-9: One quadrant of the rectangular duct of Melling et al [57]

To achieve a verified solution two computational parameters were varied; (i) the distance from the wall that the first node is to be placed (*y+*) and (ii) the cell size in the bulk of the flow. These are shown in Table 5-5.

Table 5-5: Mesh parameters studied for rectangular duct flow

y+	*<1.1, <2.0, <4.5*
Mesh size in bulk flow (mm)	*0.125, 0.25, 0.5*

5.2.1.3 <u>Mesh Sensitivity Studies</u>

The mesh sensitivity studies using the RSM are shown in this section as the secondary flows and turbulent field were deemed important in monitoring mesh convergence. However, the SST model's prediction of the primary velocity field is included in the validation results.

The results given in Figure 5-10 and Figure 5-11 do not show sensitivity to bulk flow cell size below a cell size of *0.5* mm. To better visualize the flow pattern in the quadrant a sample secondary flow pattern is shown in Figure 5-12.

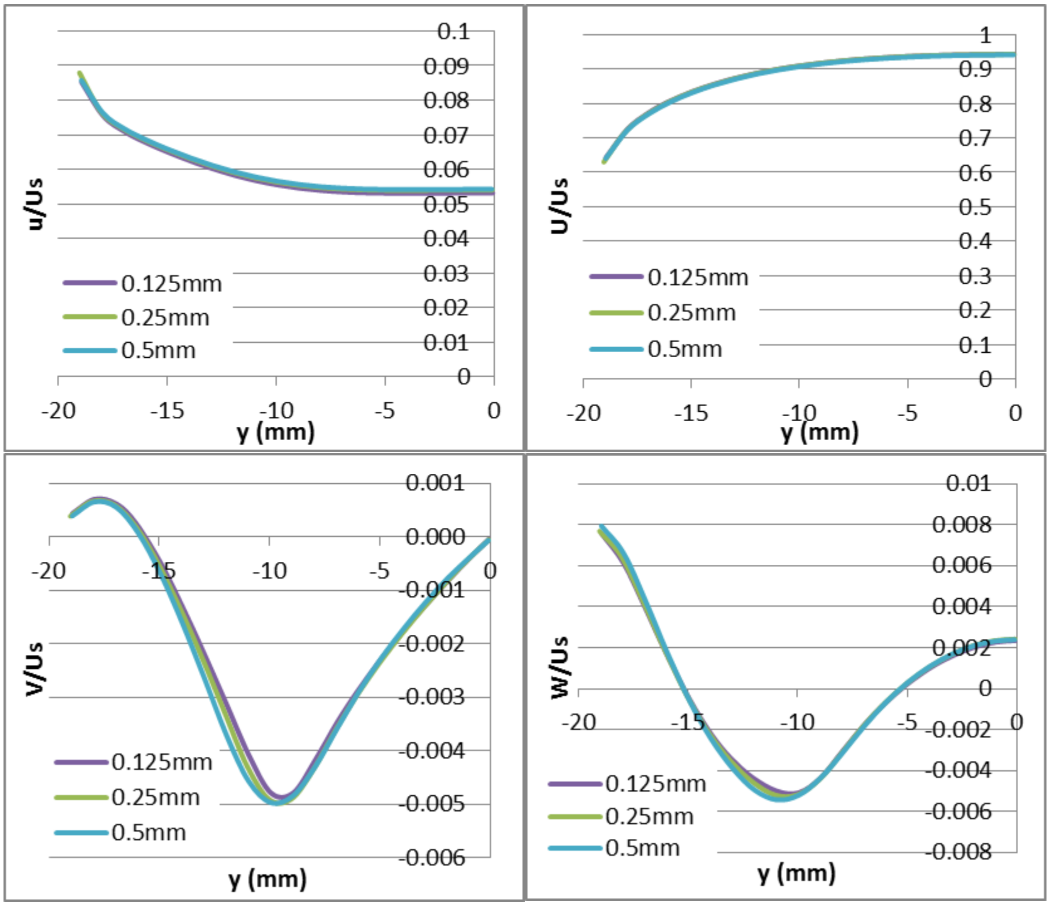

Figure 5-10: Mean and turbulent velocity at z = -10 mm for various bulk flow cell sizes with *y+ < 2*

Any discrepancy seen in Figure 5-10 and Figure 5-11 are the result of extracting variables from a discrete grid and therefore the variables are not defined at the same position. Nonetheless it is seen that the results are not sensitive to bulk flow cell size.

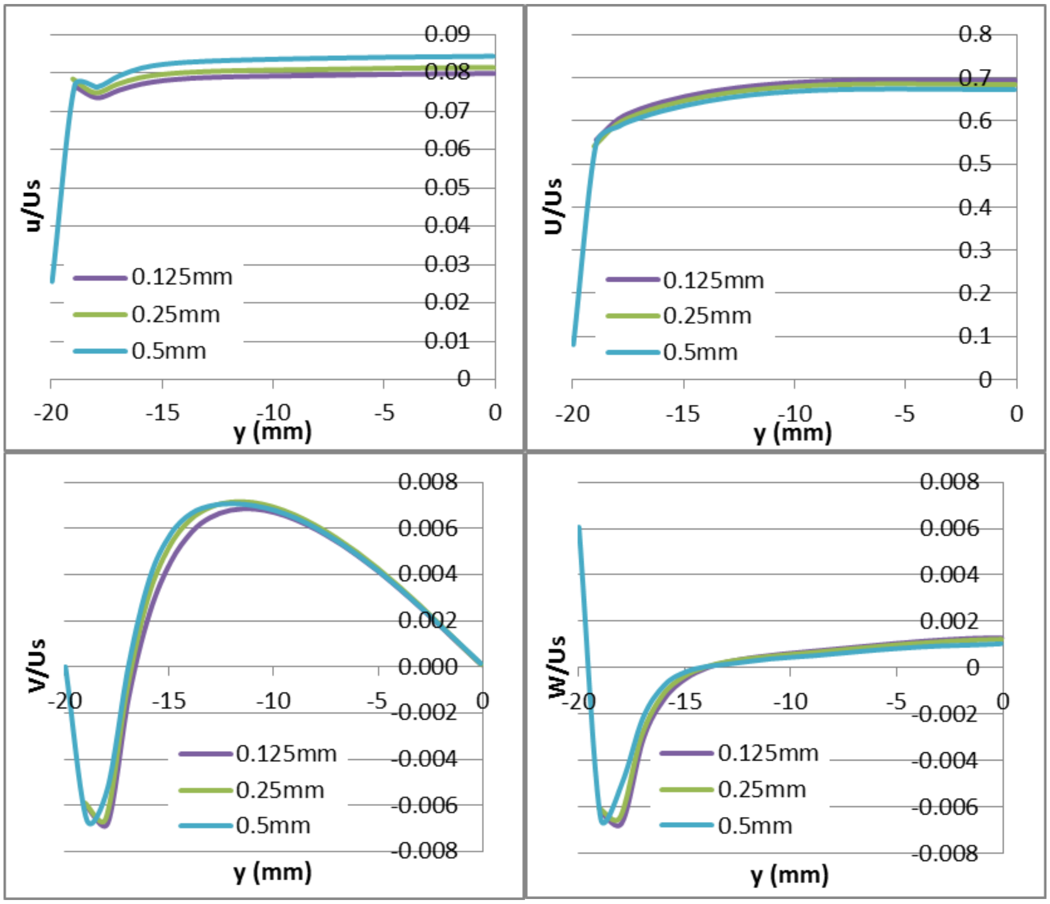

Figure 5-11: Mean and turbulent velocity at z = -19 mm for various bulk flow cell sizes with *y+ < 2*

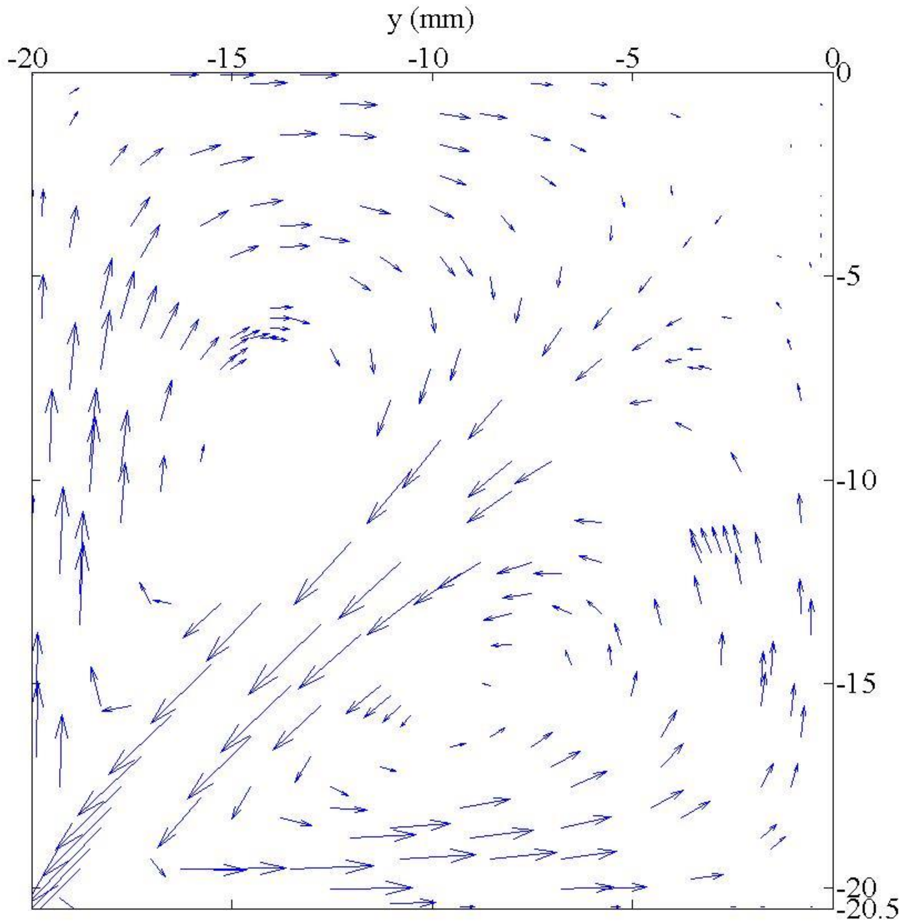

Figure 5-12: Secondary flow pattern in one quadrant of a rectangular duct

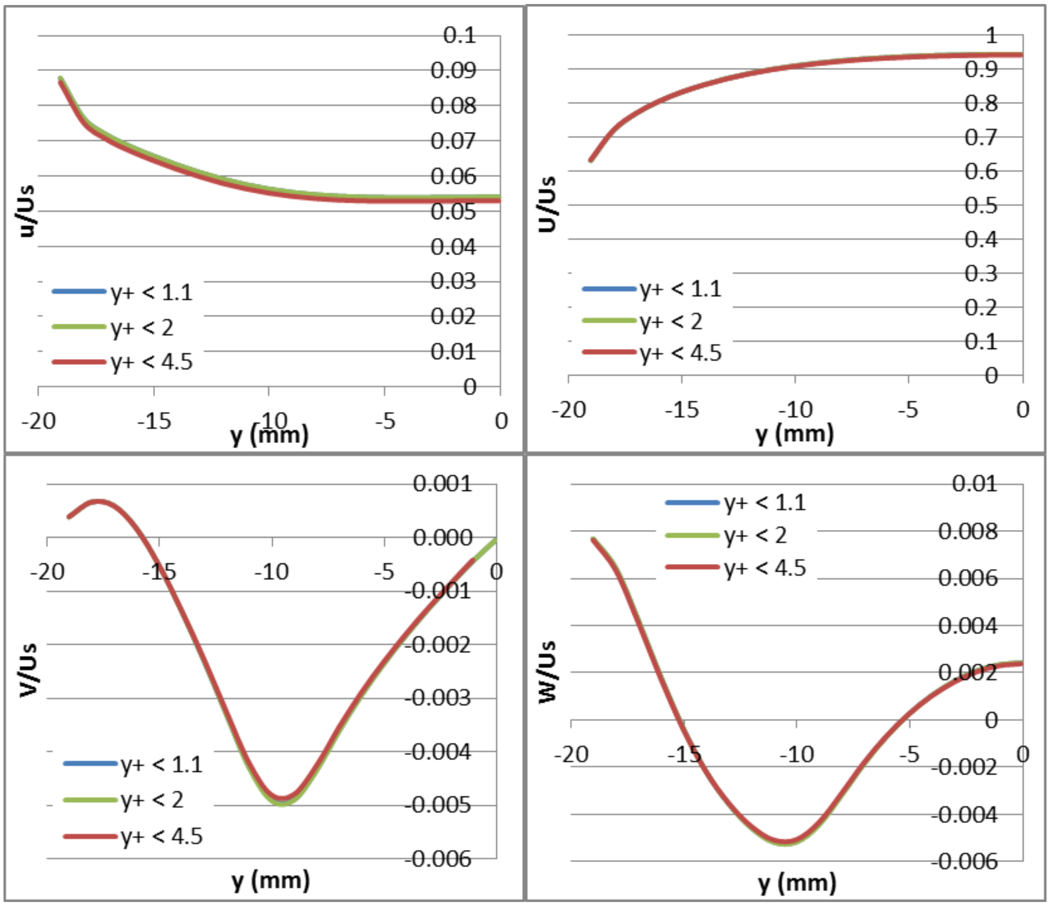

Figure 5-13: Mean and turbulent velocity at z = -10 mm for various values of *y+* with bulk flow cell size = 0.25 mm

The results given in Figure 5-13 and Figure 5-14 are shown not to be sensitive to *y+*.

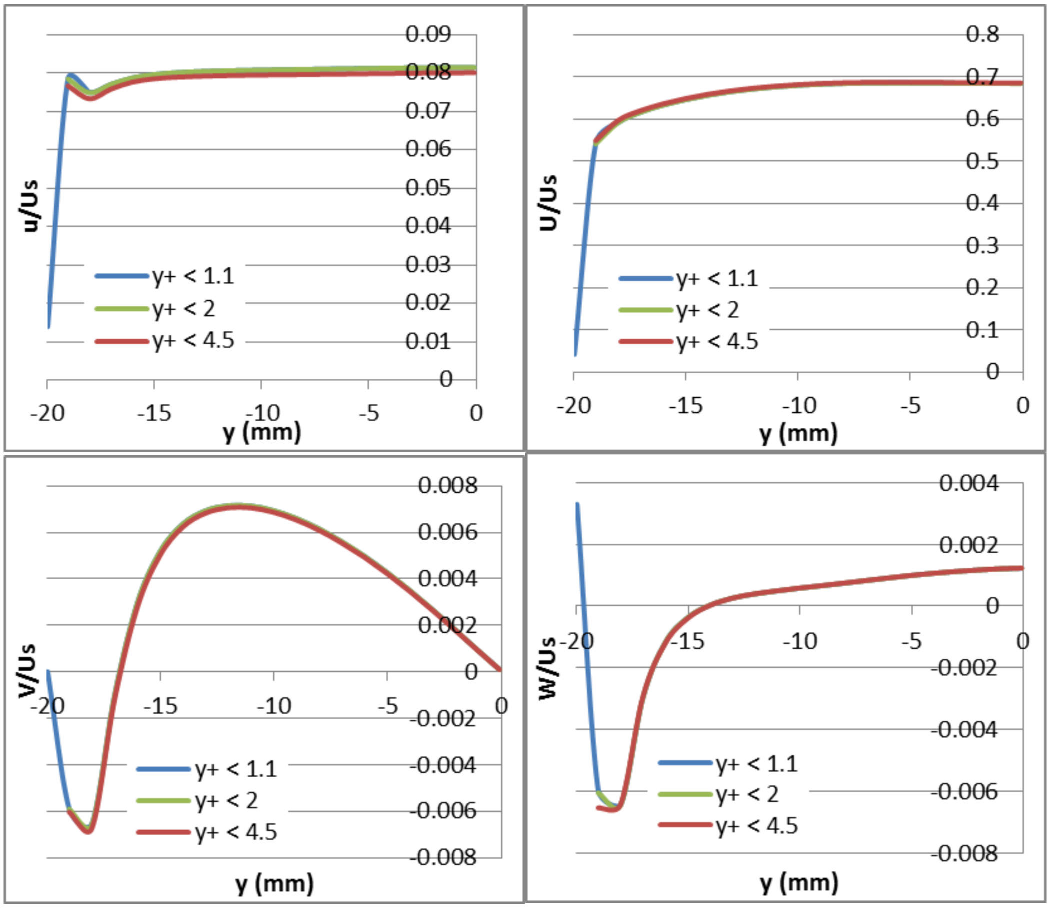

Figure 5-14: Mean and turbulent velocity at z = -19 mm for various values of *y+* with bulk flow cell size = 0.25 mm

Therefore, the mesh used for the validation study will have a bulk flow cell size of *0.5* mm, *y+ < 4.5* and take advantage of the fully developed boundary condition applied between the inlet and outlet.

5.2.1.4 Validation Study

The results of the mesh sensitivity studies show that the RSM predicts appreciable secondary flows on the order of 1% of the primary flow. As discussed previously in Chapter 2.2, the presence of the secondary flows results in the distortion of the isovels towards the corners of the duct. The primary isovels of RSM are compared to the isovels produced by Melling et al [**57**] in Figure 5-15. The isovels produced using the experimental results are much more distorted than those predicted by the RSM. This is due to the under prediction of the secondary flows; which act to convect momentum from the bulk flow into the corners.

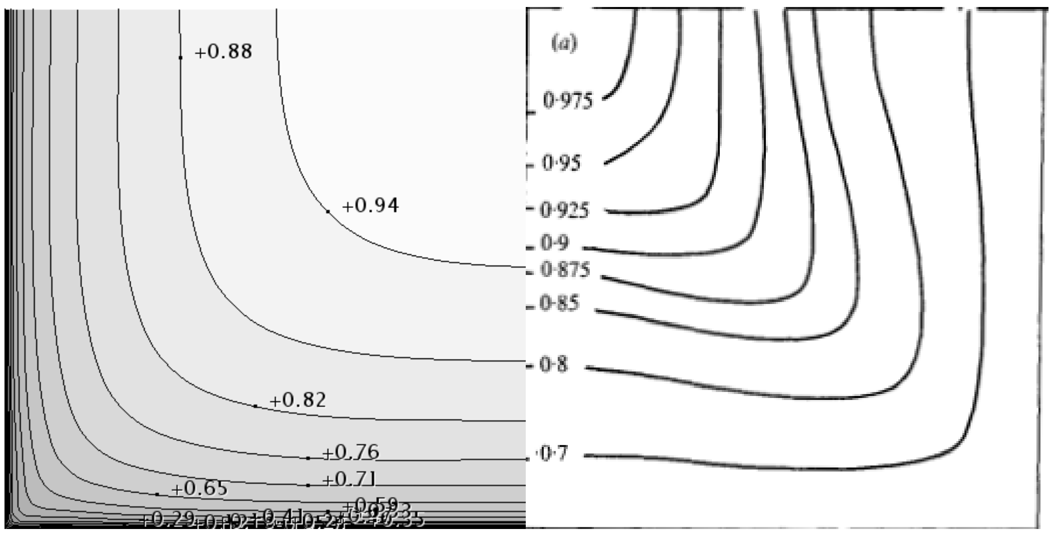

Figure 5-15: U/U_s isovels in one quadrant of a rectangular duct for RSM (left) and Melling et al [57**] (right)**

The distortion of the isovels for the primary turbulent velocity – seen in Figure 5-16 - is even more prevalent and this distortion is also under-predicted by the RSM due to the same reason stated above.

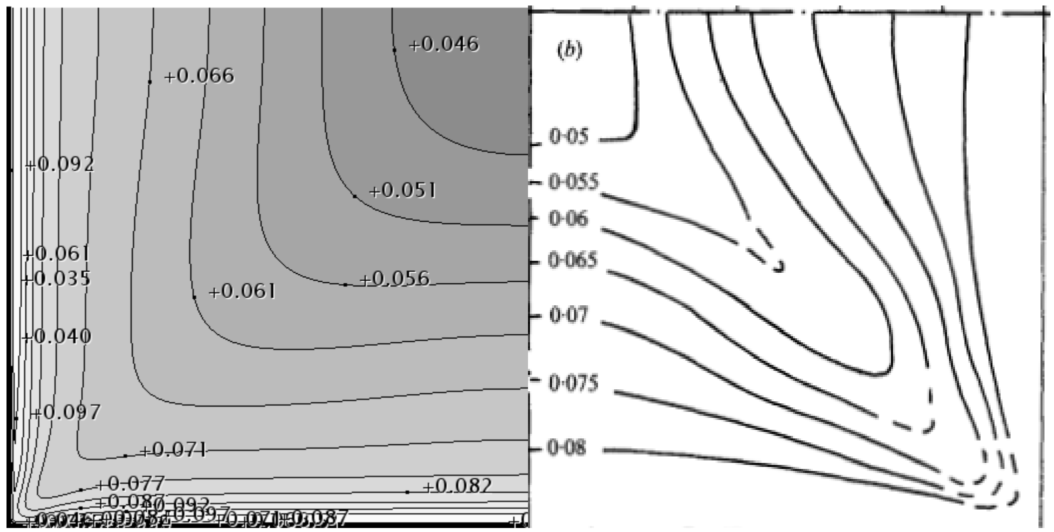

Figure 5-16: u/U$_s$ isovels in one quadrant of a rectangular duct for RSM (left) and Melling et al [57] (right)

The calculated distribution of the z component of the secondary flow is shown to agree quite well with the experimental results as shown in Figure 5-17. However, the magnitude is under-predicted by a factor of 2-3.

Figure 5-18 shows a comparison of the primary velocity isovels predicted by the RSM and SST turbulence model. The rounded isovels of the SST prediction are due to the model’s inability to predict the secondary flows and thus there is no appreciable convection of momentum into the corners of the duct. The lack of secondary flows also causes the wall shear stress distribution to be increasingly non-uniform. This becomes an important consideration when the heat transfer is considered as wall shear stress will dictate the HTC and a non-uniform wall shear stress distribution will result in wall temperature non-uniformities.

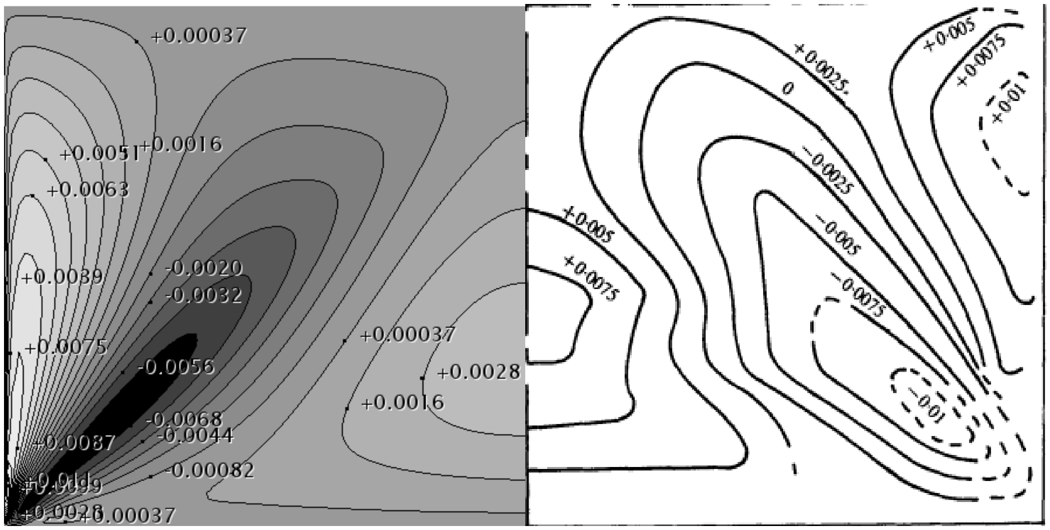

Figure 5-17: W/U$_s$ isovels in one quadrant of a rectangular duct for RSM (left) and Melling et al [57] (right)

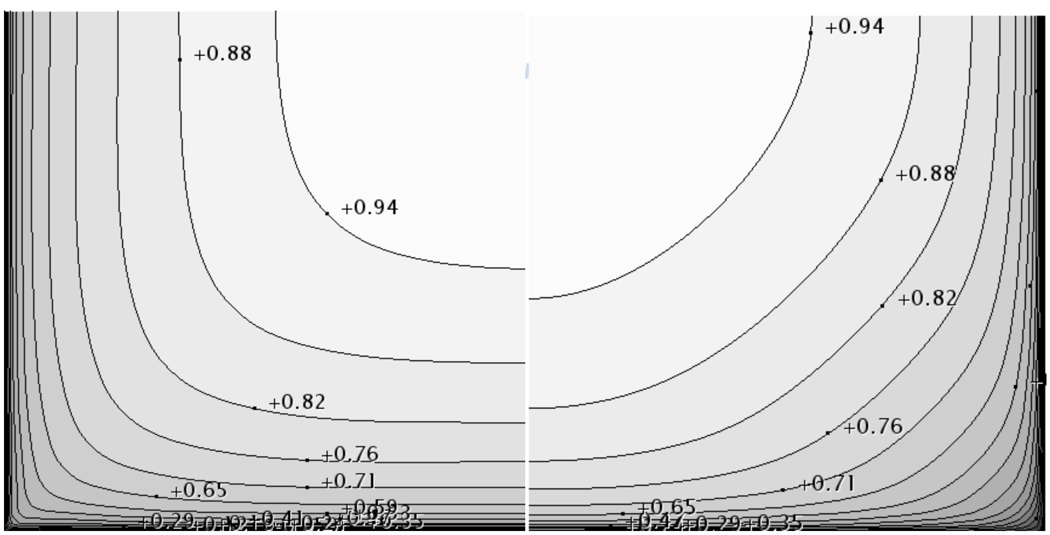

Figure 5-18: U/U$_s$ isovels in one quadrant of a rectangular duct for RSM (left) and SST (right)

The RSM was shown to predict moderate distortion of the primary isovels and was able to predict the distribution of the secondary flows. Despite its under-prediction of the secondary flows by a factor of 2-3, the RSM outperformed the SST model simply because the linear Boussinesq approximation relating the Reynolds stress tensor to the velocity gradient tensor does not allow for the precise prediction of the Reynolds stress field that drives the secondary flows.

5.2.2 "Infinite" Rod Bundle Flow

The experiments of Trupp et al [**53**] were examined in a simulated infinite rod bundle with square and triangular lattice configurations and various pitch to diameter ratios. In the case of the triangular lattice, measurements of mean velocity, five of six Reynolds stresses and local wall shear stress were made for one sixth of a subchannel.

5.2.2.1 Boundary Conditions

The boundary conditions of the experimental case C6 are shown in Table 5-6.

Table 5-6: Boundary conditions of the Trupp et al [53**] validation case**

Bulk Velocity (m/s)	*12.78*
Hydraulic Diameter (mm)	*29.86*
***Re* (based on U_b and D_h)**	*23760*

The experimental geometry studied was that of a triangular lattice rod bundle shown in Figure 5-19. Two sub channels are shown in the figure and due to symmetry; each sub channel can be split into six equivalent sections.

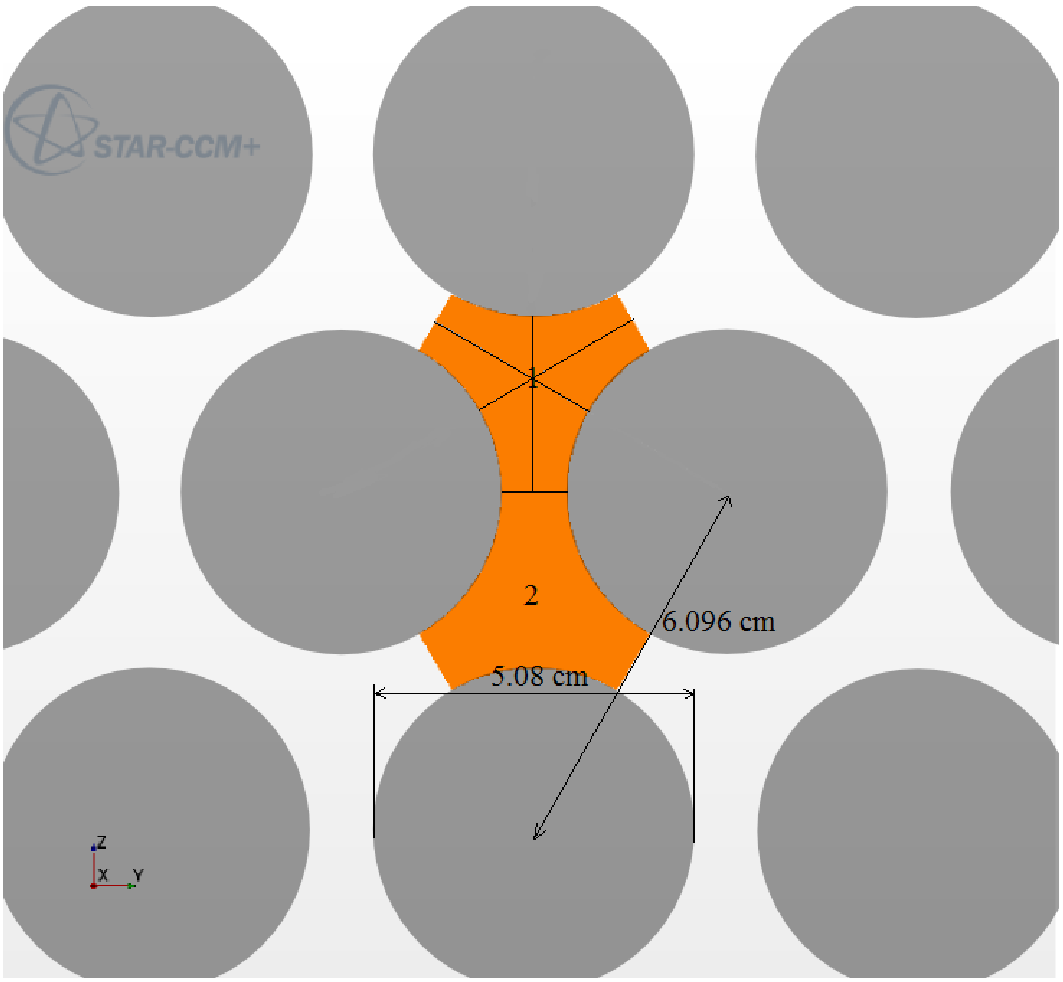

Figure 5-19: Triangular lattice rod bundle with P/D = 1.2

5.2.2.2 Computational Parameters

Computations were performed for a one-sixth sub channel as well as two sub channels using symmetry and rotationally periodic boundary conditions, respectively. A fully developed boundary condition was applied across the inlet and outlet of all simulations to reduce computation time.

To achieve a verified solution two parameters were varied; (i) the distance from the wall that the first node is to be placed (*y*+) and (ii) the cell size in the bulk of the flow. These parameters are described in Table 5-7.

Table 5-7: Mesh parameters studied for rod bundle flow

***y*+**	*<0.3, <0.7, <4.0*
Mesh size in bulk flow (mm)	*0.36, 0.72, 1.44*

5.2.2.3 <u>Mesh Sensitivity Study</u>

As in the Melling et al study, the mesh sensitivity studies were done using the RSM and are shown in this section. This is due to the very poor performance of the SST model in predicting the secondary flows. However, the SST prediction of the turbulent velocities in the three coordinate directions and the average friction velocity are included in the study. The mesh sensitivity study with the SST model has been performed and can be found in Appendix B.

The turbulent velocity results within the one sixth sub channel were used to identify mesh independence. Figure 5-20 identifies the measuring regions within the sub channel. Trupp et al measured the turbulent velocities along the *0°*, *15°*

and *30°* lines and therefore the mesh sensitivity will be determined by doing the same. In order to generate the plots the distance from the rod wall, *y*, is normalized by the variable *y'* which is the distance from the rod wall to the bisector of the sub channel and therefore varies azimuthally.

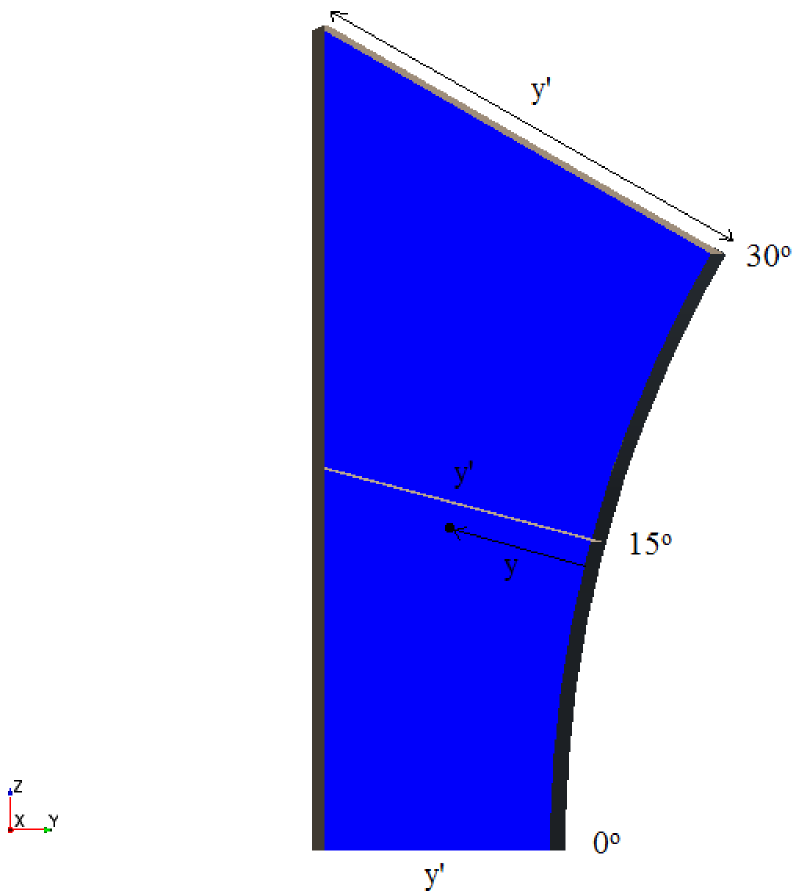

Figure 5-20: Measuring axes within the one sixth sub channel

The turbulent velocity along the *0°* and *30°* degree lines are reported in Figure 5-21 and it shows that for a $y+ < 0.7$ the results are not sensitive, as the blue line of $y+ < 0.3$ is completely covered by the green line of $y+ < 0.7$.

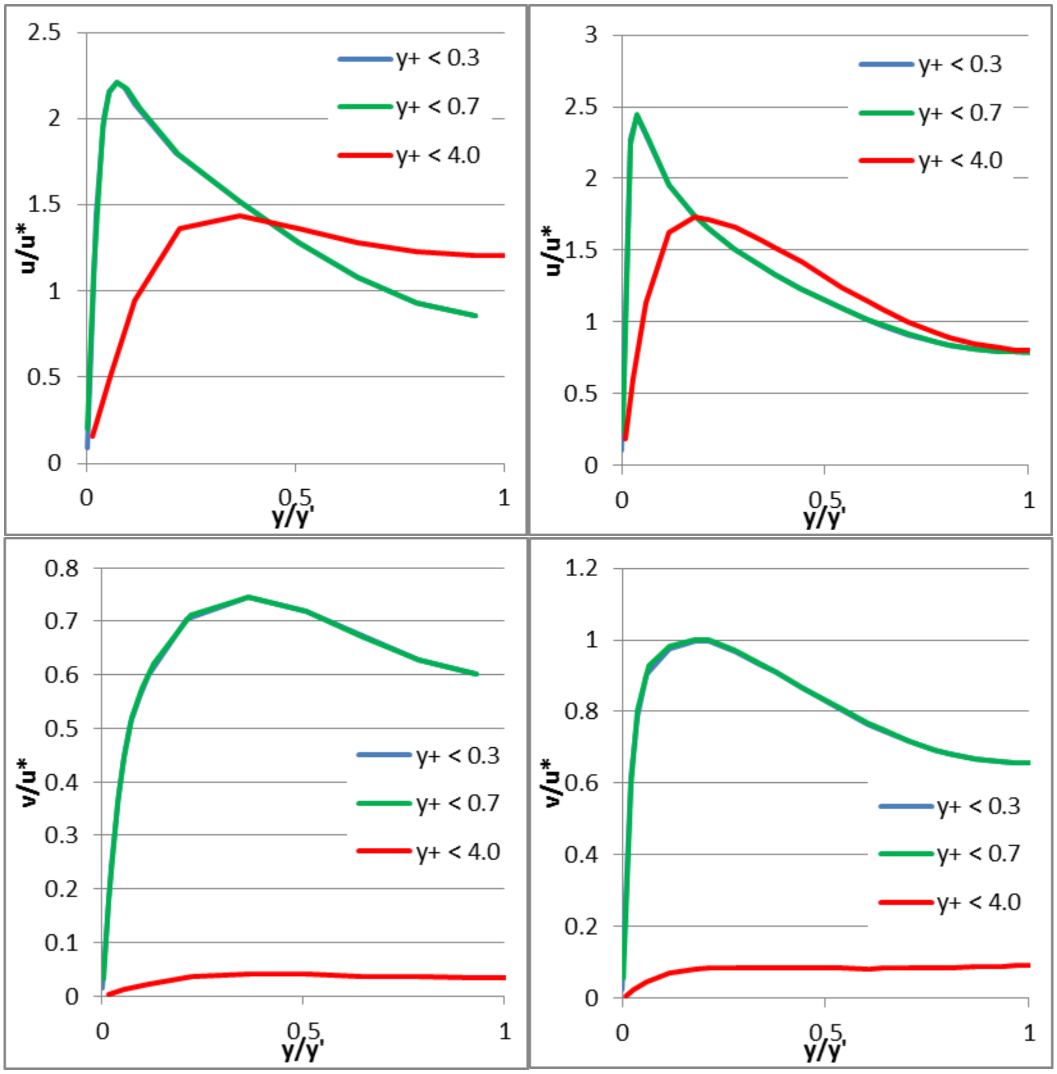

Figure 5-21: Turbulent velocity along the *0°* (left) and *30°* (right) lines for various values of *y+* with bulk flow cell size = 0.72 mm

Turbulent velocity results given by meshes of various bulk flow cell sizes are shown in Figure 5-22. The results show no sensitivity to bulk flow cell size.

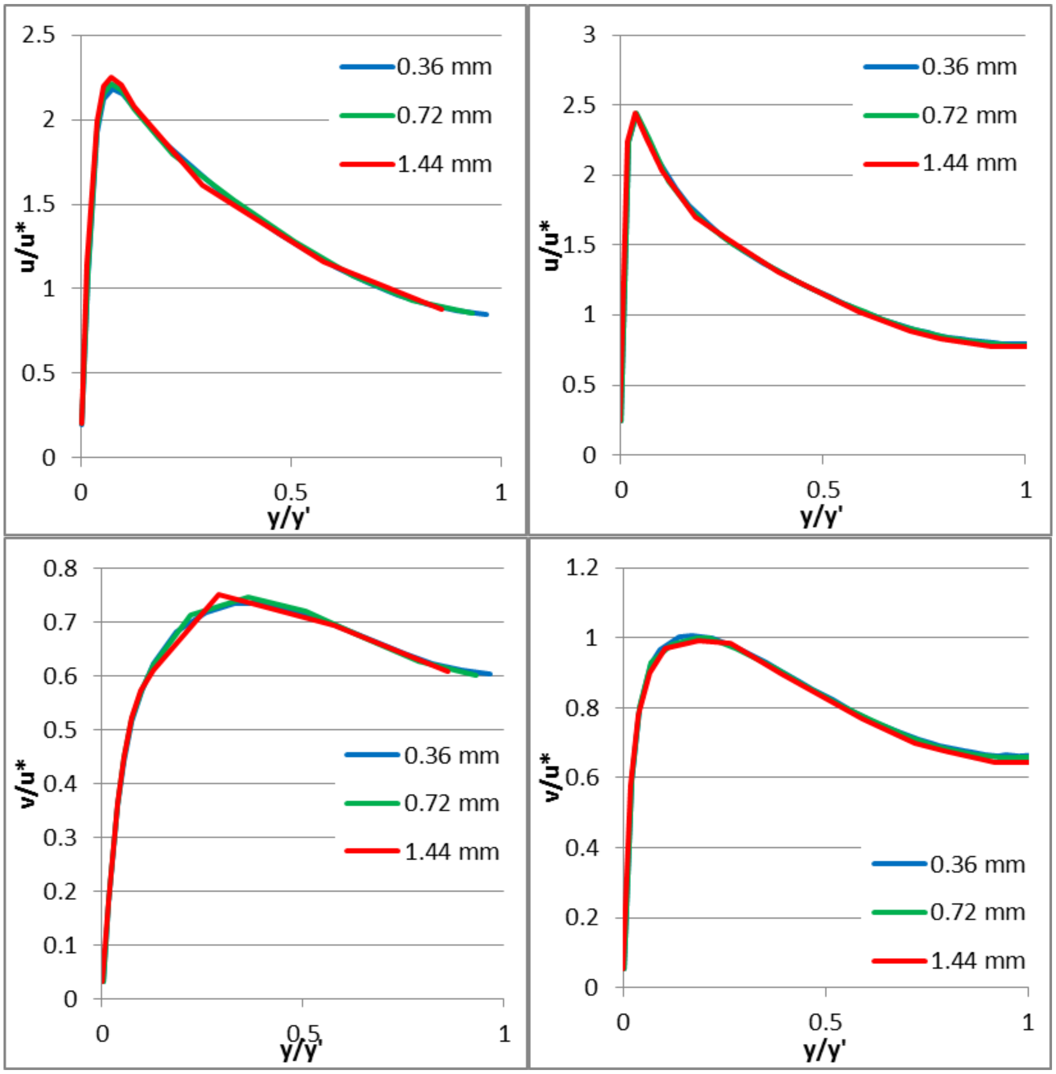

Figure 5-22: Turbulent velocity along the *0°* (left) and *30°* (right) lines for various values of bulk flow cell size with *y+ < 0.7*

Therefore, the mesh used for the validation study will have a bulk flow cell size of *1.44 mm* and *y+ < 0.7*.

5.2.2.4 Validation Study

The performance of each turbulence model used for this study is judged by its ability to predict the turbulent velocity field as well as the average friction velocity. These two flow characteristics are known to be related as the turbulence present in the flow increases the momentum transfer throughout the flow and therefore has an impact on the shear stress at the wall. Therefore, as stated previously, the average friction velocity – which relates to the wall shear stress – is the primary predictor in determining the successful model.

Table 5-8: Comparison of average friction velocity for the SST, RSM and Trupp et al [53**]**

Model	**u* (m/s)**
Trupp et al [**53**]	*0.781*
SST	*0.720*
RSM	*0.740*

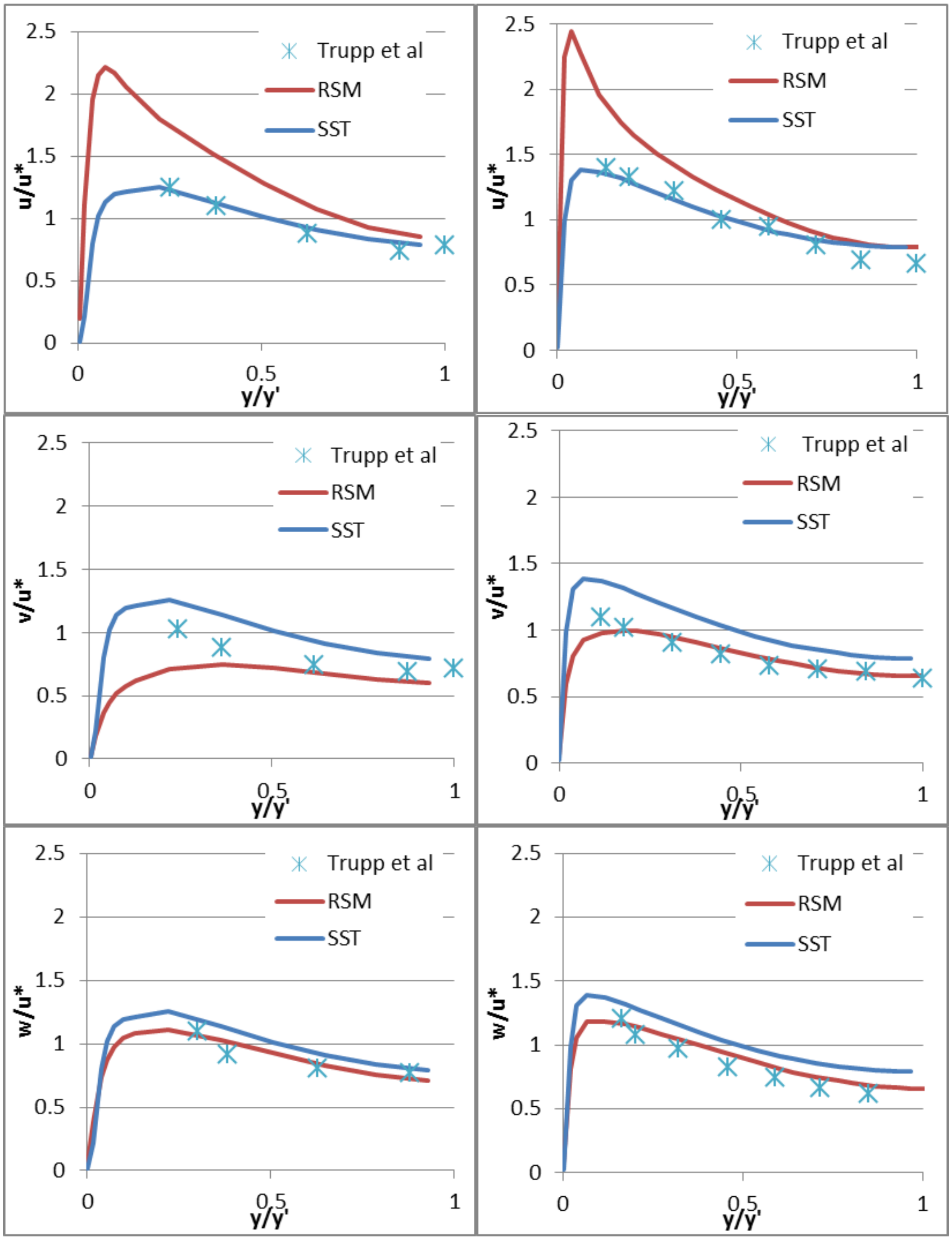

Figure 5-23: Comparison of turbulent velocity along the *0°* (left) and *30°* (right) lines for RSM, SST and Trupp et al

The average friction velocity results are shown in Table 5-8 while the RSM and SST model are compared to the experimental turbulent velocity measurements in Figure 5-23. The predictions of average friction velocity are pleasantly surprising; the SST model, despite its inability to predict the secondary flows, gives nearly the same prediction as the RSM.

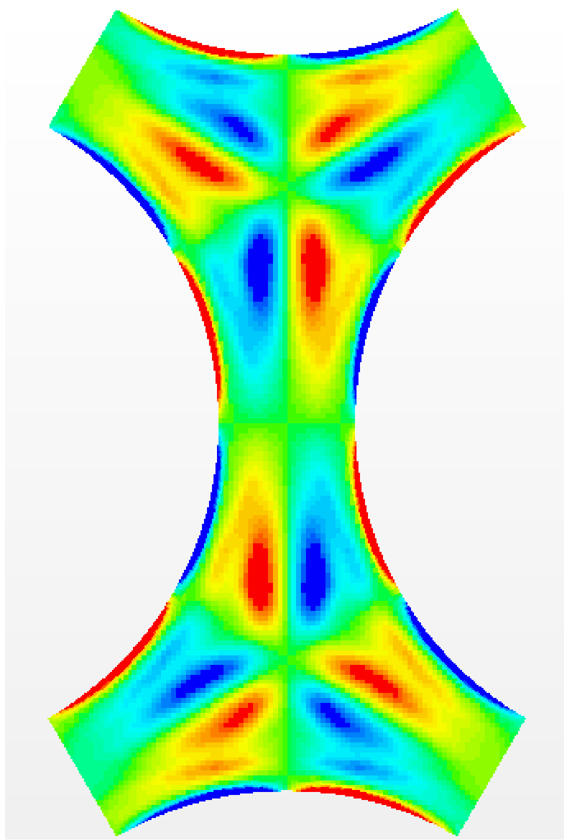

Figure 5-24: The secondary flow cells in the two sub channel geometry of Trupp et al calculated by RSM

The structure of the secondary flows within the rod bundle is shown in Figure 5-24. Regardless of flow direction into or out of the page, the cells in blue are rotating clockwise and the cells in red are rotating counter-clockwise. This is shown to illustrate the similarities between square duct flow and rod bundle flow.

5.3 Turbulence Model Choice

The previous validation studies have given insight into the capability of the RSM and SST turbulence models. The SST model was shown to outperform the RSM in predicting the HTC for NHT and EHT to supercritical water in a tube. The DHT regime was not studied further as Table 5-2 shows that DHT due to thermally induced bulk flow acceleration and buoyancy influence is not expected to occur in the heated cases B1 and B2 of the JAEA. The RSM was shown to outperform SST in terms of predicting the distribution of secondary flows for flows in channels of non-circular cross section. However, the SST model and RSM showed comparable agreement when predicting the turbulent velocities as well as when predicting the average friction velocity for flow in a rod bundle. Along with these key results, advantages and disadvantages of each model are discussed in the following subsection.

It should be noted that the predictions of SST shown in Figure 5-23 are identical regardless of the turbulent velocity direction. This is a reality due to the normal velocity gradients $(\frac{\partial U}{\partial x}, \frac{\partial V}{\partial y}, \frac{\partial W}{\partial z})$ being very close to zero and thus the Boussinesq approximation (Equation 1.11) becomes a function of the turbulent kinetic energy.

The most obvious advantage of the SST model is its computational efficiency compared to the RSM. The SST model solves the conservation equations plus two transport equations of turbulence (k and ω) while the RSM solves the conservation equations plus seven transport equations of turbulence (6 Reynolds stresses and ε).

The SST model also gives improved convergence of residuals and therefore there is more confidence in obtaining repeatable results. In complex geometries the RSM is known to have difficulty reaching a converged solution [**4**]. There exists a long history of numerical difficulties associated with the solution of the ε equation; particularly in the near wall region. This is the reason for the various approaches to the solution of ε mentioned in Chapter 1.4.1.4.

Speziale et al [**63**] mentions the lack of natural boundary conditions as well as the appearance of high order correlations in the near wall formulation of the ε equation contribute to this difficulty. The ε equation at the wall reduces to the balance of the viscous diffusion of ε with the dissipation of ε [**63**]:

$$\nu \frac{\partial^2 \varepsilon}{\partial y^2} = c_{\varepsilon 2} \frac{\varepsilon^2}{k} \tag{5.1}$$

The presence of the second order spatial derivative of the dependent variable necessitates the accurate modelling of the right hand side; which can lead to numerical difficulty [**63**].

A commonly used boundary condition for the ε equation is one prescribed from the exact turbulent kinetic energy equation [**63**]:

$$\nu \frac{\partial^2 k}{\partial y^2} = \varepsilon \tag{5.2}$$

This then relies heavily upon the accuracy of the near wall prediction of k in order to accurately prescribe the boundary condition. Other authors have employed more numerically convenient boundary conditions for ε that are not physically satisfying [**63**].

To avoid this trouble, the two layer approach is used which simply prescribes the value of ε based on the solution of the k equation and a length scale parameter which is a function of wall distance and a turbulent Reynolds number. The weakness of this approach is its heavy reliance on the logarithmic velocity distribution [**64**]. Also the blending of the one equation model near wall with the two equation model in the bulk flow is done at some arbitrary turbulent Reynolds number.

In considering the increased number of transport equations and the numerical difficulty associated with the RSM, computations on the same computational grid require 2-5 times the computational resources as compared to the SST model.

The SST model, however, utilizes the $k - \omega$ formulation [**8**] near wall which does not make use of damping functions and also allows the application of simple boundary conditions which leads to robust numerical behaviour [**34**]. Further, the $k - \omega$ formulation has been shown to outperform the $k - \varepsilon$ model in the viscous sublayer, giving more accurate predictions of skin friction and equally accurate mean velocity profiles [**34**]. As the wall distance is increased, the $k - \omega$ model is blended with the $k - \varepsilon$ model such that the well-known sensitivity of the $k - \omega$ model to free-stream values of ω is avoided. Therefore, the SST model combines the best features of the $k - \omega$ and $k - \varepsilon$ models to give a numerically robust approach that relies on the accuracy of $k - \omega$ in the near wall region and the accuracy of $k - \varepsilon$ in free shear layers.

The flows of the JAEA experimental geometry are very much wall bounded flows as the *P/D* ratio is quite low and the resolution of the boundary layers on the heated rods is of utmost importance in predicting the HTC. In addition to this, the presence of the grid spacer geometry acts to introduce localized heat transfer enhancement due to the production of turbulent kinetic energy in its near wall region due to the high levels of strain that will be present as the bulk fluid flowing in the centre of the sub-channel suddenly encounters walls. In light of the preceding arguments, the SST model has been chosen as the turbulence model with which to simulate the experiments of the JAEA.

Chapter 6

Sensitivity Studies

Prior to reporting the final results for each of the three experimental cases decisions must be made regarding the spatial discretization. The sensitivity of pressure drop and wall temperature results to spatial discretization parameters will be thoroughly investigated in the following sections.

The monitoring criteria for the following sensitivity studies will be pressure drop for the isothermal case A1 and wall temperature for the heated cases B1 and B2 as these are the predictions to be submitted to the GIF SCWR computational benchmark exercise.

For both the isothermal case A1 as well as the heated cases B1 and B2 the one-third rod bundle geometry seen in Figure 4-11 was used as it was determined that the pressure drop and wall temperature results were identical when compared to those of the full rod bundle geometry.

6.1 Isothermal Case A1 Sensitivity

The basis of analyzing the mesh sensitivity for this case will be the pressure drop calculated across one grid spacer. Each simulation case had boundary conditions consistent with Figure 4-13 (a). The pressure drop was measured between two probes that were placed 5 mm and 125 mm, upstream and downstream of the grid spacer, respectively.

The mesh sensitivity results are summarized in Table 6-1. Where base size refers to the cell size used to discretize the bulk flow and different parameters were used to discretize the rod and grid spacer/shroud walls.

Owing to the fact that very little sensitivity is seen in the results of pressure drop, the mesh giving the smallest amount of cell volumes is chosen to be applied to the full length test section. Case **B** is therefore chosen and a cross section of the mesh within the grid spacer is shown in Figure 6-1 and a detailed view of the near wall discretization is shown in Figure 6-2. The discretization in the axial direction proved to be of little consequence and a symmetric hyperbolic tangent function has been used both upstream and downstream of the grid spacer.

Table 6-1: Mesh sensitivity results for case A1

Case	**Base Size (mm)**	**Rod *y+***	**Grid Spacer/Shroud *y+***	**Pressure Drop (kPa)**
A	*0.1*	*<0.53*	*<1.08*	*11.805*
B	*0.2*	*<0.53*	*<1.08*	*11.913*
C	*0.2*	*<0.09*	*<1.08*	*12.034*
D	*0.2*	*<0.02*	*<1.08*	*12.063*
E	*0.2*	*<0.09*	*<4.65*	*11.597*
F	*0.2*	*<0.09*	*<0.56*	*12.220*

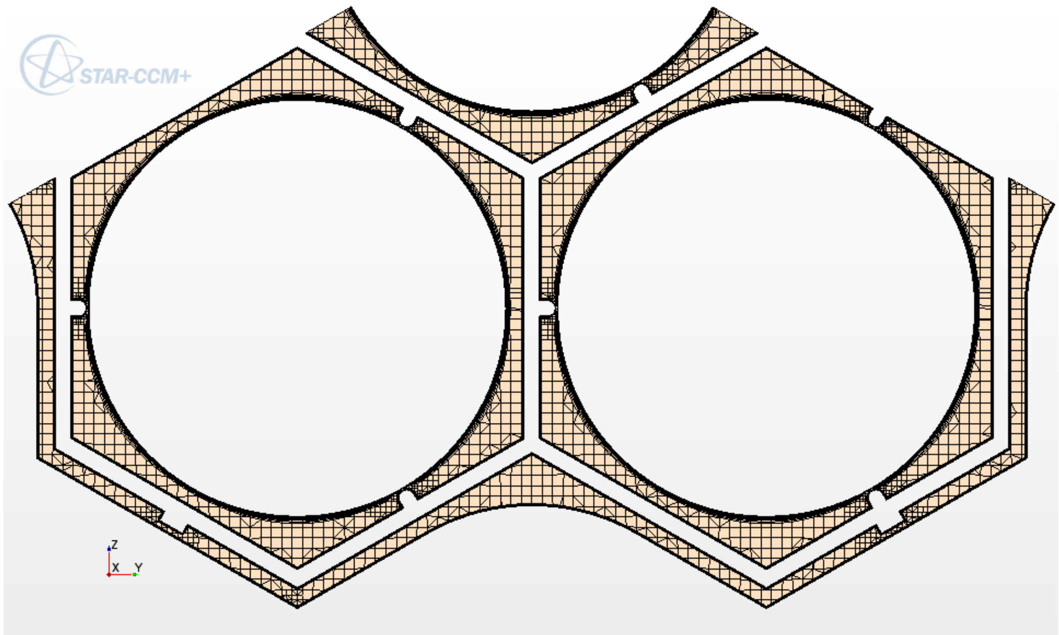

Figure 6-1: Spatial discretization to be used for the isothermal case A1

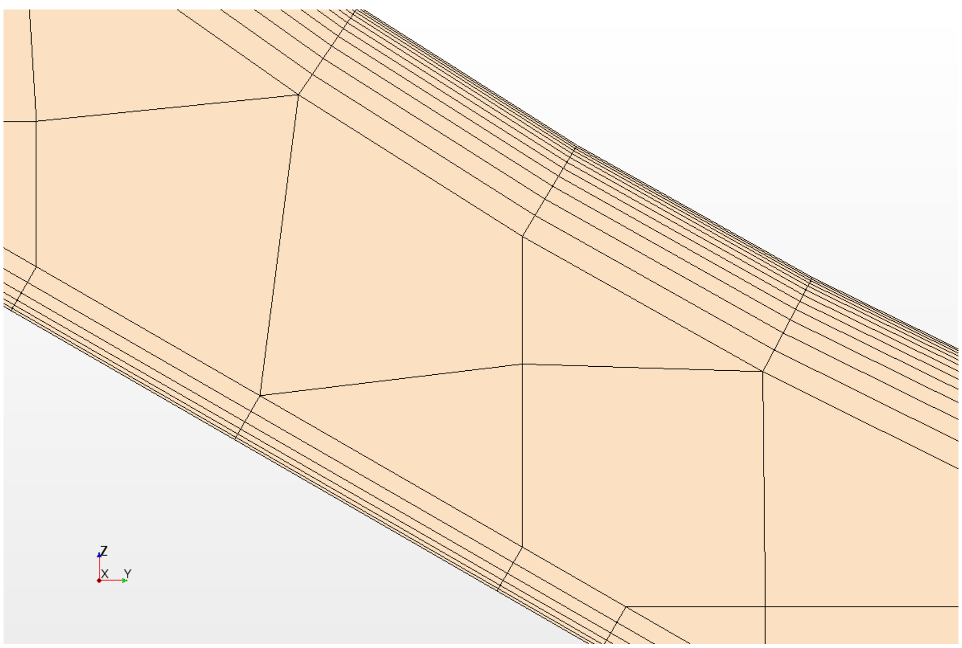

Figure 6-2: Detailed view of the near wall discretization to be used for the isothermal case A1

6.2 Heated Case B1 and B2 Sensitivity

The basis of the mesh sensitivity of these cases will be the calculated centre rod wall temperatures at a definite azimuthal position along a certain axial length. As explained in Chapter 4.2.1, the 4th spacer shown in Figure 4-7 will act as the geometry in which these sensitivities are examined. The azimuthal position on the centre rod will be defined as in Figure 4-11.

The boundary conditions of the high enthalpy, high heat flux case B2 will be used to report the results of the mesh sensitivity study. It can be easily reasoned that if mesh independence is achieved for case B2, applying the same mesh to the low enthalpy, low heat flux case B1 will result in mesh independence as well. In fact, this check has been made and for the sake of brevity the sensitivity results for case B1 are not included.

Figure 6-3 shows that the use of a base size of *0.4mm* results in increased prediction of wall temperature. This is expected due to the coarse grid acting to spatially average the velocity and temperature field and ultimately show an effect similar to an increased viscosity (numerical viscosity). Further, there is little difference in wall temperature between the simulations using *0.1mm* and *0.2mm* base size. For the sake of computational efficiency a base size of *0.2mm* was chosen.

All the cases used hexahedral computational cells to discretize the coolant and clad domain. The clad domain is discretized using *0.2mm* computational cells.

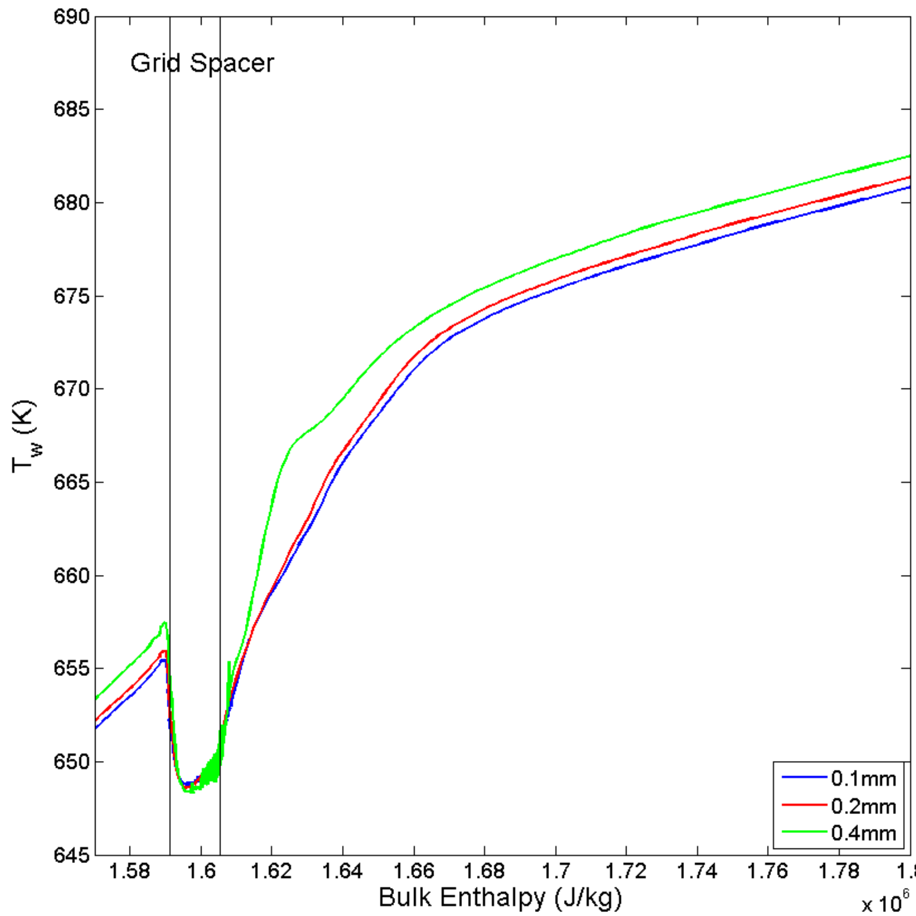

Figure 6-3: T_w vs. Bulk Enthalpy of the 4th grid spacer section along the *270°* azimuthal position of the centre rod for various base sizes

Figure 6-4 shows that the wall temperature predictions change, if only slightly, as the near rod wall mesh is refined to a very low *y+*. This is expected due to the very large property gradients that exist where even a small temperature gradient exists when the temperature is close to $T_{pc} = 658\ K$. The near rod wall mesh was chosen to be refined to *y+<0.09*, this is due to the diminishing return in terms of the increased number of iterations required for convergence as a result of meshing even finer.

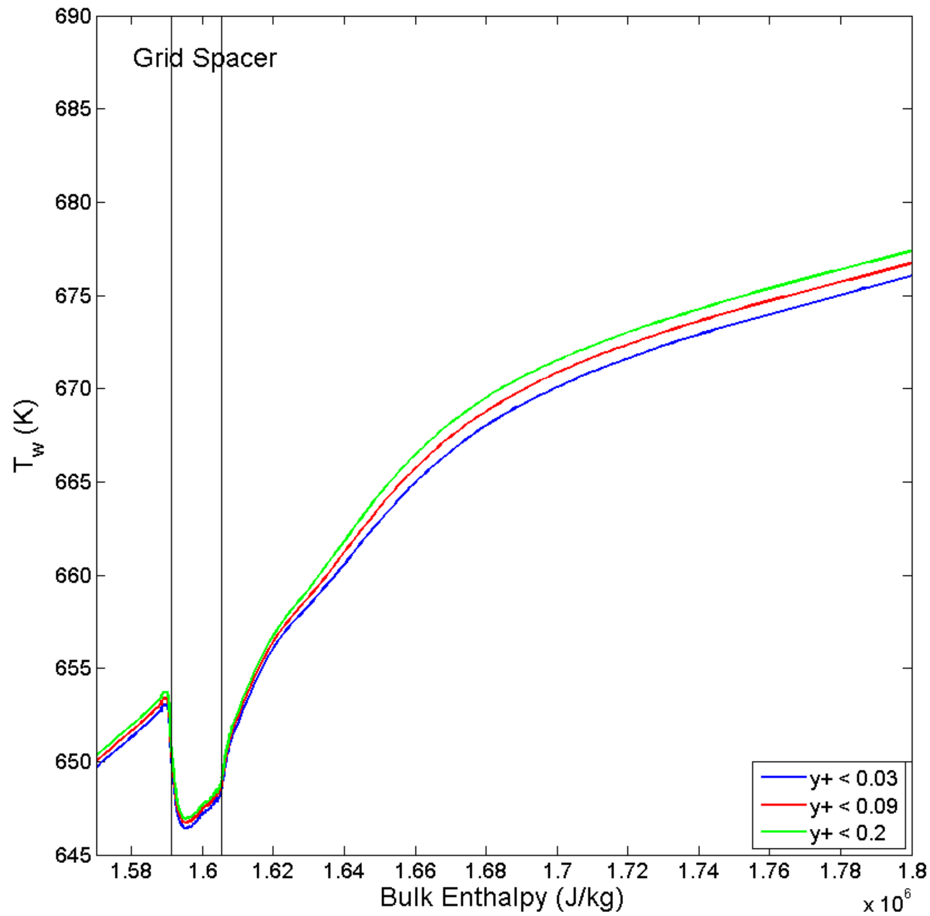

Figure 6-4: T_w vs. Bulk Enthalpy of the 4th grid spacer section along the *270°* azimuthal position of the centre rod for various rod *y+* values

Figure 6-5 shows the effect of modifying the radial growth rate (RGR) of computational cells as they are placed away from the rod wall. For the same reason of diminishing return as stated above, an RGR = *1.28* was chosen.

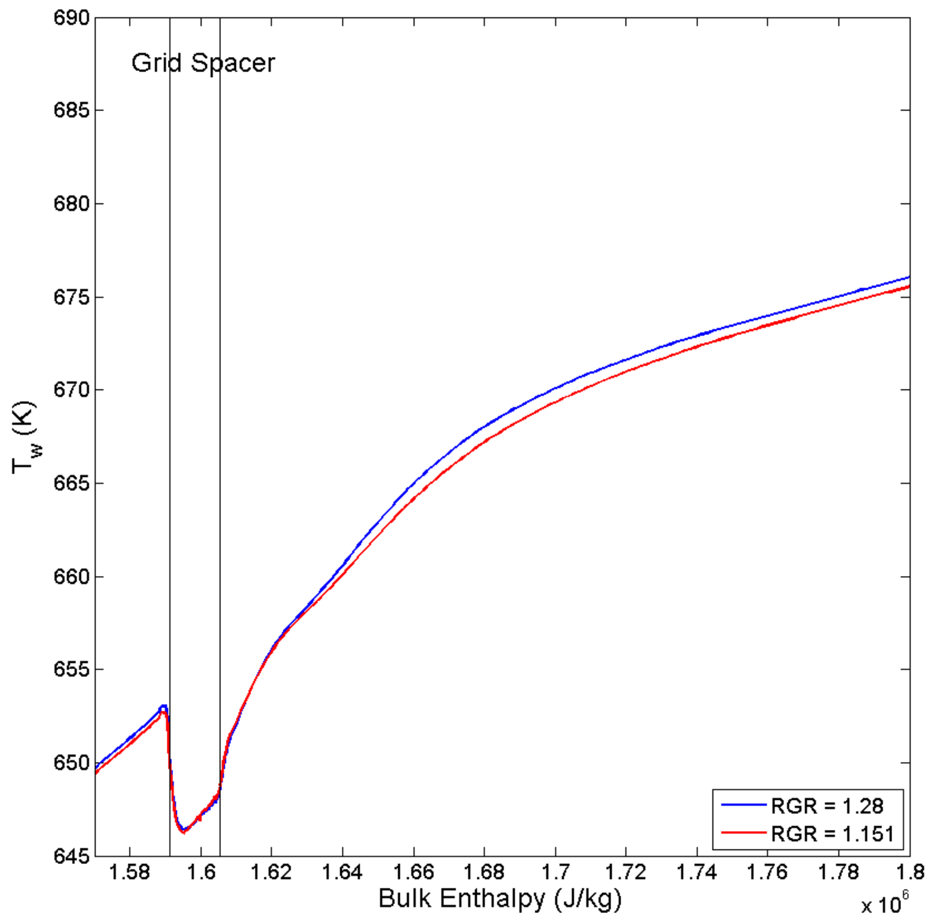

Figure 6-5: T_w vs. Bulk Enthalpy of the 4th grid spacer section along the *270°* azimuthal position of the centre rod for various rod RGR values

Figure 6-6 shows the effect of refining the shroud and grid spacer near wall mesh. The main consideration when refining the mesh on these walls was the proper prediction of the turbulent kinetic energy. When the first computational cell was placed in the range of $5<y+<16$, the turbulent kinetic energy was predicted much higher than if the laminar sub-layer was resolved, as it is in the other cases. The increase in turbulent kinetic energy increases the turbulent heat flux and enhances heat transfer from the heated surface. The shroud and grid spacer near wall mesh was chosen to be refined to $0.3<y+<2.5$ due to its ability to resolve the laminar sub-layer and avoid difficulty of placing the first computational cell within the buffer layer.

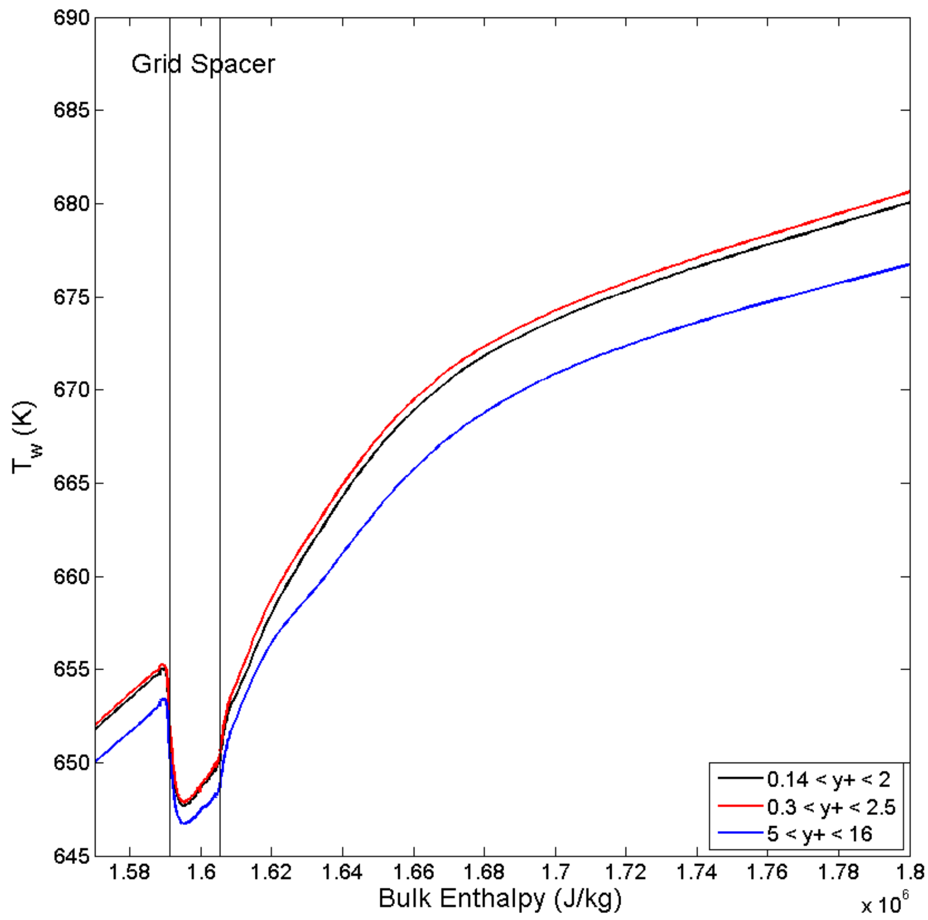

Figure 6-6: T_w vs. Bulk Enthalpy of the 4th grid spacer section along the *270°* azimuthal position of the centre rod for various grid spacer/shroud *y+* values

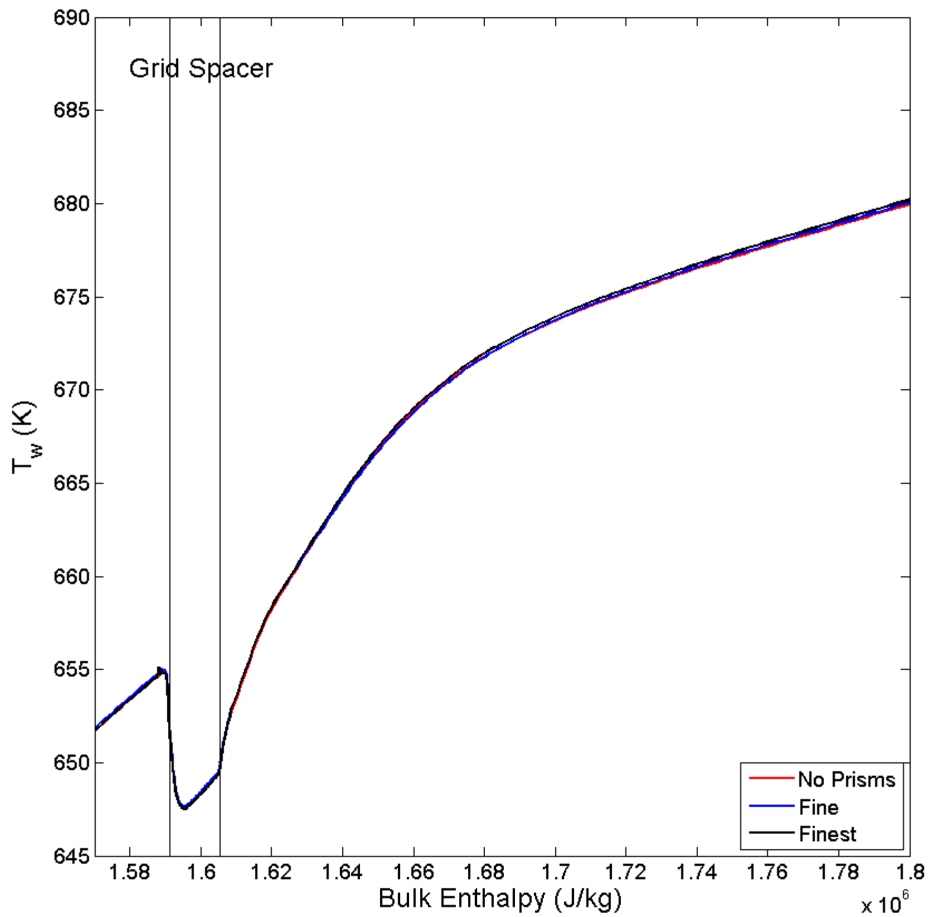

Figure 6-7: T_w vs. Bulk Enthalpy of the 4th grid spacer section along the *270°* azimuthal position of the centre rod for various clad mesh refinement

Figure 6-7 shows that no effect is present when refining the heat flux and clad interface boundary. The “No Prisms” series represents no specific treatment of the heat flux and clad interface boundary (Figure 4-11), the clad is simply discretized entirely by aligned hexahedral computational cells. The “Fine” series represents an order of magnitude refinement at the heat flux and clad interface boundary (*0.02mm)* and the “Finest” series represents another order of magnitude refinement (*0.002mm)*. Due to the slight improvement of convergence with the refinement of the heat flux and clad interface boundaries, the "Fine" series was chosen.

As stated previously in Chapter 6.1, the discretization in the axial direction proved to be of little consequence and a symmetric hyperbolic tangent function that achieves a ratio of largest to smallest cell of 40 has been used both upstream and downstream of the grid spacer.

The mesh parameters for the heated cases are summarized below in Table 6-2.

Table 6-2: Mesh parameters used for the heated cases B1 and B2

Base Size	*0.2mm*
Rod *y+*	*<0.09*
Rod RGR	*1.28*
Grid Spacer/Shroud *y+*	*0.3<y+<2.5*
Clad Interface/Heat Flux Boundary Refinement	*0.02mm*
Axial Discretization	Symmetric Hyperbolic Tangent

A typical cross section of the clad mesh is shown in Figure 6-8. A cross section of the coolant mesh within the grid spacer is shown in Figure 6-9 and a detailed view of the near wall discretization is shown in Figure 6-10.

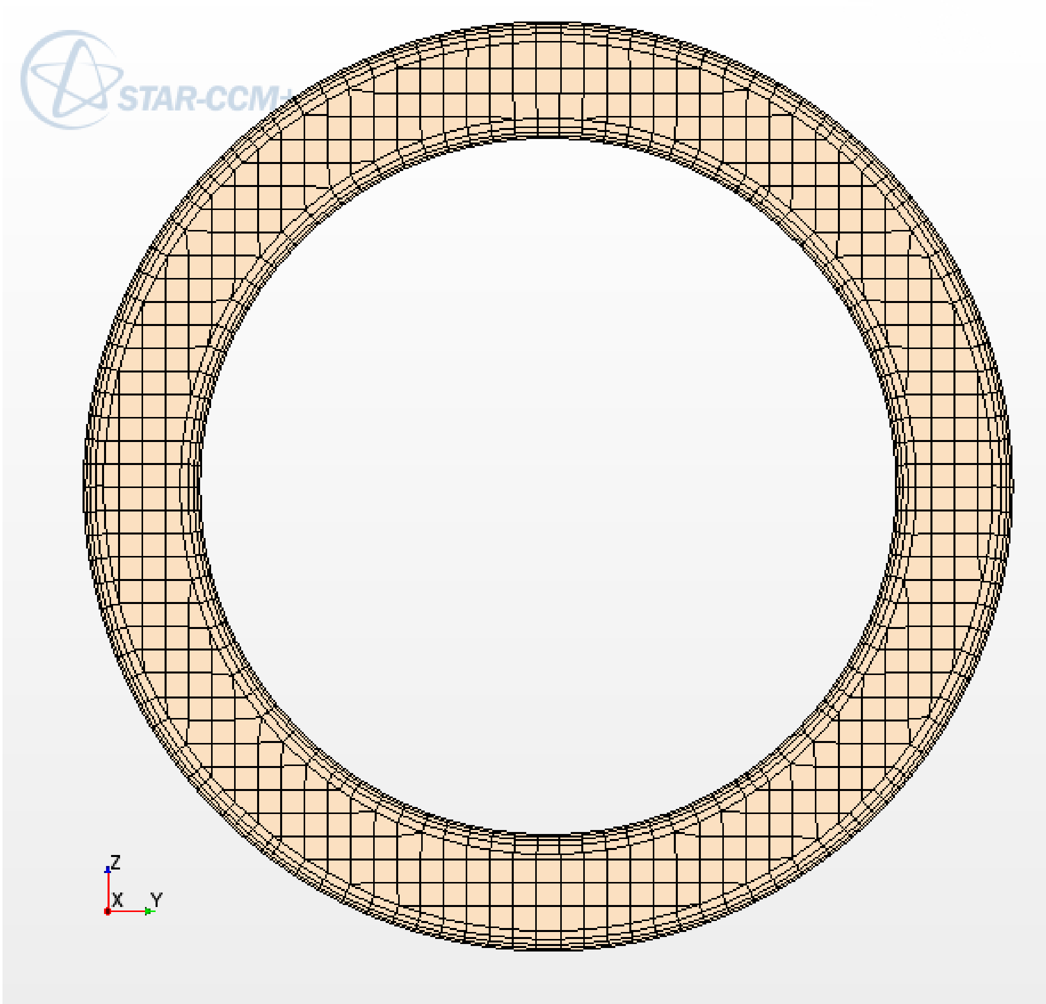

Figure 6-8: Spatial discretization of the clad to be used for the heated cases B1 and B2

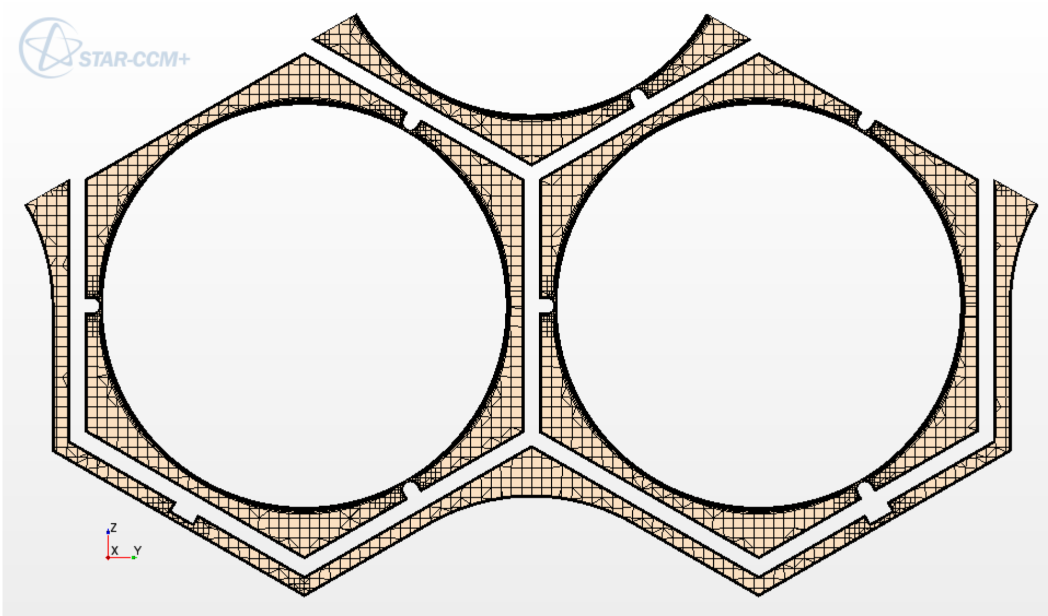

Figure 6-9: Spatial discretization of the coolant to be used for the heated cases B1 and B2

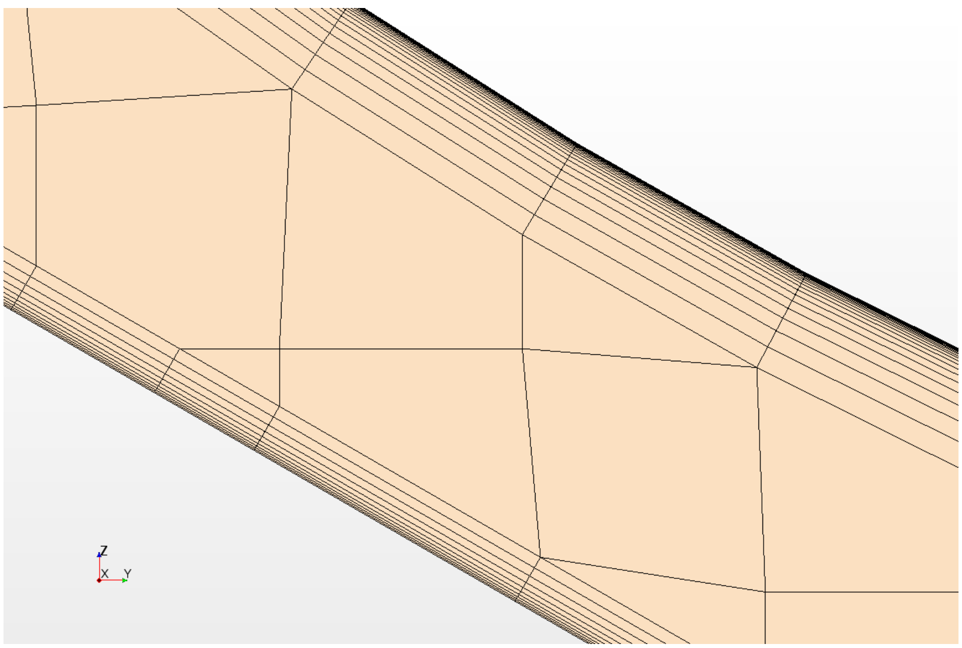

Figure 6-10: Detailed view of the near wall discretization to be used for the heated cases B1 and B2

Chapter 7

Final Results

The final simulation results for each of the three experimental cases can now be presented. Prior to this, practical considerations regarding simulation set-up, including mesh size and computational resources, will be discussed. The results of velocity, turbulence kinetic energy and pressure drop will be shown for the isothermal case. Following this, the results of velocity, turbulent kinetic energy and rod wall temperatures will be shown for the heated cases. Throughout, the discussion will focus upon the physics predicted by the turbulence model, trusting that the results presented here represent the model's "true" predictions with minimal discretization error. An effort will be made to critique the turbulence model choice in terms of the expected experimental results. The known weaknesses of the EVMs will be illuminated in this process. This chapter will rely heavily on the visualization through contour plots and the raw temperature and pressure drop data submitted to the GIF SCWR computational benchmark exercise can be found in Appendix C.

7.1 Simulation Set-Up

For each of the three experimental cases, the test section was split into five sections, with each section containing one grid spacer. A plane upstream of the outlet of the previous section served as the inlet to the next section. Parameters were taken upstream of the outlet in order to prevent any impact of the pressure boundary condition. The inlets of the successive sections were defined by the velocity vector, temperature, turbulent kinetic energy, *k,* and specific dissipation rate, ω at each cell on the inlet plane.

Table 7-1: The computational properties of the simulation cases

Case	**Computational Resources**	**Total Mesh Size (Millions of cells)**	**CPU Time (hrs)**
Isothermal A1	8 CPU, 2.27 GHz	Coolant: 17.46	120
Heated B1	64 CPU,	Clad: 6.69 Coolant: 46.99	2450
Heated B2	30 CPU, 1.95 GHz	Clad: 6.06 Coolant: 30.51	1516

Splitting the test section into five sections reduced the individual simulation file size greatly which allowed for easy file transfer and quicker trouble-shooting should a simulation give unexpected or erroneous results. The computational properties of each simulation case are shown in Table 7-1.

7.2 Isothermal Case A1

7.2.1 Pressure Drop

Referring to Figure 4-7, which is presented again for convenience, the pressure tap positions along the test section can be seen. The pressure drop measured across these two positions has been calculated to be *61.77%* due to the minor losses associated with the four grid spacers and the remainder of the pressure drop is due to the major losses.

Table 7-2: Pressure Drops

Structure	Pressure Drop (kPa)
Grid Spacer (5mm up and downstream)	*8.301*
Between Pressure Taps	*53.749*

Each grid spacer was found to contribute an identical pressure drop. This is due to the predicted flow returning to an equivalent fully-developed state upstream of each grid spacer. The pressure drop for each grid spacer as well as the total pressure drop is shown in Table 7-2

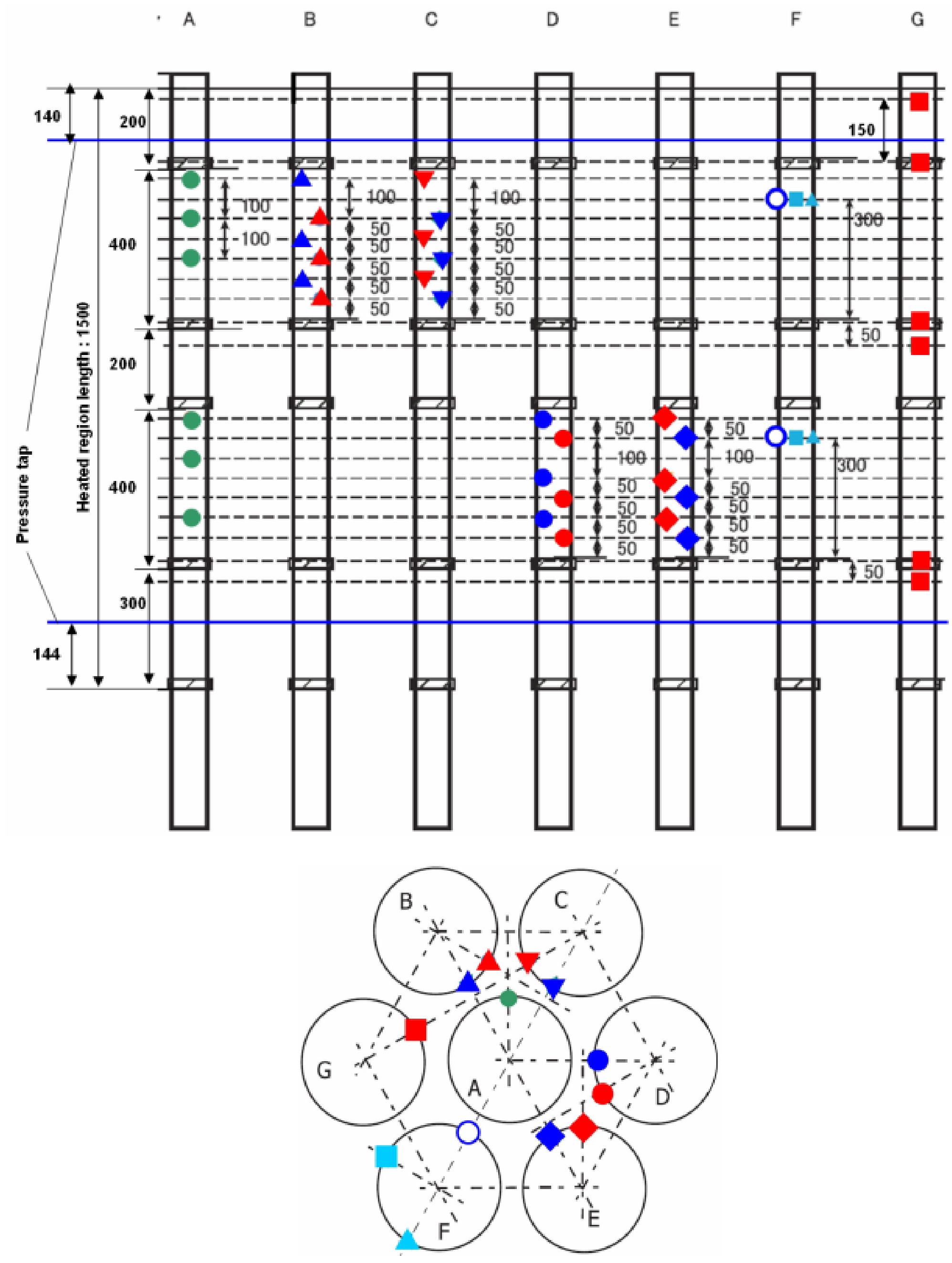

Figure 4-7: Pressure tap and thermocouple positions for final submission [61]

7.2.2 Flow Field Through and Downstream of the Grid Spacer

The velocity and turbulent field of the isothermal case will be analyzed in order to gain insight into the effect that the grid spacer has on the flow. This knowledge will then be used to analyze the heated cases' results of wall temperature.

Due to the equivalent nature of the flow through each of the grid spacers, only one of the grid spacers will be studied. For convenience a local coordinate system (shown in Figure 7-1) with its origin at the downstream edge of the spacer will be used to report the contour plots of velocity and turbulent kinetic energy.

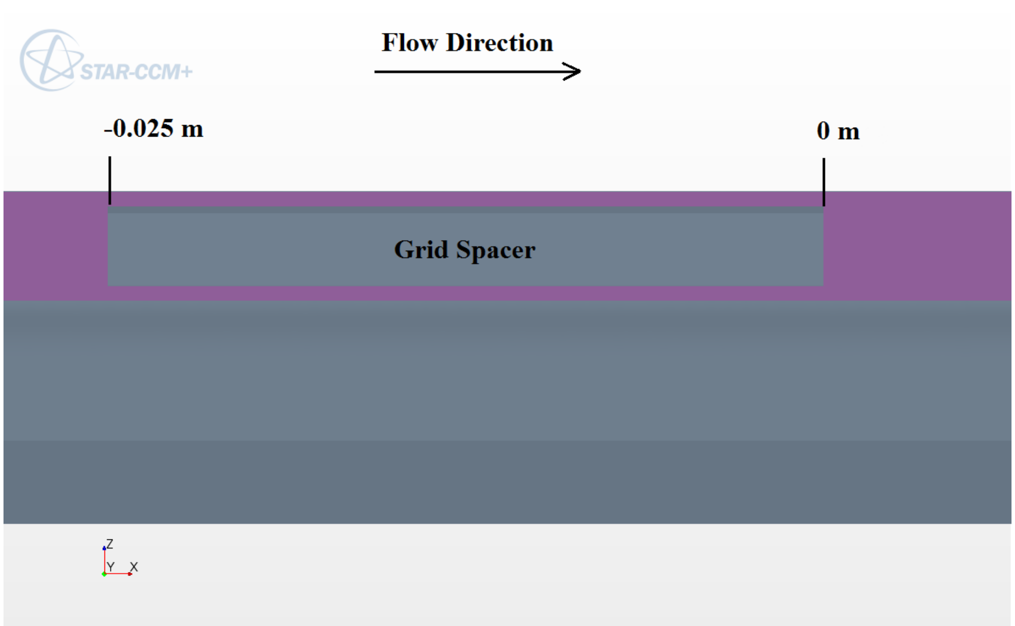

Figure 7-1: Local coordinate system defining positions relative to the downstream edge of the grid spacer

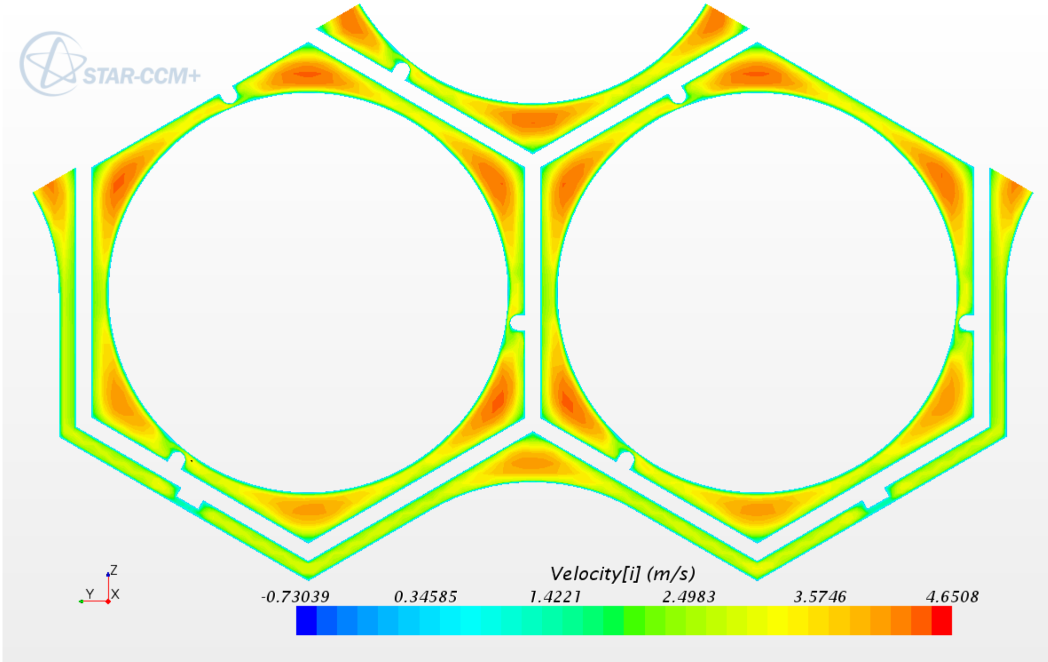

Figure 7-2: Streamwise velocity contour at x = -0.020m

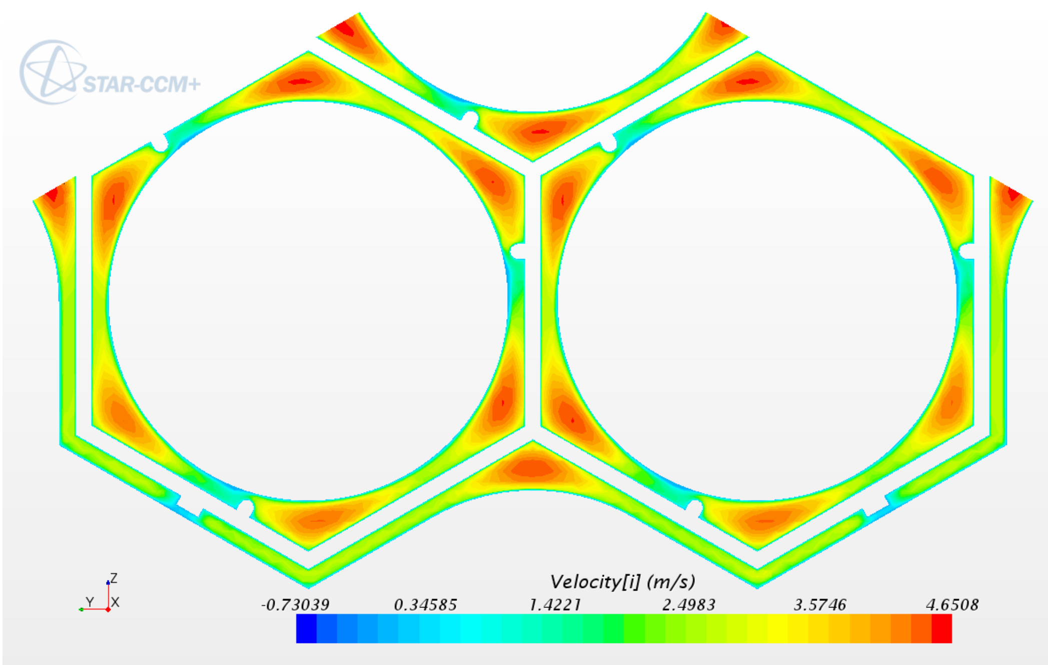

Figure 7-3: Streamwise velocity contour at x = -0.0001m

Figure 7-2 and Figure 7-3 show the streamwise velocity field near the upstream edge and downstream edge of the grid spacer, respectively. The flow fields are somewhat similar except for the low velocity region that forms on the low pressure side of the bars. This occurs because of the pitched orientation of the bars, as seen previously in Figure 4-4. The flow is unable to fully circulate around the bars due to the very small flow path that exists between the bar and the rod surface. This flow path is shown in Figure 7-4 where the arrows represent the velocity vector and the colour bar represents the velocity in the z direction.

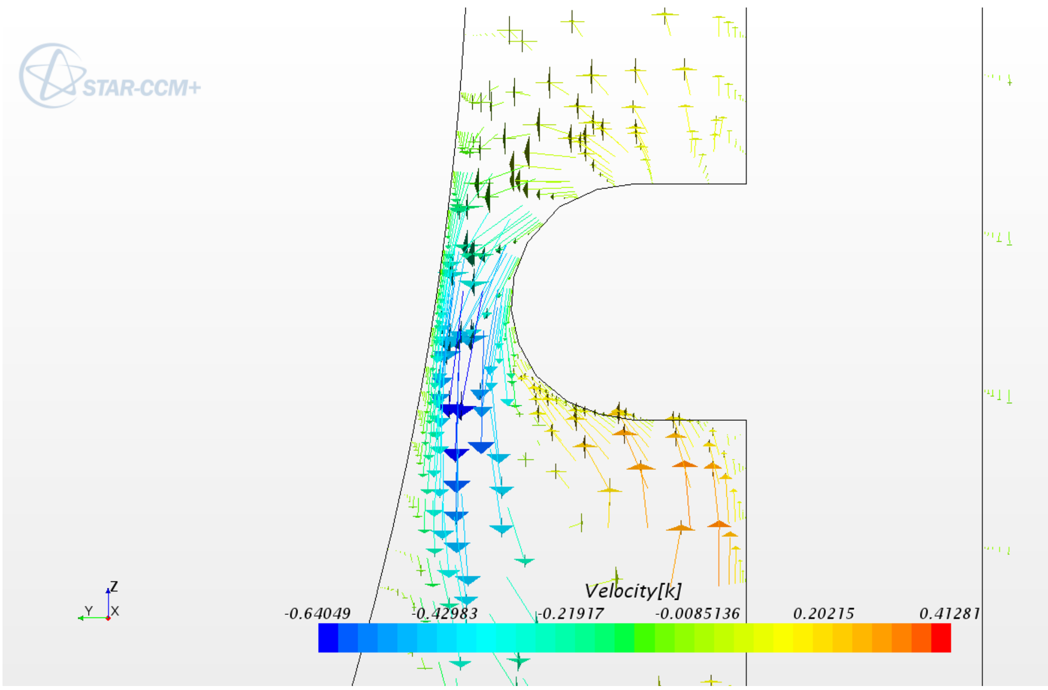

Figure 7-4: Circulation flow around the bar structure at x = -0.020m

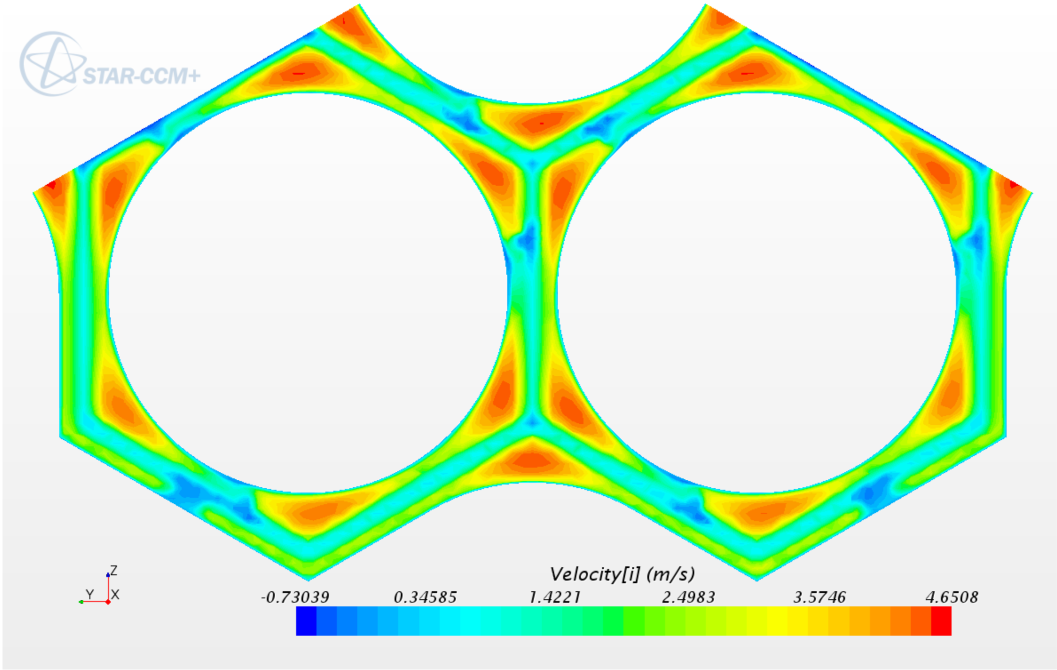

Figure 7-5: Streamwise velocity contour at x = 0.0001m

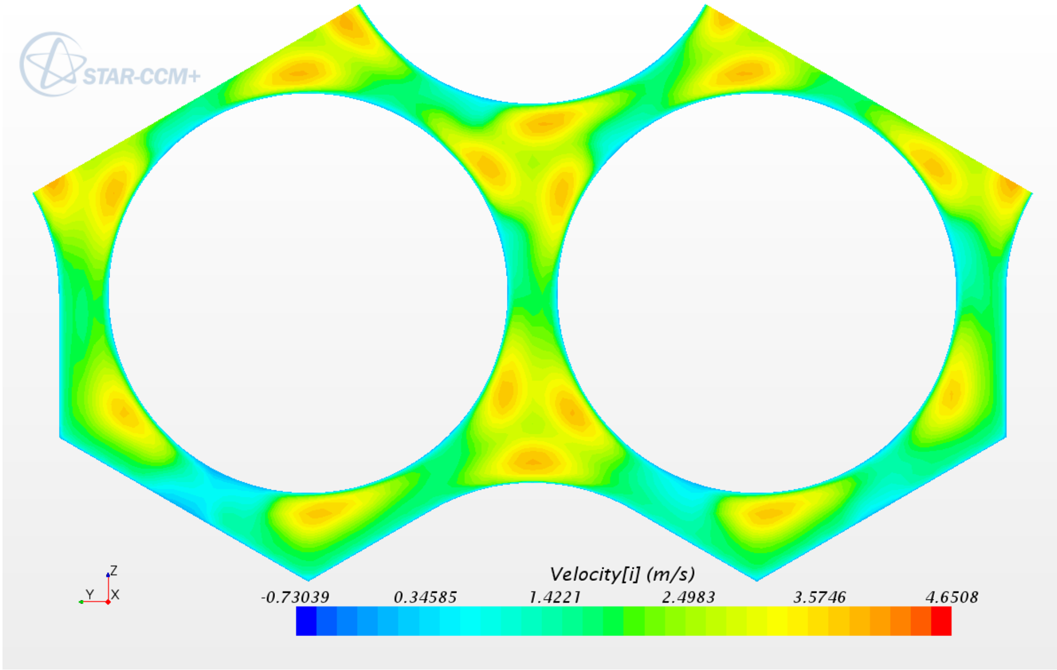

Figure 7-6: Streamwise velocity contour at x = 0.0058m

Figure 7-5 and Figure 7-6 show the streamwise velocity field immediately downstream and 2 D_h downstream of the grid spacer, respectively. The velocity field evolves from being defined by recirculation zones and strong velocity gradients to a quite diffusive state within only 2 D_h. It is also noted that convection in the plane normal to the streamwise direction is very nearly non-existent and the field is predominately diffusive shortly downstream of the grid spacer.

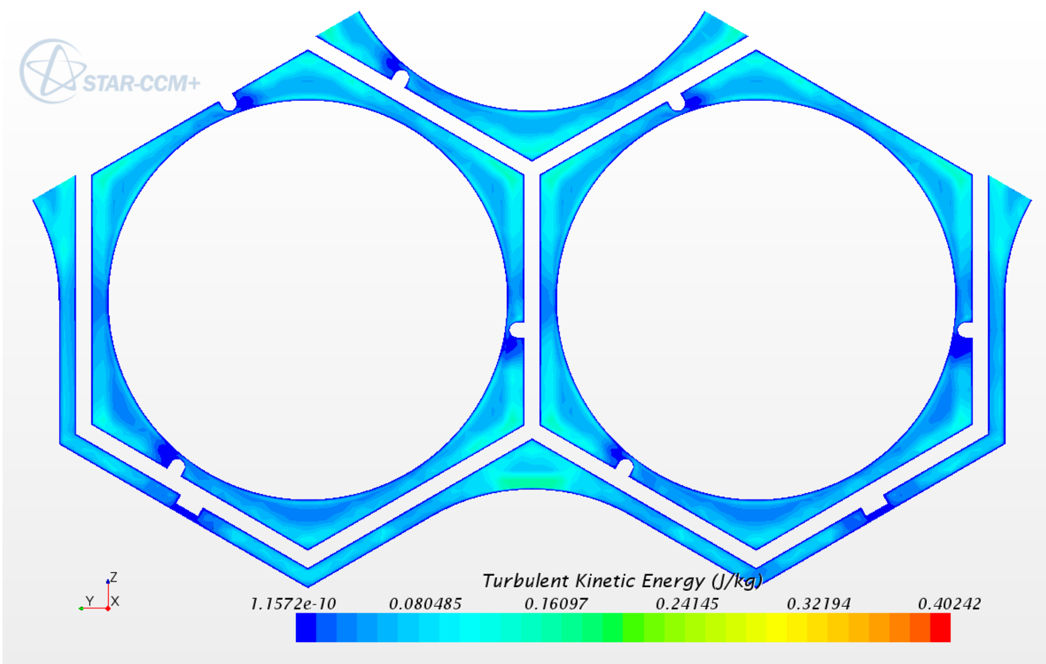

Figure 7-7: Turbulent kinetic energy contour at x = -0.020m

There is a formation of a region of low turbulent kinetic energy on the low pressure side of the bars. This region develops quickly within the grid spacer

(Figure 7-7) and is most prominent at the downstream edge of the grid spacer (Figure 7-8).

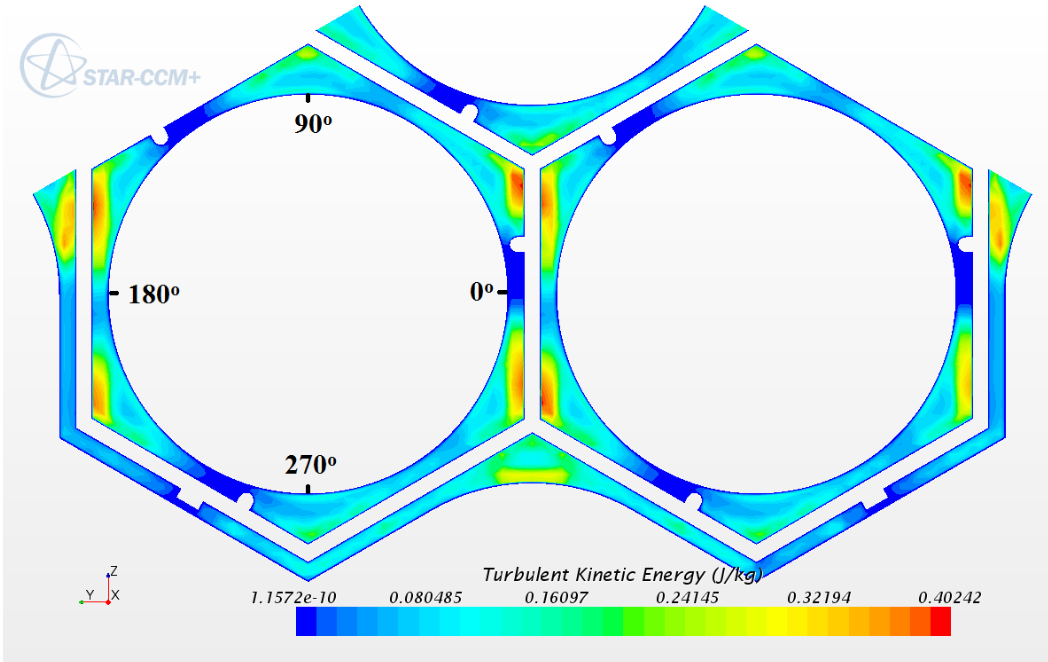

Figure 7-8: Turbulent kinetic energy contour at x = -0.0001m

The figures show that three regions of low turbulent kinetic energy are formed around each rod and are seen to be most prevalent near the downstream edge of the grid spacer (Figure 7-8 and Figure 7-9). The turbulent field diffuses (by the dominant action of the eddy viscosity) to give Figure 7-10 which shows six regions of low turbulent kinetic energy around each rod. The regions of low turbulent kinetic energy also have low wall shear stress magnitude and vice versa, as expected.

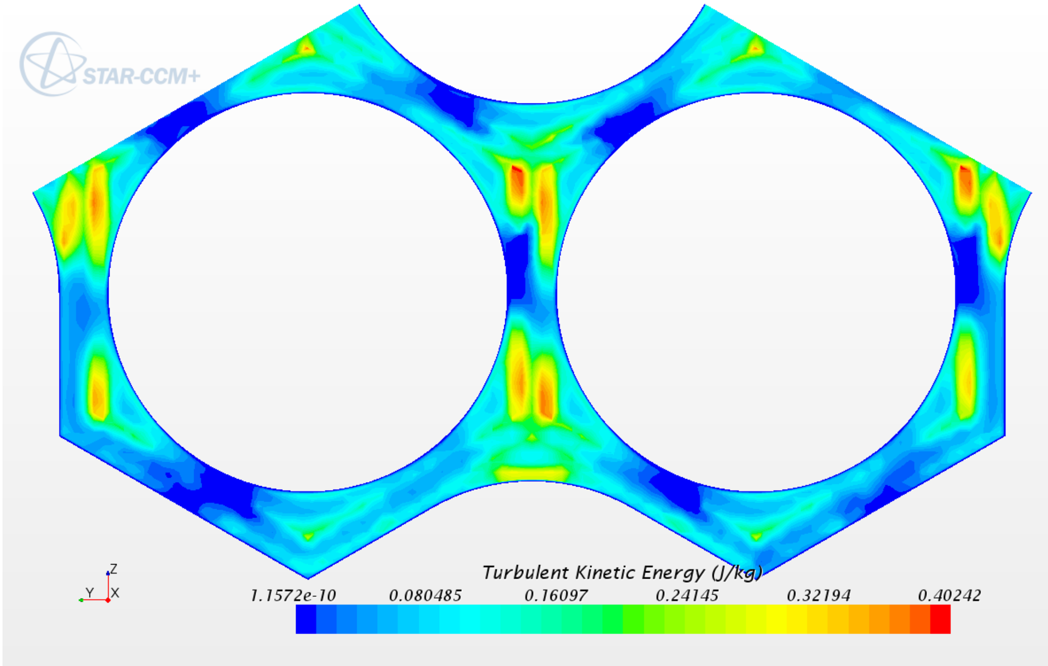

Figure 7-9: Turbulent kinetic energy contour at x = 0.0001m

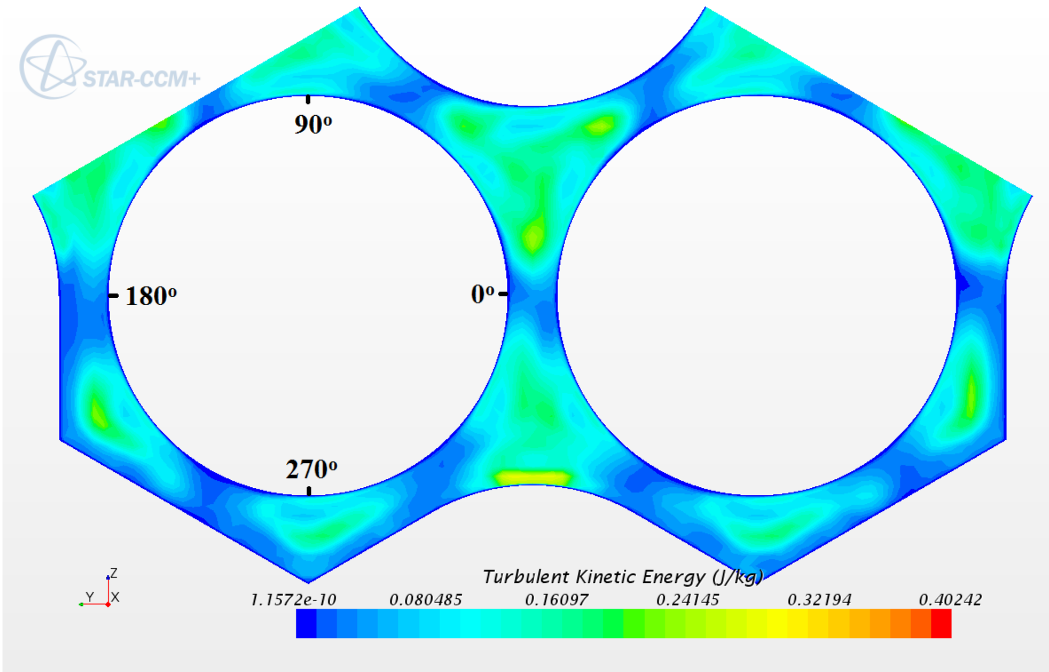

Figure 7-10: Turbulent kinetic energy contour at x = 0.0058m

The wall shear stress magnitude of the peripheral rod along the azimuthal direction is given at various streamwise positions in Figure 7-11. Only one-third (120^o) of the rod is examined as the results are periodic within the grid spacer. The azimuthal positions can be referenced using Figure 7-8 and Figure 7-10. The wall shear stress shows a large peak at 68^o near the upstream edge of the grid spacer. This peak is associated with the constriction of flow path as the grid spacer is encountered by the flow. As the flow travels downstream through the grid spacer this region becomes one of low to moderate wall shear stress. The flow develops and the bulk of the flow is redistributed to the larger flow cross sections seen at 30^o and 90^o.

The peak in wall shear stress magnitude was expected to be present at 60^o, as this is the region where the flow is most constricted. It is believed that the proximity of the bar in the centre rod grid spacer cell has an effect on this. By the same logic, a peak in wall shear stress magnitude was expected to be present at 120^o, but the presence of the bar very close to this region creates a stagnation zone upstream of the grid spacer's edge, this causes the flow to divert from this point and therefore no high velocity gradients are seen here.

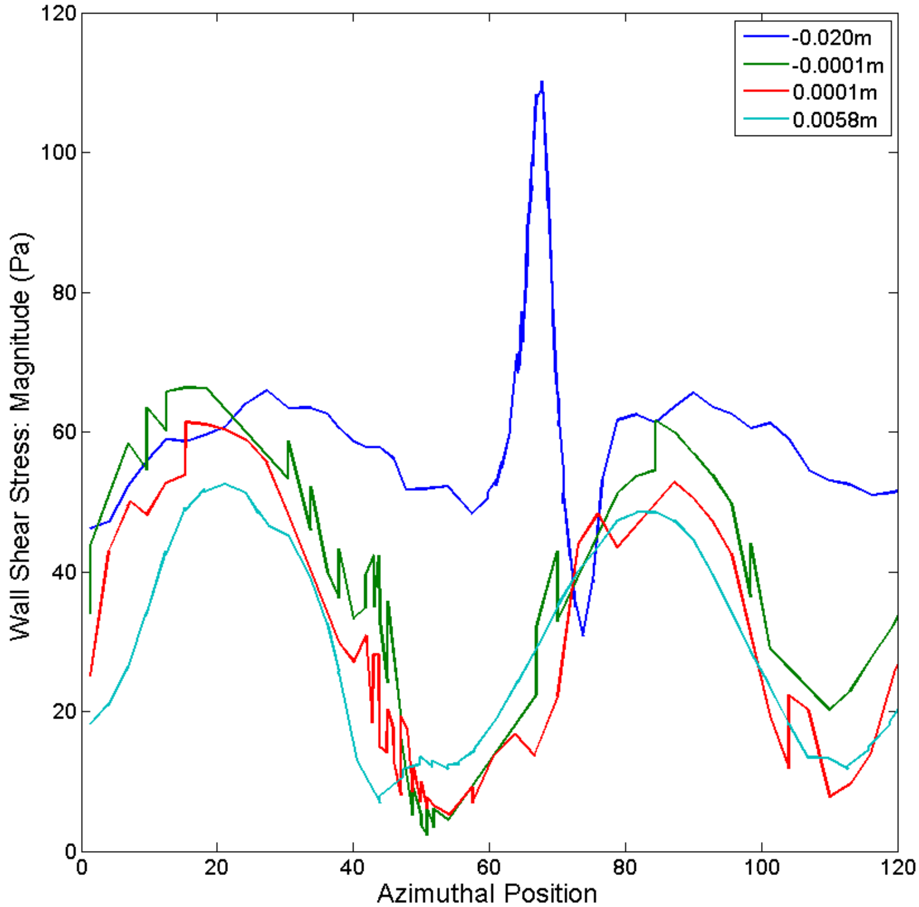

Figure 7-11: Peripheral rod wall shear stress magnitude along the azimuthal direction at various streamwise positions

The further downstream calculations of wall shear stress magnitude are consistent with the explanation that the flow has been redistributed to larger flow cross sections and there exists little flow within the constricted flow paths. Therefore, the minimums of wall shear stress magnitude are seen to be in close proximity to 0^o, 60^o and 120^o.

7.3 Heated Case B1

7.3.1 Heat Transfer Enhancement

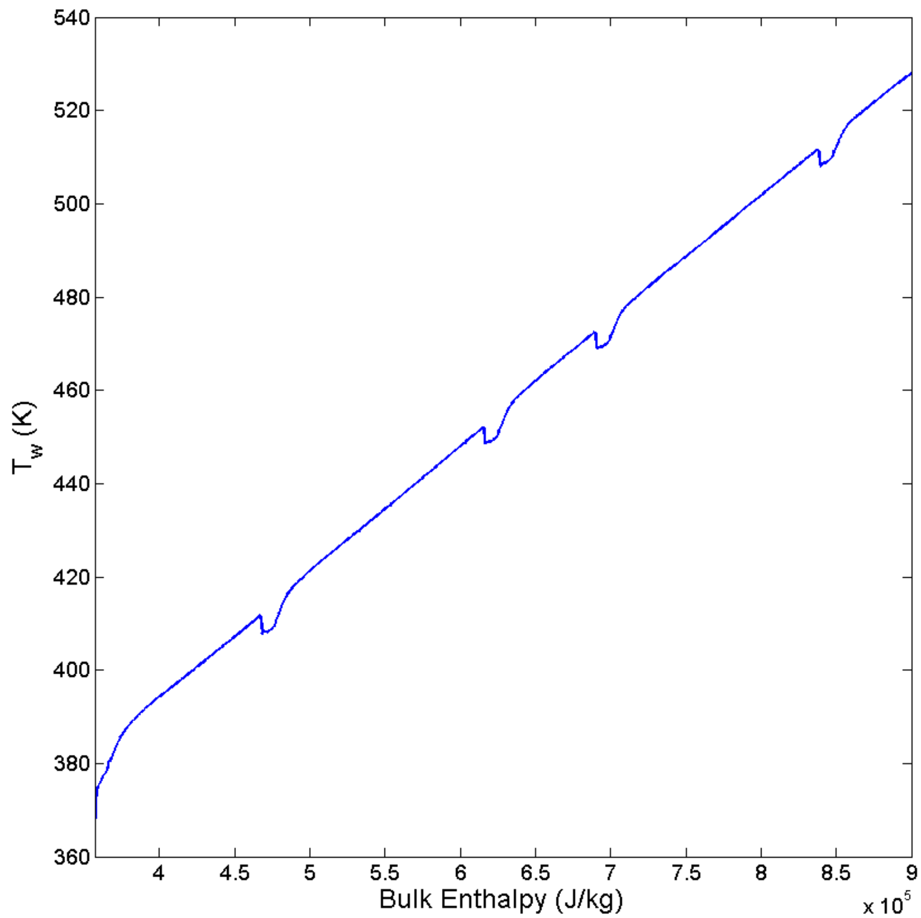

Figure 7-12: Heated Case B1 - T_w vs. Bulk Enthalpy along the entire test section at the *270°* azimuthal position of the centre rod

The heat transfer enhancement effect of the grid spacer's can be seen in Figure 7-12. The fifth grid spacer is chosen to show (Figure 7-13) the typical wall temperature behaviour through this region of heat transfer enhancement. The enhancement begins just upstream of the grid spacer as a stagnation region at the upstream edge forms and this acts to redistribute the flow closer to the rod walls, therefore increasing the wall shear stress magnitude and enhancing heat transfer. The heat transfer enhancement is evident shortly downstream of the grid spacer as well. In this region the turbulent kinetic energy is decaying from its peak at the downstream edge of the grid spacer.

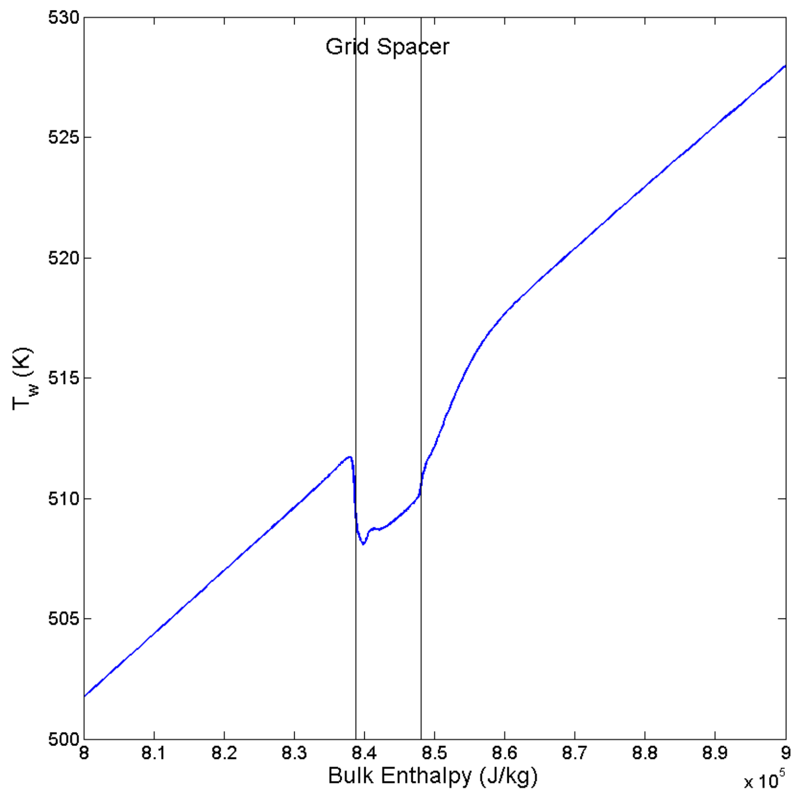

Figure 7-13: Heated Case B1 - T_w vs. Bulk Enthalpy at the 5th grid spacer at the *270°* azimuthal position of the centre rod

7.3.2 Rod Wall Non-Uniformities

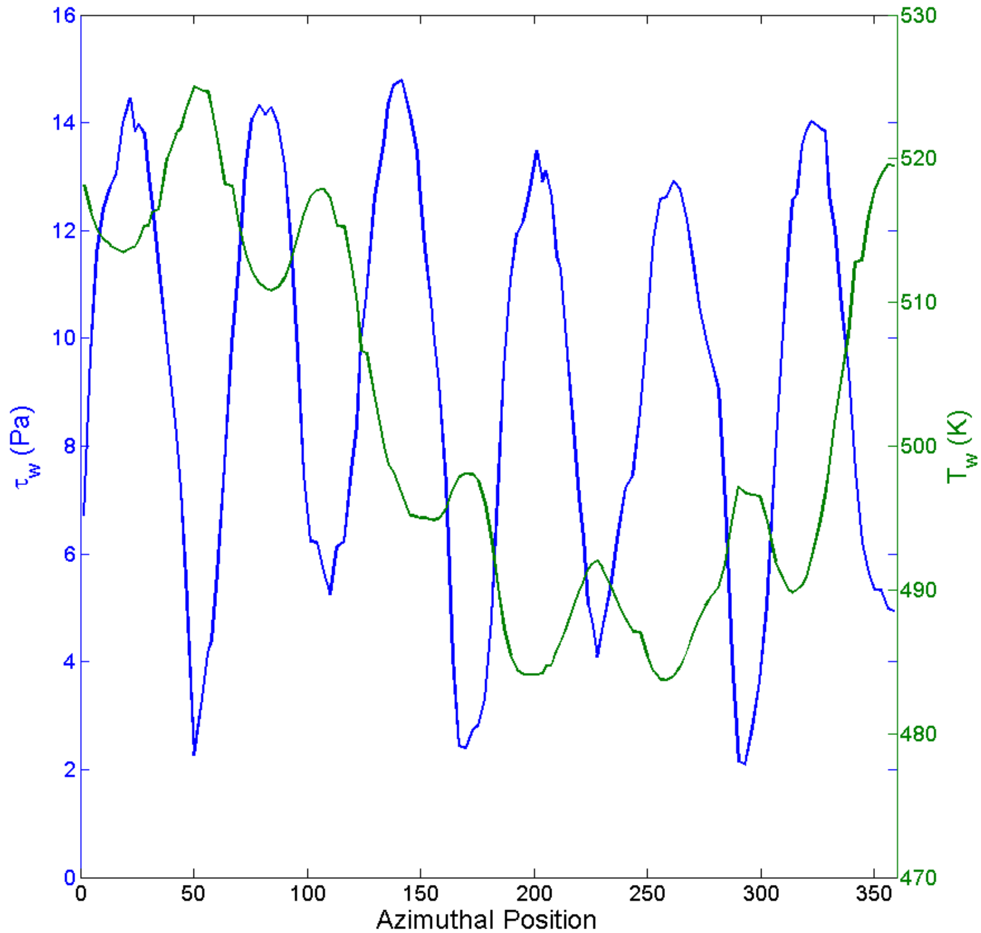

Figure 7-14: Heated Case B1 - Peripheral rod wall shear stress magnitude and T_w along the azimuthal direction 2 D_h downstream of the 5th grid spacer

Figure 7-14 shows the non-uniformities in the peripheral rod wall shear stress magnitude and its corresponding effect on the wall temperature. Azimuthal positions of local minima and maxima of wall shear stress magnitude are shown to correspond to local maxima and minima of wall temperature, as expected.

These non-uniformities are due to varying flow conditions (minimal narrow gap flow, high subchannel flow) seen by the rod wall in the azimuthal direction and is slightly exacerbated by the nearly non-existent convection in the plane normal to the streamwise direction.

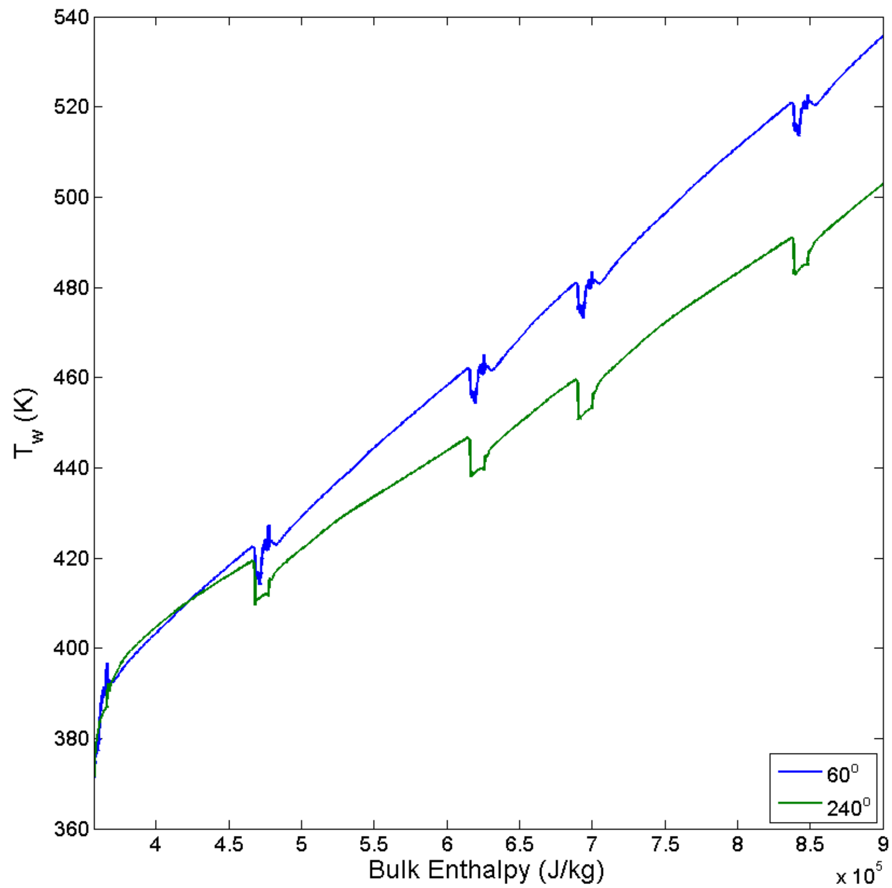

Figure 7-15: Heated Case B1 - T_W vs. Bulk Enthalpy along the entire test section at the *60°* and *240°* azimuthal position of the peripheral rod

As expected the azimuthal position of maximum temperature is calculated to be in the narrow gap facing the centre rod, at *60°*, and the azimuthal position of the minimum temperature is calculated to be in the region facing the shroud, at approximately 210^o and 270^o. Figure 7-15 shows that at the outlet of the test section this wall temperature non-uniformity is approximately *35K*.

7.4 Heated Case B2

7.4.1 Heat Transfer Enhancement

As in the previous heated case, the grid spacers have a similar effect in enhancing the heat transfer to the coolant. Whereas, the heated case B1 wall temperature results were shown to be a fairly linear function of bulk enthalpy, the heated case B2 wall temperature results (Figure 7-16) are not.

This is due to largely variable properties in the vicinity of T_{pc}. It should be noted that the heat transfer is enhanced more by each successive grid spacer; this is due to the increase in *Re* along the test section.

Figure 7-17 shows the most drastic enhancement of heat transfer at the fifth grid spacer. As previously, the stagnation region slightly upstream of the grid spacer acts to initiate the enhancement prior to the flow reaching the upstream edge. The heat transfer also remains enhanced as the turbulent kinetic energy decays from its peak value at the downstream edge.

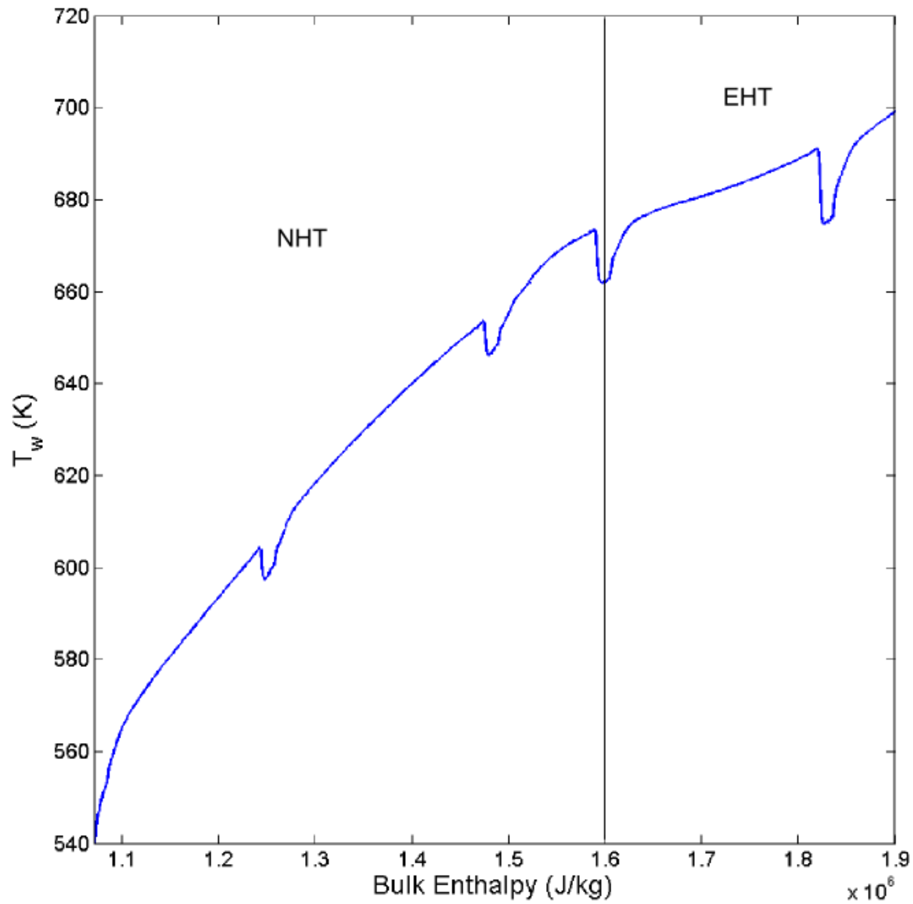

Figure 7-16: Heated Case B2 - T_w vs. Bulk Enthalpy along the entire test section at the *270°* azimuthal position of the centre rod

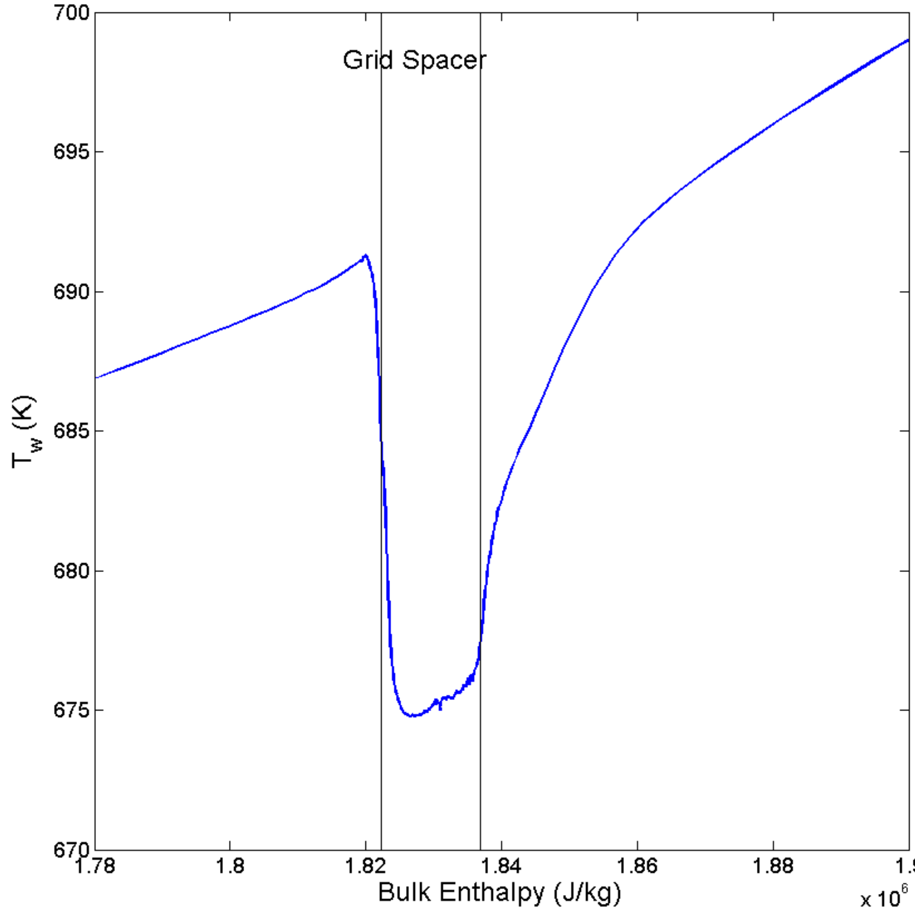

Figure 7-17: Heated Case B2 - T_w vs. Bulk Enthalpy at the 5th grid spacer at the *270°* azimuthal position of the centre rod

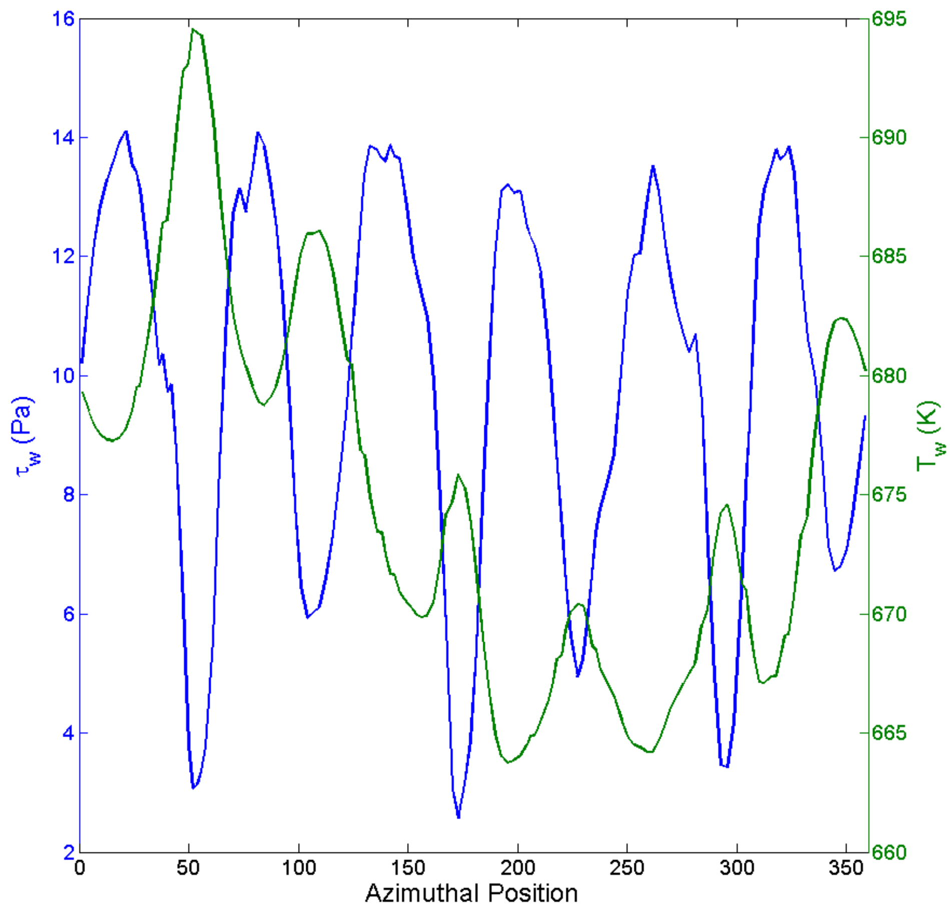

Figure 7-18: Heated Case B2 - Peripheral rod wall shear stress magnitude and T_w along the azimuthal direction 2 D_h downstream of the 5th grid spacer

Figure 7-18 shows the relationship between wall shear stress magnitude and wall temperature. These results are similar to those of the heated case B1 as seen in Figure 7-14 and the varying azimuthal conditions cause these rod wall non-uniformities that are exacerbated by the lack of convection in the plane perpendicular to the streamwise direction.

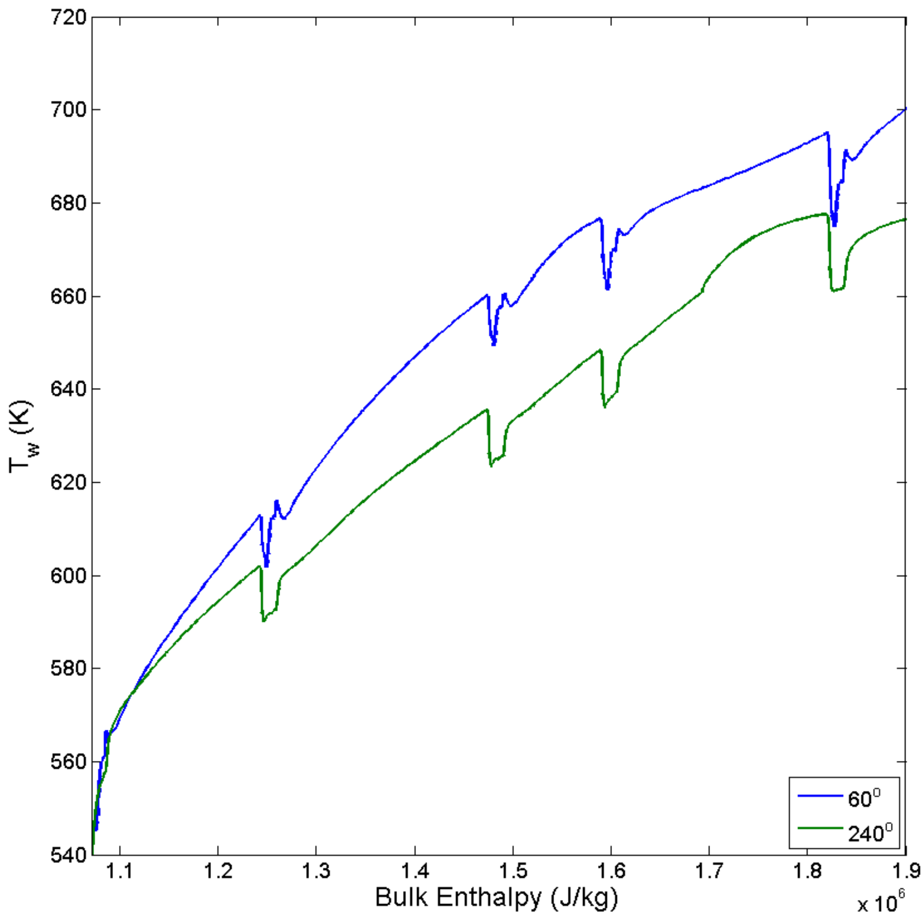

Figure 7-19: Heated Case B2 - T_w vs. Bulk Enthalpy along the entire test section at the *60°* and *240°* azimuthal position of the peripheral rod

Again, as expected, the highest region of wall temperature is present at the azimuthal position of *60°*, and the lowest region of wall temperature is present at the azimuthal position of *210°* and *270°*.

7.5 Prediction Bias

The most apparent shortcoming of the EVMs can be seen in Figure 7-14 and Figure 7-18 where there are large non-uniformities in rod wall shear stress magnitude and wall temperature. This is, in part, due to the inability of models' developed using the Boussinesq approximation to predict the anisotropic nature of the Reynolds stress tensor (Figure 5-23) to any degree of accuracy. A failure to predict the Reynolds stress tensor results in a failure to resolve the secondary flows (see Equation 2.9) known to be present in rod bundle flows. Also, previous studies in rod bundles have shown that there exists increased subchannel mixing associated with complex turbulent interaction in the gap region which is not resolved by RANS models [**65**] [**66**].

The choice of EVM has precluded the resolution of the secondary flows as well as the complex turbulent interaction in the gap region. Both of these phenomena contribute to increased convection in the plane perpendicular to the streamwise direction and therefore the EVM's predictions are expected to suffer from increased rod wall shear stress and wall temperature non-uniformities in the azimuthal direction.

Therefore, the choice of the SST turbulence model will bias the wall temperature results in both directions. There will be an over-prediction of wall temperature for the centre rod as well as the regions of the peripheral rods that face the centre rod and there will be an under-prediction of wall temperature for the regions of the peripheral rods that face the shroud.

Chapter 8

Conclusions

A methodology for CFD simulations using STAR-CCM+ 9.02.005 has been developed for submission to the GIF SCWR computational benchmark exercise. This methodology included a detailed examination of the physical phenomena important in modelling heat transfer to super-critical water flowing upward in a 7 rod bundle. The separate effects study revealed the prediction bias of the EVMs and the practical difficulties in applying RSMs. Discretization error was then analysed in a mesh sensitivity study. Finally, the results of pressure drop and wall temperature were analyzed.

This work has acted to highlight the shortcomings as well as the strengths of the EVMs. The choice of the SST turbulence model has precluded the resolution of secondary flows and the complex turbulent interaction. However, this preclusion will affect the wall temperature predictions in a known way. Therefore, it can be concluded that the SST turbulence model will give conservative wall temperature predictions near the centre of the bundle and non-conservative wall temperature predictions near the perimeter of the bundle. The simple fact that SST's weakness is well known gives the author confidence in recommending it as a coarse wall temperature estimate, able to accurately predict the average wall temperature.

A formal summary and recommendations of each of the benchmark participants will be assembled in an academic paper following the release of the experimental results and analysis by the benchmark organizing committee. This academic paper will be the start of an assembly of best practice guidelines in modelling heat transfer to super-critical water coolant in bundles. The lessons learned will also help to better understand the mechanisms of heat transfer as a complement to experimental programs.

A number of possible extensions can be made from this work in order to further understand the mechanisms and modelling of heat transfer to supercritical water within bundle geometries. In the context of this specific work, a study of the sensitivity of the wall temperature to changes in the turbulent Prandtl number would have been helpful. In addition, a study of the azimuthal heat flux within the clad could give insight into the precise causes of the rod wall temperature non-uniformities. In addition some unexpected behaviour was observed in some of the predictions (e.g., the small temperature increase immediately downstream of the spacers), and these should be studied further.

Currently, the SCWR community lacks experimental data of any kind describing the velocity field for coolant at supercritical pressure. Without this extremely valuable piece of knowledge experiments that define the wall temperature distribution within any type of geometry can be used to improve the turbulence models.

Fundamental experimental studies in tube geometries at low *Re* can be compared to DNS data to further the understanding of each heat transfer regime and this understanding can be used to refine the turbulence models.

Applied experimental cases – similar to that of the JAEA – can be used to explore heat transfer at many different flow conditions that include the three heat transfer regimes. These cases can be used to validate various computational approaches much in the same way as described in the present work.

Bibliography

[1] U.S. DoE, "A technology roadmap for generation IV nuclear energy systems," Nuclear Energy Research Advisory Committee and the Generation IV International Forum, 2002.

[2] I.L. Pioro and R.B. Duffrey, "Experimental heat transfer in supercritical water following inside channels (survey)," *Nuclear Engineering and Design*, vol. 235, pp. 2407-2430, 2005.

[3] A.N. Kolmogorov, "Local structure of turbulence in incompressible viscous fluid for very large Reynolds number," *Doklady AN. SSSR*, vol. 30, pp. 299-303, 1941.

[4] D.C. Wilcox, *Turbulence Modeling for CFD*, 2nd ed. La Canada, California: DCW Industries, 1998.

[5] B.E. Launder, G.J. Reece, and W. Rodi, "Progress in the development of a Reynolds-stress turbulence closure," *Journal of Fluid Mechanics*, vol. 68, no. 03, pp. 537-566, 1975.

[6] CD-adapco, USER GUIDE STAR-CCM+ Version 9.02, 2014.

[7] W.P. Jones and B.E. Launder, "The prediction of laminarization with a two-equation model of turbulence," *International Journal of Heat and Mass Transfer*, vol. 15, pp. 301-314, 1972.

[8] D.C. Wilcox, "Re-assessment of the scale-determining equation for advanced turbulence models," *AIAA Journal*, vol. 26, no. 11, pp. 1299-1310, 1988.

[9] E.R. van Driest, "On turbulent flow near a wall," *Journal of Aeronautical Sciences*, vol. 11, pp. 1007-1011, 1956.

[10] M. Wolfstein, "The velocity and temperature distribution in one-dimensional flow with turbulence augmentation and pressure gradient," *International Journal of Heat and Mass Transfer*, vol. 41, pp. 3161-3176, 1969.

[11] J. Mahaffy et al, "Best practice guidelines for the use of CFD in nuclear reactor safety applications," OECD/NEA/CSNI, NEA/CSNI/R(2007)5, 2007.

[12] (2006) Higher National Computing: Verification and Validation. [Online]. http://www.sqa.org.uk/e-learning/SDPL03CD/page_16.htm

[13] I.L. Pioro, H.F. Khartabil, and R.B. Duffrey, "Heat transfer to supercritical fluids flowing in channels - empirical correlations (survey)," *Nuclear*

Engineering and Design, vol. 230, pp. 69-91, 2004.

[14] E.A. Krasnoshchekov and V.S. Protopopov, "About heat transfer in flow of carbon dioxide and water at supercritica region ofl state parameters," *Thermal Engineering*, vol. 10, p. 94, 1960.

[15] E.A. Krasnoshchekov and V.S. Protopopov, "Heat transfer at supercritical region in flow of carbon dioxide and water in tubes," *Thermal Engineering*, vol. 12, pp. 26-30, 1959, (in Russian).

[16] E.A. Krasnoshchekov, V.S. Protopopov, F. Van, and I.V. Kuraeva, "Experimental investigation of heat transfer for carbon dioxide in the supercriitcal region," RAND Corporation, Santa Monica, California, R-451 PR, 1967.

[17] B.S. Petukhov, E.A. Krasnoshchekov, and V.S. Protopopov, "An investigation of heat transfer to fluids flowing in pipes under supercritical condition," in *Proceedings of the ASME Int. Dev. Heat Transf.*, New York, NY, 1961, pp. 569-578.

[18] J.D. Jackson and J. Fewster, "Forced convection data for supercritical pressure fluids," Heat Transfer Fluid Flow Science, HTFS 21540, 1975.

[19] J.D. Jackson, "Validation of an extended heat transfer equation for fluids at

supercritical pressure," in *Proceedings of the 4th Int. Sym. on SCWRs*, Heidelberg, Germany, 2009.

[20] J.D. Jackson, "Consideration of the heat transfer properties of supercritical pressure water in connection with the cooling of advanced nuclear reactors," in *Proceedings of the 13th Pacific Basin Nuclear Conference*, Beijing, China, 2002.

[21] H. Kim, Y.Y. Bae, H.Y. Kim, J.H. Song, and B.H. Cho, "Experimental investigation on the heat transfer characteristics in a vertical upward flow of supercritical carbon dioxide," in *Proceedings of the Int. Con. on Adv. in Nuc. Power Plants*, La Grange Park, IL, 2006, pp. 372-381.

[22] J.D. Jackson, "Some strking features of heat transfer with fluids at pressures and temperature near the critical point," in *Int. Conf. on Energy Conversion & Application*, Wuhan, China, 2001.

[23] K. Yamagata, K. Nishikawa, S. Hasegawa, T. Fujii, and S. Yoshida, "Forced convective heat transfer to supercritical water flowing in tubes," *International Journal of Heat and Mass Transfer*, vol. 15, pp. 2575-2593, 1972.

[24] J.D. Jackson, "A semi-empirical model of turbulent convective heat transfer to fluids at supercritical pressure," in *Proceedings of the 16th International*

Conference on Nuclear Engineering, Orlando, Florida, 2008.

[25] P.M. Moretti and W.M. Kays, "Heat transfer to a turbulent boundary layer with varying free-stream velocity and varying surface temperature- An experimental study," *International Journal of Heat and Mass Transfer*, vol. 8, pp. 1187-1202, 1965.

[26] D.P. Mikielewicz, A.M. Shehata, J.D. Jackson, and D.M. McEligot, "Temperature, velocity and mean turbulence structure in strongly heated internal gas flows. Comparison of numerical predictions with data," *International Journal of Heat and Mass Transfer*, vol. 45, no. 21, pp. 4333-4352, 2002.

[27] D. Palko and H. Anglart, "Theoretical and numerical study of heat transfer deterioration in high performance light water reactor," *Science and Technology of Nuclear Installations*, 2008.

[28] S. He, W.S. Kim, and J.D. Jackson, "A computational study of convective heat transfer to carbon dioxide at a pressure just above the critical value," *Applied Thermal Engineering*, vol. 28, pp. 1662-1675, 2008.

[29] S. Koshizuka, N. Takano, and Y. Oka, "Numerical analysis of deterioration phenomena in heat transfer to supercritical water," *International Journal of*

Heat and Mass Transfer, vol. 38, no. 16, pp. 3077-3084, 1995.

[30] W.P. Jones and B.E. Launder, "The calculation of low-Reynolds number phenomena with a two-equation model of turbulence," *International Journal of Heat and Mass Transfer*, vol. 16, no. 6, pp. 1119-1130, 1973.

[31] F. Roelofs, "CFD analyses of heat transfer to supercritical water flowing vertically upward in a tube," Netherlands Ministry of Economic Affairs, 21353/04.60811/P, 2004.

[32] V. Yakhot, S.A. Orszag, S. Thangam, T.B. Gatski, and C.G. Speziale, "Development of turbulence models for shear flows by a double expansion technique," *Physics of Fluids A: Fluid Dynamics*, vol. 4, p. 1510, 1992.

[33] B.E. Launder and N. Shima, "Second moment closure for the near-wall sublyaer: Development and application," *AIAA Journal*, vol. 27, pp. 1319-1325, 1989.

[34] F.R. Menter, "Two-equation eddy-viscosity turbulence modeling for engineering applications," *AAIA Journal*, vol. 32, pp. 1598-1605, 1994.

[35] A.P. Ornatskij, L.F. Glushchenko, and S.I. Kalachev, "Heat transfer with rising and falling flows of water in tubes of small diameter at supercritical pressures," *Thermal Engineering*, vol. 18, no. 5, pp. 137-141, 1971.

[36] M.E. Shitsman, "Impairment of the heat transmission at supercritical pressures," *High Temperatures*, vol. 1, no. 2, pp. 237-244, 1963.

[37] S. Kim, Y. Kim, Y. Bae, and B. Cho, "Numerical simulations of the vertical upward flow of water in a heated tube at supercritical system pressure," in *Proceedings of ICAPP '04*, Pittsburgh, PA, 2004.

[38] P.A. Durbin, "Separated flow computations with the k-epsilon-v-squared model," *AIAA Journal*, vol. 33, no. 4, pp. 659-664, 1995.

[39] K. Abe, T. Kondoh, and Y. Nagano, "A new turbulence model for predicting fluid flow and heat transfer in separating and reattaching flows - I. Flow field calculations," *International Journal of Heat and Mass Transfer*, vol. 37, no. 1, pp. 139-151, 1994.

[40] Y. Zhu, "Numerical investigation of the flow and heat transfer within the core cooling channel of a supercritical water reactor," *PhD Dissertation, University of Stuttgart*, 2010.

[41] L. Glushchenko and O. Gandzyuk, "Temperature conditions at the wall of an annular channel with internal ehating at supercritical pressures," *High Temperatures*, vol. 10, pp. 734-738, 1972.

[42] X. Cheng, B. Kuang, and Y.H. Yang, "Numerical analysis of heat transfer in

supercritical water cooled flow channels," *Nuclear Engineering and Design*, vol. 237, pp. 240-252, 2007.

[43] C.G. Speziale, S. Sarkar, and T.B. Gatski, "Modeling the pressure-strain correlation of turbulence: an invariant dynamical systems approach," *Journal of Fluid Mechanics*, vol. 227, pp. 245-272, 1991.

[44] J. Yang, Y. Oka, Y. Ishiwatari, J. Liu, and J. Yoo, "Numerical investigation of heat transfer in upward flows of supercritical water in circular tubes and tight fuel rod bundles," *Nuclear Engineering and Design*, vol. 237, pp. 420-430, 2007.

[45] M.J. Watts and C.T. Chou, "Mixed convection heat transfer to supercritical pressure water," in *Proceedings of the 7th International Heat Transfer Conference*, Munich, 1982, pp. 495-500.

[46] A.A. Bishop, R.O. Sandberg, and L.S. Tong, "Forced convection heat transfer to water at near-critical temperatures and supercritical pressures," Westinghouse Electric Corporation, Pittsburgh, WCAP-2056, Part IV, 1964.

[47] S. Hassid and M. Poreh, "A turbulent energy dissipation model for flows with drag reduction," *Journal of Fluid Engineering*, vol. 100, pp. 107-112, 1978.

[48] J. Nikuradse, "Untersuchungen uber die Geschwindigteitsverteilung in turbulenten Stromungen," *PhD Dissertation, Gottingen*, 1926.

[49] L. Prandtl, "Uber den Reibungswiderstand stromenderluft," *Ergeb. Aerodyn. Versuch., Gottingen, III Series*, 1927.

[50] E. Brundrett and W.D. Baines, "The production and diffusion of vorticity in duct flow," *Journal of Fluid Mechanics*, vol. 19, no. 3, pp. 375-394, 1964.

[51] F.B. Gessner and J.B. Jones, "On some aspects of fully developed turbulent flow in a rectangular channel," *Journal of Fluid Mechanics*, vol. 23, pp. 689-713, 1965.

[52] H.J. Perkins, "The formation of streamwise vorticity in turbulent flow," *Journal of Fluid Mechanics*, vol. 44, pp. 721-740, 1970.

[53] A.C. Trupp and R.S. Azad, "The structure of turbulent flow in triangular array rod bundles," *Nuclear Engineering and Design*, vol. 32, pp. 47-84, 1974.

[54] J. Laufer, "The structure of turbulence in fully developed pipe flow," NACA, 1174, 1954.

[55] B.E. Launder and W.M. Ying, "Prediction of flow and heat transfer in ducts of square cross section," in *Proceedings of the Institution of Mechanical*

Engineers, 1973, pp. 455-461.

[56] G.J. Reece, "A generalized Reynolds stress model of turbulence," *PhD thesis, Imperial College, London*, 1976.

[57] A. Melling and J.H. Whitelaw, "Turbulent flow in a rectangular duct," *Journal of Fluid Mechanics*, vol. 78, pp. 289-315, 1976.

[58] G. Mompean, S. Gavrilakis, L. Machiels, and M.O. Deville, "On predicting the turbulence induced secondary flows using nonlinear k models," *Physics of Fluids*, vol. 8, no. 7, pp. 1856-1868, 1996.

[59] S. Nisizima, "A numerical study of turbulent square duct flow using an anisotropic k-epsilon model," *Theoretical and Computational Fluid Dynamics*, pp. 61-71, 1990.

[60] M.M. Gibson and B.E. Launder, "Ground effects on pressure fluctuations in the atmospheric boundary layer," *Journal of Fluid Mechanics*, vol. 86, no. 3, pp. 491-511, 1978.

[61] T. Misawa et al., "Heat transfer experiments and numerical analysis of supercritical pressure water in seven-rod test bundle," in *Proceedings of NURETH-13*, Kanazawa City, Japan, 2009.

[62] X. Zhu, S. Morooka, and Y. Oka, "Numerical investigation on practicability of reducing MCST by using grid spacer in a tight rod bundle," *Nuclear Engineering Design*, vol. 270, pp. 198-208, 2014.

[63] C.G. Speziale, R. Abid, and E.C. Anderson, "A critical evaluation of two-equation models for near wall turbulence," NASA, Hampton, Virginia, ICASE Report No. 90-46, 1990.

[64] W. Rodi, N.N. Mansour, and V. Michelassi, "One-equation near-wall turbulence modelling with the aid of direct simulation data," *Journal of Fluids Engineering*, vol. 2, pp. 196-205, 1993.

[65] L. Meyer and K. Rehme, "Large-scale turbulence phenomena in compound rectangular channels," *Experimental Thermal and Fluid Science*, vol. 8, pp. 286-304, 1994.

[66] L. Meyer, "From discovery to recognition of periodic large scale vortices in rod bundles as source of natural mixing between subchannels - A review," *Nuclear Engineering and Design*, vol. 240, pp. 1575-1588, 2010.

Appendix A

Two Layer Formulation of Wolfstein [10]

The two layer formulation is used with turbulence models that employ the solution of the ε transport equation. Alternatives to the two layer approach are the use of damping functions that act to modify the production and dissipation of ε as well as modify the turbulent viscosity. Also, the use of wall functions along with a coarse mesh is an option but it is undesirable for applications where the resolution of the boundary layer is of utmost importance. The following is a description of the two layer formulation of Wolfstein [**10**].

In the case of the RSM linear pressure strain two layer approach, the general idea is to solve the full set of transport equations in regions remote from walls and when in the near wall region the value of ε is prescribed algebraically and blended with its value computed by transport equation.

The two layer model makes use of a length scale function $l_\varepsilon = f\left(y, Re_y\right)$ and a turbulent viscosity ratio, $\frac{\mu_t}{\mu} = f(Re_y)$ [**6**]. Where y is the wall distance and $Re_y = \frac{\sqrt{k}y}{\nu}$. The dissipation rate is then computed from:

$$\varepsilon = \frac{k^{3/2}}{l_\varepsilon} \tag{A.1}$$

Where the length scale is:

$$l_\varepsilon = c_l y \left[1 - e^{-\frac{Re_y}{A_\varepsilon}}\right] \tag{A.2}$$

$$A_\varepsilon = 2c_l \tag{A.3}$$

$$c_l = \kappa {C_\mu}^{-3/4} \tag{A.4}$$

And the turbulent viscosity ratio in the near wall layer is:

$$\frac{\mu_t}{\mu} = Re_y {C_\mu}^{1/4} \kappa \left[1 - e^{-\frac{Re_y}{A_\mu}}\right] \tag{A.5}$$

Although the RSM doesn't employ the Boussinesq approximation, the turbulent viscosity away from the near wall region is defined as:

$$\mu_t = \rho C_\mu \frac{k^2}{\varepsilon} \tag{A.6}$$

The blending of the turbulent viscosity is done using the following equations:

$$\mu_t = \lambda \mu_t|_{away\ from\ wall} + (1-\lambda)\mu\left(\frac{\mu_t}{\mu}\right)_{2layer} \tag{A.7}$$

$$\lambda = \frac{1}{2}\left[1 + tanh\left(\frac{Re_y - Re_y{}^*}{A}\right)\right] \tag{A.8}$$

$$A = \frac{|\Delta Re_y|}{\operatorname{atanh}(0.98)} \tag{A.9}$$

Where $Re_y{}^* = 60$ gives the limit at which the two layer formulation is not used. All of the constants are given in Table A-1.

Table A-1: The constants used in the two layer formulation

$C_\mu = 0.09$	$\kappa = 0.42$	$A_\mu = 70$	$\Delta Re_y = 10$

Appendix B

SST Mesh Sensitivity

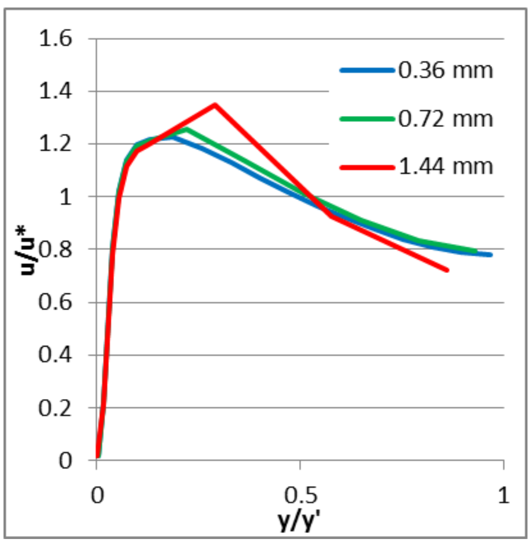

Figure B-1: Turbulent velocity along the *0°* for various values of bulk flow cell size with *y+ < 0.7*

Figure B-1 shows a slight sensitivity to bulk flow cell size. It appears that the results are converged for a bulk flow cell size of *0.72* mm.

It is seen that the results in Figure B-2 are moderately sensitive to *y+*. The results appear to be converged for a *y+ < 0.7*.

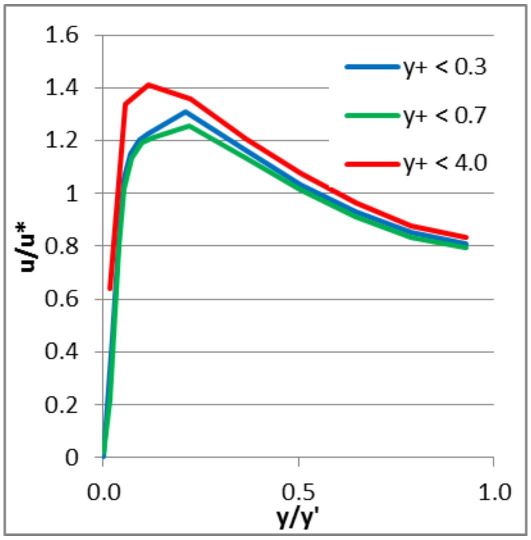

Figure B-2: Turbulent velocity along the *0°* for various values of *y+* with bulk flow cell size of *0.72* mm

The SST model will be solved using the same mesh parameters; bulk flow cell size = *0.72* mm and *y+ < 0.7*.

Appendix C

Computational Benchmark Submission

The spreadsheets are included that have been submitted to the GIF SCWR computational benchmark exercise organizers.

Calculation conditions of A1	
Parameter	Case A1
Fluid	Water
Inlet temperature (K)	297.35
Inlet pressure (MPa)	25
Flow rate (kg/s)	26.33

Calculated pressure drop
53.749 kPa

Heater rod name	Thermocouple No.	Installation angle of thermocouple (deg)	Axial position from the start of the heating length (m)	Thermocouple No. and installation angle of thermocouple (deg)										Calculated wall temperature (K)	
				30 (deg)	60 (deg)	120 (deg)	150 (deg)	180 (deg)	210 (deg)	240 (deg)	270 (deg)	300 (deg)	330 (deg)	Case B1	Case B2
A	T1	180	0.425					T1						425.2	622.3
	T2	180	0.575					T2						439.8	640.6
	T3	180	0.675					T3						449.8	651.2
	T4	180	1.075					T4						490	680.1
	T5	180	1.175					T5						499.7	684.3
	T6	180	1.275					T6						509.4	689.6
B	T7	60	0.975		T7									483.2	673.1
	T8	30	1.025	T8										493.3	681.1
	T9	60	1.075		T9									493.1	677.9
	T10	30	1.125	T10										504.2	686.2
	T11	60	1.175		T11									503	681.5
	T12	30	1.275	T12										519.1	694.7
C	T13	330	0.975										T13	486	677.4
	T14	300	1.025									T14		488.6	676.9
	T15	330	1.075										T15	497.9	683.2
	T16	300	1.125									T16		498.1	680
	T17	330	1.175										T17	508.9	688.1
	T18	300	1.275									T18		512.4	685.6
D	T19	300	0.375									T19		424.7	614.2

	T20	270	0.425								T20			434	628.3
	T21	300	0.475									T21		434.4	627.6
	T22	270	0.525								T22			444.7	642
	T23	300	0.625									T23		449.3	645
	T24	270	0.675								T24			459.8	658.6
E	T25	210	0.375						T25					427.7	619.3
	T26	180	0.425					T26						429.1	621.2
	T27	210	0.475						T27					439.1	635.1
	T28	180	0.525					T28						439	633.3
	T29	210	0.625						T29					455	653.2
	T30	180	0.675					T30						453.9	649.9
F	T31	150	0.625				T31							454.9	653.9
	T32	240	0.625							T32				440.3	631
	T33	330	0.625										T33	442.1	629.5
	T34	150	1.225				T34							514.2	691.9
	T35	240	1.225							T35				488.6	674.3
	T36	330	1.225										T36	487	676.8
G	T37	120	0.27			T37								411.2	597.7
	T38	120	0.32			T28								410.9	597.5
	T39	120	0.87			T39								469.1	667.1
	T40	120	0.92			T40								469.4	660.3
	T41	120	1.32			T41								508.9	673.6
	T42	120	1.475			T42								528.6	695.2